1-1-2015

Interaction Forces And Reaction Kinetics Of Ligand-Cell Receptor Systems Using Atomic Force Microscopy

Anwesha Sarkar
Wayne State University,

Recommended Citation

Sarkar, Anwesha, "Interaction Forces And Reaction Kinetics Of Ligand-Cell Receptor Systems Using Atomic Force Microscopy" (2015). *Wayne State University Dissertations*. 1410.
https://digitalcommons.wayne.edu/oa_dissertations/1410

INTERACTION FORCES AND REACTION KINETICS OF LIGAND-CELL RECEPTOR SYSTEMS USING ATOMIC FORCE MICROSCOPY

by

ANWESHA SARKAR

DISSERTATION

Submitted to the Graduate School

of Wayne State University,

Detroit, Michigan

in partial fulfillment of the requirements

for the degree of

DOCTOR OF PHILOSOPHY

2015

MAJOR: PHYSICS

Approved By:

Advisor Date

DEDICATION

To my husband and my parents who never left me alone

ACKNOWLEDGMENTS

I am extremely grateful to my advisor Dr. Peter M. Hoffmann for his proper guidance and support which helped me to successfully complete my PhD degree. He was always available to me and he listened to my research related problems with patience. He believes in independent work atmosphere of a graduate student and never interferes if not needed. It helped me a lot to grow as a researcher.

My senior graduate students in other experimental condensed matter physics laboratories especially Maheshika Palihawadana Arachchige, Rupam Mukherjee and Suvra Laha were of great help to me. I'm ever grateful to Edward Kramkowski who taught me to operate AFM, use cantilevers and functionalize them. I learned a lot about AFM by observing him and Dr. Hoffmann. I was lucky enough to have Jason Esmacher and Jiayin Dong in our laboratory (as undergraduate students) who helped me a lot in learning functionalization procedures and cell culture protocols. I am very grateful to Dr. Rafael Fridman from the Department of Pathology (Wayne State University) and Dr. Olivia Merkel from Department of Pharmaceutical Sciences (Wayne State University) for helping us and working with us in collaboration. Dr. Fridman and his group members provided us with the biological samples for one of our projects. I am ever grateful to Dr. Anjum Sohail for his immense effort to culture different cancer cells and provide us with proteins and antibodies. I learnt a lot about cell culture and cell maintenance from him. I would like to thank Jiayin Dong, an undergraduate student in our group for helping with cell culture and data analysis. Dr. Merkel's graduate student, Steven Jones who worked with me in collaboration was very helpful to me too.

I would like to thank Dr. Ratna Naik, Dr. Ashish Mukhopadhyay, Dr. Christopher Kelly, and Dr. Rafael Fridman for helping me with their valuable suggestions as my dissertation committee members. Prof. Ratna Naik as the Department Chair of Physics Department was extremely helpful to me throughout my entire graduate study and she encouraged me with helpful discussion and support. I’m thankful to my parents and husband who kept telling me that there is nothing in the world that I can’t achieve.

TABLE OF CONTENTS

CHAPTER 1: INTRODUCTION 1

1.1. Introduction: 1

1.2. Research overview: 2

CHAPTER 2: INSTRUMENTAL SETUP 7

2.1. Importance of Single molecule techniques in Biophysics: 7

2.1.1. Advantages of AFM (Atomic Force Microscopy): 8

2.2. Basic set up of AFM: 10

2.2.1. Bioscope catalyst head: 19

2.2.2. AFM Probes: 21

2.2.3. Bioscope Catalyst Baseplate: 23

2.2.4. Cantilever holders: 25

2.2.5. EasyAlign: 26

2.3. Imaging modes: 27

2.3.1. Contact mode AFM: 27

2.3.2. Tapping mode AFM: 28

2.3.3. Peak force quantitative nanomechanical mapping: 29

2.3.4. MIRO: 38

2.4. TOTAL INTERNAL REFLECTION FLUORESCENCE MICROSCOPY (TIRFM): 39

2.4.1. Fluorescence Microscopy: 39

2.4.2. Advantages of combining AFM and Fluorescence Microscopy: 40

2.4.3. Total Internal Reflection Fluorescence Microscopy: 41

2.4.4. Combining AFM & TIRFM: 44

CHAPTER 3: AFM ON LIVE CELLS 46

3.1. Introduction: 46

3.2. Single-molecule measurements on live cells: 46

3.3. Imaging cells (live and fixed) and cellular segments: 48

3.3.1. Analysis of the dynamic cellular procedures: 50

3.3.2. Discovering cellular compartments: 52

3.4. Measurement of cell adhesion at single cell level: 53

3.5. Deformation of cell membrane by pulling in AFM experiments: 53

CHAPTER 4: BACKGROUND AND THEORY OF FORCE SPECTROSCOPY 56

4.1. Standard theory (Bell-Evans theory): 56

4.1.1. Limitations of this theory: 59

4.2. Bell-Evans-worm-like chain model (BE-WLC model): 60

4.3. Raible’s work to improve standard theory: 63

4.3.1. Heterogeneity of chemical bonds: 63

4.4. Akhremitchev’s work to improve standard theory: 67

4.4.1. Two-bond rupture model: 68

4.5. Conclusions and Summary 71

CHAPTER 5: FORCE MEASUREMENTS USING AVIDIN-BIOTIN MODEL SYSTEM 73

5.1. Materials and methods: 74
5.1.1. Sample preparation: 74
5.1.2. Protocol of decorating the AFM tip and the substrate with PEG linkes: 75
5.2. Force measurement procedure: 76
5.3. Measurement procedure and data analysis: 77
5.4. Measurements on substrates with varying densities of active sites 82
5.4.1. Multiple attachment probability: 84
5.5. Influence of active site density on measurements 95
5.6. Conclusion: 97
CHAPTER 6: DDR1-COLLAGEN INTERACTION FORCES 99
6.1. Introduction: 99
6.2. The extracellular matrix: 99
6.2.1. ECM components: 100
6.2.2. Cell-ECM adhesion: 101
6.2.3. Creation of ECM: 102
6.3. Collagen: 102
6.4. Cell surface receptors: 103
6.4.1. Structure and function: 104
6.4.2. Transmission of signals through cell surface receptors: 105
6.4.3. Role of kinase in signaling: 105
6.5. Integrins: 106

6.5.1. Structure: 107

6.5.2. Activation: 107

6.5.3. Function: 107

6.5.4. Types of integrins: 108

6.6. Discoidin domain receptors (DDRs): 108

6.7. Role of DDR and collagen in cancer and motivation behind our study: 113

6.8. Planned work: 115

6.9. EXPERIMENTAL SAMPLE PREPARATIONS AND ATTACHMENT PROTOCOLS: 116

6.9.1. Cell culture and passaging: 116

6.9.2. Protocol for attaching rat-tail collagen1 to cantilever tip: 118

6.9.3. Protocol for attaching DDR1-Fc fusion protein to cantilever tip: 119

6.9.4. Protocol for attaching rat tail collagen to the glass coverslip substrate: 121

6.10. Force measurements: 122

6.11. Results and Discussion: 123

6.11.1. Measurement of interaction forces between extracted extracellular DDR and Collagen: 137

6.11.2. Force measurements on BPH1 cells ($BPH1_{scr}$, parental $BPH1_{shDDR1}$) with DDR1 and integrin blocking antibody: 140

6.12. Conclusions: 143

CHAPTER 7: CONCLUSION AND FUTURE WORK 145

7.1. Conclusions: 145

7.2. Directions for future work: 148

REFERENCES ……... 152

ABSTRACT ………….. 163

AUTOBIOGRAPHICAL STATEMENT 164

LIST OF FIGURES

Figure 2.1: Components and scopes of single-molecule science 8

Figure 2.2: Schematic diagram of AFM 11

Figure 2.3: Schematic of a typical cantilever deflection vs. piezo height 12

Figure 2.4: Z(X) is the cantilever deflection at the position X, Zc being the cantilever deflection at its end 15

Figure 2.5: Schematic position sensitive detector current signal (I_{PSD}) vs. piezo position (Z_p) curve including approaching and retracting parts. Three types of hysteresis can occur: in the zero force line (A), in the contact part (B) and adhesion (C).. 17

Figure 2.6: Components of AFM[24] 18

Figure 2.7. AFM head[24] (1- Piezoelectric Z scanner, 2-laser stage control knobs, 3- photodetector control knobs, 4- motors for course Z axis positioning).. 19

Figure 2.8. Photodetector structure.. 21

Figure 2.9. Examples of cantilever layout 23

Figure 2.10. Baseplate Components, Controls and Accessories[24] 23

Figure 2.11: Component 3: Sample Substrate Clamps[24].. 24

Figure 2.12. Probe holders[24] 26

Figure 2.13**.** Feedback Loop Electronics 28

Figure 2.14. Feedback Loop Electronics 29

Figure 2.15. Diagrams explaining the principles of peak force tapping and peak force QNM mode[25] 31

Figure 2.16. Calibration in air[26] 36

Figure 2.17. Calibration in liquid[26].. 37

Figure 2.18. Canvas view of MIRO software[27] 39

Figure 2.19.Schematic Diagram of Fluorescence Microscopy 40

Figure 2.20. (a) Light wave is incident normally from glass (n =1.5) to glass-water interface and it is transmitted normally to water (n =1.3), (b) The transmitted light wave is refracted into water at an angle which is greater than its angle of incidence at the interface, (c) The angle of incidence is the critical angle here and it’s approximately 60° for glass-water interface. The angle of refraction is 90° and the transmitted light wave grazes at the glass-water interface, (d) The angle of incidence is greater than the critical angle. So the entire incident light is reflected back to the glass media. This event is mentioned as total internal reflection. 43

Figure 2.21.: Schematic diagrams of the three basic TIRF microscope configurations (not to scale). (a) In the prism-based geometry, a beam of light is directed through a prism (with high index of refraction such as glass or sapphire), which has been optically coupled to a glass cover slip with a thin layer of index-matching oil. (b) The objective-based TIRF microscope requires the use of objectives with an NA .1.3.. 44

Figure 3.1.AFM-based nanoscale microscopy technique of live cells. (a) AFM characterizes a sample by detecting the small interaction forces between the cell surface and the cantilever tip. (b) The AFM tip is scanned through the surface of the cell (arrows) in order to receive the surface topography (indicated by dashed line). (c) The cantilever tip is applied for the measurement of cell-surface interactions. Examples display a functionalized tip: left most tip is tagged with a ligand to measure interaction forces with its cognate receptor, middle tip is functionalized with chemical components in order to figure out chemical interactions and right most tip is decorated with cell-adhesion molecules in order to figure out interactions between hemophilic or heterophilic components and other cell-adhesion molecules... 49

Figure 3.2.(a) represents the field of view where we can see the AFM cantilever tip (DNP-C cantilever from Bruker corporation) scanning on top of BXPC-3 cells, (b) represents height image of that particular cell, tip is scanning on; (c) represents deflection error image of that particular cell. Average size of those cells are 25-30μm. Both (b) and (c) are 50×50 μm^2 images............. 52

Figure 4.1. Theoritical simulation of probability distribution function (pdf) according to standard theory. 58

Figure 4.2. shows linear relationship between f_p (the most probable rupture force) and the logarithm of the load rate, r_f according to standard theory. 59

Figure 4.3. Theoretical simulation of rupture force (pN) vs retract speed (nm/s) according to standard theory and worm-like chain model.. 63

Figure 5.1. Experimental force curves: Blue is approach and red is retract. (a) Cantilever is in contact with surface, bond forms, (b) Bond experiences maximum stretch, (c) Bond breaks. 78

Figure 5.2. Different arrangements of molecular interactions 79

Figure 5.3. –vln(S(f)) (in log $_{10}$ scale) vs rupture force (pN) plot for different pulling velocities (ranging from 10 nm/s to 10000 nm/s) 81

Figure 5.4: Binding probability vs Biotin ratio plot 83

Figure 5.5: Multiattachment probability vs biotin ratio (%) 84

Figure 5.6: Contour length histogram for 50 % Biotin data 85

Figure 5.7: Pdf of rupture force for 50% biotin data where peak of the Gaussian fit signifies the probable rupture force (107.7pN in this case). 86

Figure 5.8: Pdf of ΔR for 50% biotin data 89

Figure 5.9. Zero-distance multiple attachment probability and tail percentage vs biotin ratio (%): open circles indicate zero distance multiple attachment probability and closed circles represent tail percentage 91

Figure 5.10: Simulated rupture force histograms with different scenarios 95

Figure 6.1. (a) AFM image of rat tail collagen type I attached to glass coverslip (scan size 17 μm), (b) represents polypeptide chains of collagen fibril. 103

Figure 6.2.Basic structure of DDR1a and DDR2 109

Figure 6.3.Role of DDRs and other receptors in downstream signaling pathways 112

Figure 6.4: (a) Fluorescent image of collagen attached to the cantilever tip (5.3×5.3 inch) and (b) Zoomed-in image of collagen fibril fragment 122

Figure 6.5: (a) Microscope images of the BPH1$_{\mathrm{shDDR1}}$ cells at 10X magnification (b) Same cells with magnification 20X; (c) Microscope images of the BPH1$_{\mathrm{scr}}$ at 10X magnification (d) Same cells at magnification 20X. 124

Figure 6.6: (a) BPH1$_{\mathrm{shDDR1}}$ cell with AFM cantilever; (b) AFM height profile and (c) AFM peak force error image of a particular cell 125

Figure 6.7: It shows the field of view where unfunctionalized DNP-C cantilever is scanning on top of a BPH1$_{\mathrm{scr}}$ cell 126

Figure 6.8: (a) represents the height image of BXPC-3 cell scanned with DNP-C cantilever and (b) represents the peak force error image of BXPC-3 cell. 127

Figure 6.9: represents example of control force curves performed on the $BPH1_{scr}$ cells where the blue line represents the approach curve and red line represents the retract curve 127

Figure 6.10: image of $BPH1_{scr}$ cell scanned with collagen functionalized cantilever 128

Figure 6.11 (a) and (b) Height image and peak force error image of $BPH1_{scr}$ cell scanned with collagen functionalized OBL-A cantilever with scan size of 40 µm. (c) and (d) Height image and peak force error image of $BPH1_{scr}$ cell scanned with collagen functionalized OBL-A cantilever with scan size of 20 µm. 129

Figure 6.12: (a) Example of a single rupture event due to presence of collagen 1 on the cantilever tip and $BPH1_{scr}$ cell as substrates; (b) Double rupture event due to the binding of collagen to more than one cell surface receptor (the blue line represents the approach curve and red line represents the retract curve) 130

Figure 6.13: (a), (b) and (c) represent collagen functionalized OBL-A cantilever, the right most cantilever in all the images (with nominal stiffness: 0.03 N/m) scanning on top of $BPH1_{scr}$ cells of different shapes 131

Figure 6.14: (a) represents rupture force histogram performed on the elongated $BPH1_{scr}$ cell (shown in the figure 6.13 (a)) before injecting fibronectin and (b) represents rupture force histogram performed on the elongated $BPH1_{scr}$ cell (shown in the figure 6.13 (a)) after injecting fibronectin 132

Figure 6.15: (a) represents rupture force histogram performed on the elongated $BPH1_{shDDR1}$cell (shown in the figure 6.13. (a)) before injecting fibronectin and (b) represents rupture force histogram performed on the elongated $BPH1_{shDDR1}$ cell (shown in the figure 6.13. (a)) after injecting fibronectin 133

Figure 6.16: (a) and (b) Rupture force histogram for single rupture events, performed on MiaPaCa-2 EV Cells before and after injecting integrin blocking antibody (AII B2 –anti beta integrin 1 blocking antibody with concentration 262 µg/ml) respectively 134

Figure 6.17: (a) represents rupture force histograms for single rupture events, performed on MiaPaCa-2 DDR1b Cells without integrin blocking antibody or fibronectin, (b) represents rupture force histograms for single rupture events, performed on MiaPaCa-2 DDR1b Cells with integrin blocking antibody, (c) represents rupture force histogram for single rupture events, performed on MiaPaCa-2 DDR1b Cells with fibronectin 135

Figure 6.18: Rupture force histogram for single rupture events, performed on MiaPaCa-2 DDR1b R105A cells.......... 136

Figure 6.19: (a) and (b) AFM image of Rat tail Collagen 1 attached to glass coverslip with scan size of 50 μm. ; (c) and (d) AFM image of Rat tail Collagen 1 attached to glass coverslip with scan size of 17 μm. : (e) and (f) AFM image of Rat tail Collagen 1 attached to glass coverslip with scan size of 5.3 μm. Scan rates for imaging all of them was 0.5 Hz. (a), (c) and (e) represent the height images and (b), (d) and (f) represent the peak force error images.......... 138

Figure 6.20: Example of force curve due to interaction of extracted extracellular DDR on the cantilever tip and Collagen on the glass coverslip where measured rupture force between the the two dotted red bars is 150 pN. 139

Figure 6.21: (a) Rupture force histogram on $BPH1_{scr}$ cells data with DDR1 blocking antibody with most probable rupture force as 150 pN, (b) Rupture force histogram on $BPH1_{scr}$ cells data with integrin blocking antibody with most probable rupture force as 150 pN; (c) Rupture force histogram on $BPH1_{shDDR1}$ cells data with DDR1 blocking antibody with most probable rupture force as 130 pN and (d) Rupture force histogram on $BPH1_{shDDR1}$ cells data with integrin blocking antibody with most probable rupture force as 138 pN.......... 141

LIST OF TABLES

Table 2.1 Description and function of different components of AFM[24]...................................... 18

Table 6.1: It summarizes all different types of cells with modulated expressions of DDR1, used in our experiments……………………………………………………….......................................117

Table 6.2 It summarizes binding probability measurements for different types of live cells using different experimental conditions 141

Table 6.3 It summarizes the most probable rupture force measurements for different types of live cells using different experimental conditions 142

CHAPTER 1: INTRODUCTION

1.1. Introduction:

Biophysics has emerged as an important field that uses the principles of physics to explain activities of biological molecules, their functions and molecular structures. Development of new experimental techniques and theories have played an important role in the rapid growth of this field. As protein-protein interactions (receptor-ligand interactions, interactions between antigen and antibodies) play crucial role in most of the biological processes in various organisms, they have been one of the central themes of these studies. Both structural, kinetic and thermodynamic approaches have been used to investigate these protein-protein interactions and measure binding probabilities, binding energies and dissociation constants[1].

Single molecule measurement is a kinetic technique through which we can investigate interactions between biomolecules not only in isolated molecules, but also on live cells. Single molecule measurement techniques like optical tweezer, magnetic tweezer and atomic force microscopy (AFM) have emerged as trusted methods to provide precise information on binding and dissociation kinetics. AFM has several advantages (described in detail in chapter 2) over the other mentioned approaches including high resolution imaging. It is capable to perform measurement of forces in the range of piconewtons.

AFM can not only image biological samples with high resolution in air as well as in liquid, but can also be used to obtain forces between single molecules. Florin and coworkers[2] first investigated avidin-biotin bonds and showed that the minimum force needed to break an avidin-biotin bond is almost 160pN. Many other protein-ligand systems have since been investigated after this pioneering experiment. An important advance was the introduction of flexible polymeric linkers (Hinterdorfer et al[3]) to attach the ligands to the AFM cantilever tip. This additional step helps to spatially separate and distinguish specific and nonspecific cantilever-surface adhesion. By functionalizing cantilever with low ligand density, multiple attachments can be controlled and true single molecule measurements are becoming an efficient method to localize binding sites.

1.2. Research overview:

Our research involves two simultaneous projects using atomic force microscopy. The first project is about effect of surface density of active sites on rupture force distributions of single molecule interactions. In AFM measurements we initially bring a functionalized cantilever (with a ligand) near the functionalized surface or live cell (with complementary receptor). In this process, the molecules on the cantilever and the substrate have an opportunity to bind together and form an assembly. The minimum force required for breaking the bond (once the cantilever is retracted) is defined as the rupture force or unbinding force. The main observable in such a measurement is the unbinding or 'rupture' force. Once a histogram of these rupture forces is plotted and fitted with Gaussian, the most probable rupture force can be derived from the peak of the distribution. AFM force measurements demonstrate increase of the most probable unbinding rupture force with increasing loading rate. Evans[4, 5] introduced a "standard" theory (based on thermal activation model) in order to determine kinetic parameters, bond distances and activation barriers.

One of the assumptions of the standard theory is constant loading rate. This loading rate is defined as the product of the cantilever spring constant and the fixed vertical scan speed[6]. This assumption leads to the fact that the most probable rupture force varies linearly with logarithm of the retract speed. In actuality, the rupture force depends on the non- linear elasticity of polymeric linkers and molecules. Therefore, because the retract speed is applied by the piezo-electric actuator attached to the cantilever base, the applied force is not proportional to piezo extension. This is one of the reasons the standard theory has some major limitations (discussed in chapter 4 in detail).

The contributions from multiple attachments[7, 8], heterogeneity in the bond conformations[9] and non-linear force profile should be taken into account while analyzing the force data. Because of these complications, an explicit interpretation of the acquired rupture force data is not always easy. The Bell-Evans standard theory, used for analyzing rupture force data yields a rupture force probability distribution function which is skewed to the left (towards low force). However, most of the experimental measurements of rupture force data generate a probability distribution function (pdf) with a high force tail. The probable cause of this high force tail in the rupture force pdf is either multiple attachments (though recognizable multiple ruptures are typically removed from rupture force analysis) or heterogeneous bonding. The objectives of our first project was to execute single molecular force measurements using avidin-biotin model system, improve the theory used to analyze rupture force data, apply the extended theory to interpret the force data in similar biologically relevant model systems and retrieve important parameters.

To study the effect of multiple attachments, we created a varying density of active sites using a self-assembled monolayer by incubating the substrate in mixed solutions of active (biotin) and inactive (methyl-terminated) PEG molecules and pursued imaging and force measurements with avidin functionalized AFM tip. We presented a combined approach to answer the question of how much of the high force tail can be attributed to multiple attachments or to bond heterogeneity. We also performed Monte Carlo simulations in order to match experimental results with theoretical expectations.

The second project is about applying our experience in the single molecule force measurements to examine and interpret the interaction between discoidin domain receptors

(DDR1)[1, 10-12] and their ligand collagen in live cells (cancer cells) as well as outside the cell. We passaged and maintained the cells ourselves and followed all necessary procedures to make sure that the cells are alive and healthy during the few hours the experiment. Several control experiments were performed on BPH1 cells, BXPC-3 cells and MiaPaCa cells ($BPH1_{scr}$, parental $BPH1_{shDDR1}$, MiaPaCa-2 EV, MiaPaCa-2 DDR1b, MiaPaCa-2 DDR1b R105A) with non-functionalized cantilevers. The subscripts ‘scr’ and ‘shDDR1’ in the last line stand for scramble and shRNA DDR1 respectively. Detailed description of these cells can be found in chapter 6.

By regulating interaction of tumor cells with their surrounding collagen matrix, DDR1 function as a vital receptor in cancer. The alterations in DDR1 genes in human cancer cells imply that advancement of disease can be influenced by DDR1. However, research studies have provided limited information about DDR1 behavior at the cell-collagen interface. That is why we are making an experimental effort to combine biological information and force based microscopy techniques to shed new light on how DDR1 functions in physiological and pathological conditions.

In this project, we first performed control experiments with a non-functionalized cantilever on BPH1 cells and BXPC-3 cells (control and expressing DDR1). Both BPH1 (benign prostatic hyperplasia) cells and BXPC-3 (pancreatic cancer) cells are of similar sizes (20-30 μm). Next, we performed AFM imaging and force measurements using BPH1 cells with collagen type I functionalized OBL-A cantilever. To ensure that collagen is properly attached to the cantilever when functionalizing cantilever with rat tail collagen type I, we imaged the cantilever tip with fluorescence microscopy with clean glass coverslip as substrate to observe the presence of collagen auto-fluorescence.

Major receptors which bind to collagen and are present on these cell surfaces are integrins and DDRs. As we are only interested in DDR1-collagen interaction, we looked for ways to block integrin binding to collagen. We found that by injecting fibronectin (ECM glycoprotein which binds to integrin receptors but does not bind to DDR1 and DDR2) in the liquid cell we could block forces generated by interactions of collagen and integrin. We also injected integrin blocking antibody (AII B2 –anti beta integrin 1 blocking antibody with concentration 262 μg/ml) with BPH1 cells and performed force measurements and binding probability measurements. The integrin blocking antibody (AII B2 –anti beta integrin 1 blocking antibody with concentration 262 μg/ml) showed very similar suppression of the binding probability as fibronectin, suggesting that both methods are effective in blocking integrin-collagen bonding. To ensure specificity of the remaining binding events we observed, we also functionalized cantilevers with denatured (by heating collagen at 60 °C for 30 minutes) rat tail type I collagen to perform additional control experiments. These showed no binding, suggesting that what we observed were specific binding events between DDR1 and collagen. In a further control experiment, we injected a possible DDR1 blocking antibody (human IgM-DDR1 hu 5E11 with a concentration of 2.07 mg/ml, potential therapeutic drug), which should just leave integrin binding. The measured binding probability seemed to confirm that the antibody was successful in blocking DDR1, as the binding probability measured after blocking integrin and after blocking DDR1 added up to the binding probability measured in the absence of both blocking antibodies.

In order to confirm these results, we also performed measurements on another cell line, MiaPaCa-2 cells, which included three types: MiaPaCa-2 EV, MiaPaCa-2 DDR1b and MiaPaCa-2 DDR1b R105A. After using the various methods to block integrins, we observed a small amount of binding in the wild-type case, a large amount in the overexpressed case, and no binding on the mutated cells, further confirming specificity of our force measurements.

We briefly reviewed the progress in the field of single molecule force measurements and our research projects in this chapter. The second chapter to dedicated to explain basic working principle of AFM, TIRF, the details of the AFM set up and modes that we use frequently. The third chapter summarizes the research that have been done so far on live cells using AFM and we will also discuss about the cell membrane deformation by pulling experiments. The fourth chapter presents the background and theories that have been used over the years for analysis and interpretation of the experimental rupture force data. Chapter five explains the functionalization protocols and our contribution to improve the theory for the measurement of interaction forces of the avidin-biotin model system. In chapter six, we will explain the results from DDR1-collagen interaction force and binding probability measurements on three different types of live cells (BPH1scr, parental BPH1shDDR1, MiaPaCa-2 EV, MiaPaCa-2 DDR1b, MiaPaCa-2 DDR1b R105A). In seventh chapter, we will explain all our conclusions from our projects and provide directions for future work.

CHAPTER 2: INSTRUMENTAL SETUP

2.1. Importance of Single molecule techniques in Biophysics:

Single molecule techniques[13] with their ability to reveal ‘hidden information’ about molecules (see Fig 2.1), have become very important over the last few years. These techniques examine the properties of individual molecule at a time. By contrast, most techniques survey the properties of large numbers of molecules, and only the average behavior of the molecules can be accessed. Single molecule techniques provide not only average information (if repeated measurements are performed), but also information about each single molecule. The range of variation and statistical variability of molecules cannot be determined from ensemble methods, where many molecules are measured simultaneously, but only from methods where data at the single molecule level is available. Single molecule techniques are also superior in situations in which only a few molecules are available, or where molecules are associated with a specific microenvironment and cannot be extracted from the environment without distorting the results. This is often the case if interactions of molecules in living cells are to be studied.

Measurements of single molecular properties are helpful in discovering unusual states or molecular heterogeneity. For example, some of these techniques can measure molecular forces and kinetic rate constants among different states of molecules. Single molecule techniques such as optical tweezers, magnetic tweezers[14] and atomic force microscopy (AFM) have played an important role in the development of fields such as protein folding, molecular motors and protein-protein interaction force measurements. Single molecule techniques are developing very fast and are bridging the gap between physics and biology.

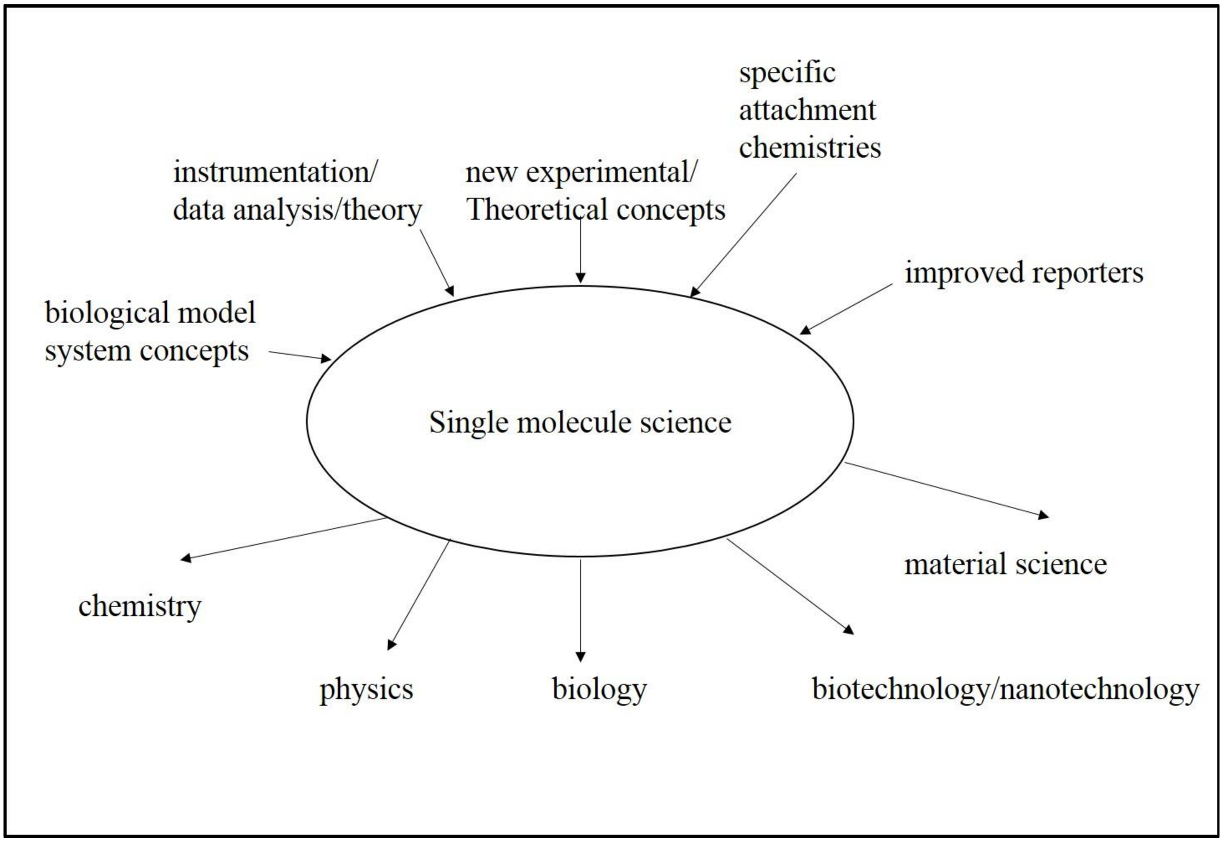

Figure 2.1: Components and scopes of single-molecule science

2.1.1. Advantages of AFM (Atomic Force Microscopy):

Atomic force Microscopy is one of the most popular and frequently used single molecule techniques. Examples of other single molecule techniques include optical tweezers, magnetic tweezers and fluorescence resonance energy transfer (FRET) [15, 16].

The atomic force microscope (which is a type of scanning probe microscope (SPM)), with its ability to image conducting as well as non-conducting samples, can investigate a wide range of samples including biomolecules (e.g., DNA, RNA, proteins and phospholipids) and living cells, cell membranes and tissues. AFM can survey mechanical, structural and functional properties of the sample with sub-nanometer resolution under a variety of conditions, including physiological conditions for the measurement of live biological samples. This helps to eliminate complex sample preparation procedure, protects the sample from getting damaged and allows measurements mimicking the natural state of cells[17] as much as possible.

AFM also can operate in different imaging modes including contact mode, tapping mode and non-contact mode. In contact mode, the AFM probe is brought into close contact with the sample and always remains in soft contact with the sample surface. The AFM electronics has a feedback loop, which uses the difference between the cantilever deflection, as measured by an optical sensor, and the desired deflection setpoint as feedback information to determine the vertical separation between sample and cantilever. The purpose of this adjustment of motion is to maintain a fixed force (determined by the cantilever deflection) between the cantilever tip and the sample. In constant force mode, the voltage acting on the scanner to control the cantilever-surface separation provides the topography image. Thus, the topography image is an image of constant force contours. The contact mode can be useful to image biological samples in liquid[18], but it can lead to sample damage because the tip is dragged laterally across the surface.

In the tapping mode, the tip oscillates at a fixed frequency close or identical to the cantilever’s resonance frequency, intermittently touching the surface of the substrate. The feedback loop mechanism collects the information about the oscillation amplitude or phase, and controls one of them (typically the amplitude) in order to keep it constant. For example, when the tip goes over a bumpy surface, the amplitude reduces and the feedback loop increases the tip-sample distance to maintain a constant amplitude. In tapping mode, the transverse motion of the tip along the surface is less affected by frictional forces, reducing the possibilities of damaging the sample.

AFM can also be used to manipulate small particles or molecules, and to apply and measure mechanical force. For example, the surface of a substrate can be functionalized with molecules and the tip coated with other molecules which can form bonds with the surface molecules. The bonds can be formed by moving the tip very close to the substrate. If the tip is retracted at constant speed, the deflection of the tip gives the amount of force needed to break the bond. This force is called rupture force or unbinding force.

AFM can measure forces from about 20 pico-newton to 10 nano-newton depending on the stiffness of the cantilever being used. Typical stiffnesses used in biophysical experiments vary from 10 to 1000 pico-newton per nanometer.

2.2. Basic set up of AFM:

The basic instrumentation of AFM comprises of a probe (a cantilever with sharp tip at the end), a cantilever deflection detecting system, a piezoelectric scanner, a sample holder and electronics. Sample characterization is done by measuring the force of interaction between the cantilever tip and the sample surface. In case of force measurement, the two interacting solid surfaces are the cantilever tip and the sample or substrate. The sample in consideration is initially placed on the top of piezoelectric scanner and can be moved upon the application of a voltage to the scanner. AFM cantilever deflection can be denoted as $Z_{cantilever}$ and position of the piezoelectric scanner as Z_{piezo}.

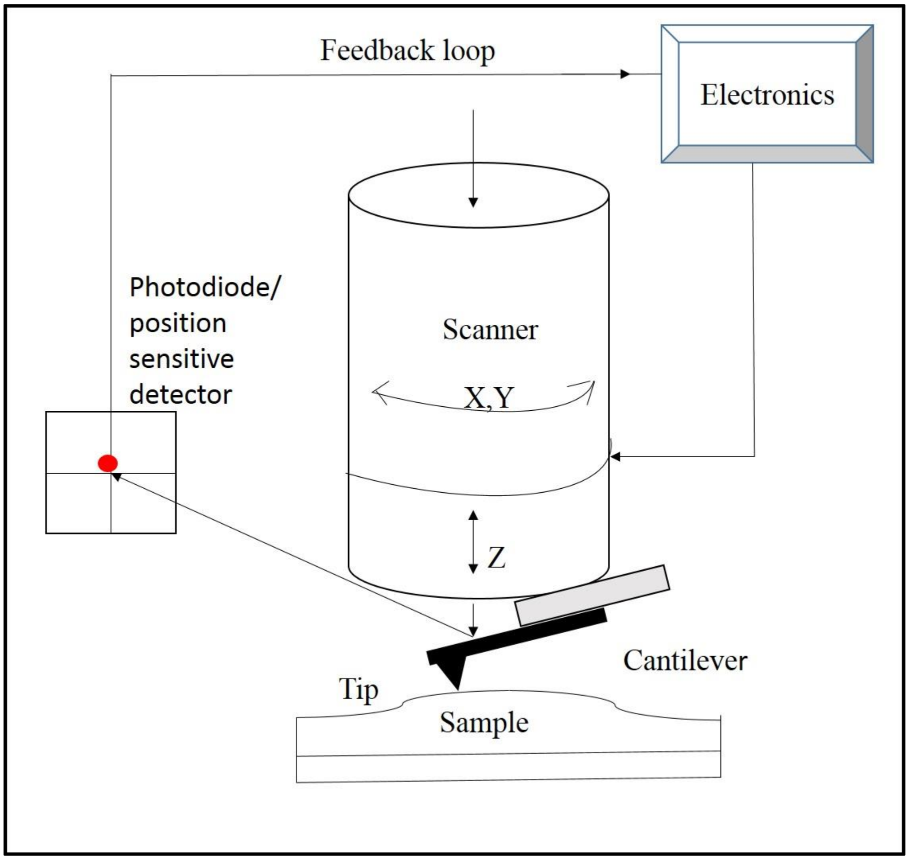

Figure 2.2: Schematic diagram of AFM

The tip sample separating distance is then given by

$$d = (Z_{cantilever} + Z_{piezo}) \tag{2.1}$$

The force on the cantilever can be derived by using Hooke's law:

$$F = -k\, Z_{cantilever} \tag{2.2}$$

where *k* is cantilever's spring constant.

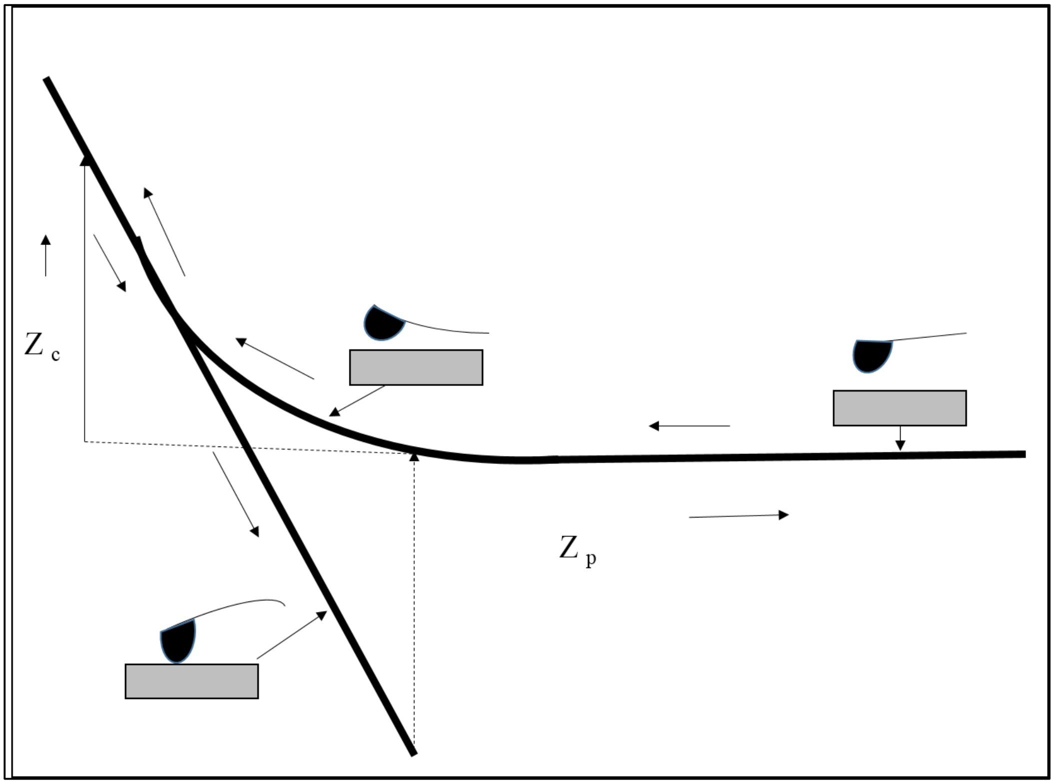

Figure 2.3: Schematic of a typical cantilever deflection vs. piezo height

Initially the probe is manually moved close to the surface of the substrate. This step is followed by a fine motion of the tip by the piezoelectric scanner, changing the sample distance. The cantilever is moved towards the surface until a desired force set-point is reached. The force is measured via the deflection of the cantilever. The deflection is measured via a laser beam that is focused and aligned to the back side of the cantilever (usually coated with gold in order to increase reflectivity) from where it reflects off to a position-sensitive detector (PSD), which is usually a sectioned photodiode. When the probe comes in very close proximity with the sample, the cantilever is deflected due to the force of interaction between sample surface and the tip surface (Figure 2.3). Then the laser spot on the detector (photodiode) shifts from its previous position. As a consequence, a voltage difference is introduced between the four sections of the PSD.

As shown in Figure 2.4, Z(X) represents the cantilever deflection where X represents the position and $Z_{cantilever}$ or Z_c is cantilever deflection at the end. So, $\frac{dZ_{cantilever}}{dX}$ is the end-slope. When the cantilever bends upon application of force to the cantilever tip, the bounced-off light-beam grazes through an angle equal to 2 $\frac{dZ_{cantilever}}{dX}$.

$$Variation\ in\ end - slope = \frac{dZ_{cantilever}}{dX} = \frac{6FL^2}{Ewt^3} \tag{2.3}$$

Where, E = Young's modulus, F = force acting on the tip, t= thickness of the cantilever, w= width of the cantilever, L =length of the cantilever. Hence, the cantilever deflection can be expressed in terms of the end-slope because the force acting on the tip is proportional to the variation in end-slope[19].

$$Z_{cantilever} = \frac{4FL^3}{Ewt^3} = \frac{2}{3}L\left(\frac{dZ_{cantilever}}{dX}\right) \tag{2.4}$$

The cantilever is usually made of silicon or silicon nitride. Various types of cantilevers can be used depending on different AFM imaging modes. The spring constant of the cantilever should be very low when the AFM is operated in the static contact mode whereas a higher value of spring constant is preferable when the AFM is operated in the dynamic operational modes, such as tapping mode. The spring constant of the cantilever is given by

$$k = \frac{F}{Z_{cantilever}} = \frac{Ewt^3}{4L^3} \tag{2.5}$$

The resonance frequency of the cantilever is represented as

$$\nu = \frac{1}{2\pi}\sqrt{\frac{k}{m^*}} \tag{2.6}$$

where m^* is the effective mass of the cantilever and it can represented as

$$m^* = nm_b = n\rho Lwt \tag{2.7}$$

For a rectangular cantilever[19, 20], m_b represents mass of the cantilever beam and n is a factor that varies depending on the shape and spring constant of the cantilever. In theory, cantilever is considered as an ideal spring with one mode of vibration but in case of experiments, cantilevers have definite shape (which should be taken into account) and different modes of vibration. Eppell et al.[21-23] took the definite shape factor into account and generated formulas for angular frequencies of the cantilever through numerical analysis. The value of angular frequency in a particular vibration mode is given by

$$\nu_i = \frac{1}{2\pi}\sqrt{\alpha_i^4}\,\frac{t}{L^2}\sqrt{\frac{E}{12\rho}} \tag{2.8}$$

As a consequence of presence of several modes of vibration, the mean squared deflection of the cantilever in one particular mode can be represented as

$$< Z_i^2(L) >= \frac{12k_BT}{k\alpha_i^4} \tag{2.9}$$

For rectangular cantilever, vibration parameter α_1 (as α_1 =1.875) is much lower in values compared to α_2 and α_3. So, we are write the last equation as

$$< Z_1^2(L) >= \frac{12k_BT}{k\alpha_1^4} \tag{2.10}$$

That leads the final formula for resonant frequency of the cantilever as

$$\nu_1 = \frac{1}{2\pi}\sqrt{\frac{(1.875)^4}{12}}\,\frac{t}{L^2}\sqrt{\frac{E}{\rho}} \tag{2.11}$$

$$\nu_1 = 0.1615\,\frac{t}{L^2}\sqrt{\frac{E}{\rho}} \tag{2.12}$$

where ρ is the density of cantilever material.

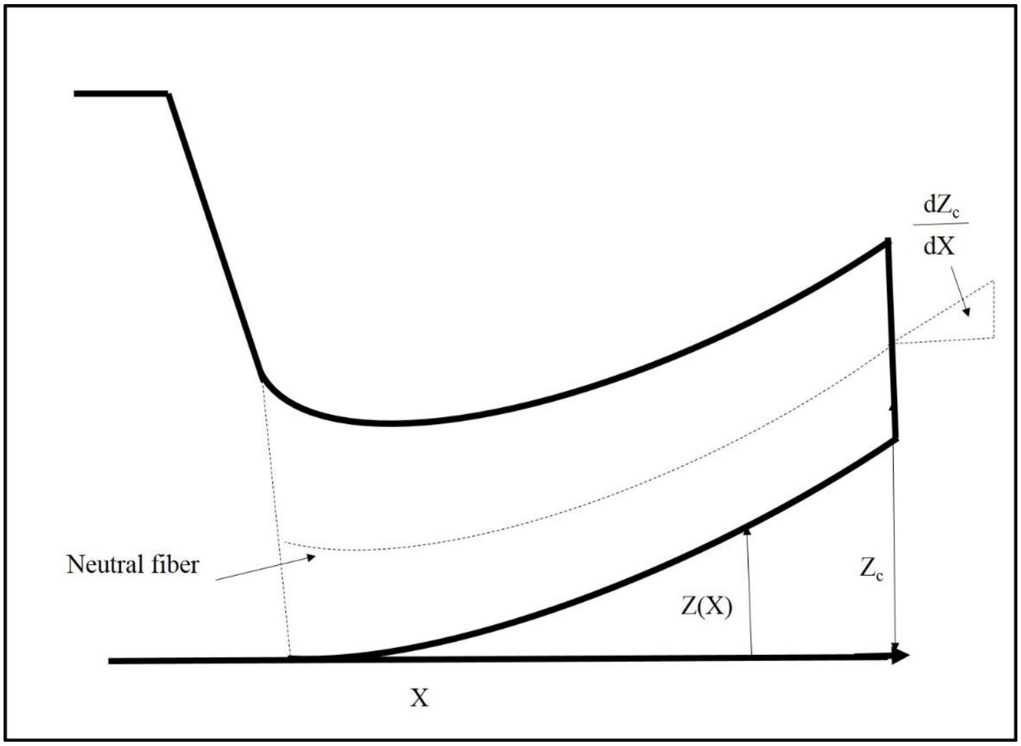

Figure 2.4: Z(X) is the cantilever deflection at the position X, Zc being the cantilever deflection at its end

In order to obtain a force-versus-distance curve, the photodiode current I_{PSD} (often expressed as a voltage) and piezoelectric translation or extension Z_p have to be expressed in terms of force and distance. In case of AFM, the sensitivity and zero distance (contact point) are derived from the force curves. In most cases, the onset of the linear portion of the contact region is referred to as zero distance and, when measuring on an "infinitely stiff" substrate like diamond, the slope of the linear region provides the sensitivity of the photodiode.

$$Z_c = \frac{I_{PSD}}{\left(\frac{dI_{PSD}}{dZ_p}\right)} \tag{2.13}$$

The force F can then be obtained by multiplying k with Z_c.

If the substrate is an infinitely hard material and a long-range surface force is acting on the tip, then the sensitivity can be retrieved from the linear contact region. Zero distance can be obtained from extrapolating from the non-contact regime at large distance and determining the where the extrapolated zero-force line meets the linear contact line. In the non-contact region of the force curve, tip sample separating distance is given by

$$d = \left(Z_p + Z_c\right) = \left(Z_p - \frac{F}{k}\right) \tag{2.14}$$

whereas in the contact part $Z_p = -Z_c$ and d=0

Similarly d can be calculated in case of a deformable substrate with or without surface forces. If the cantilever is in contact with a deformable substrate, then $d = \left(Z_p + Z_c\right)$ will be negative and represent the indentation depth of the tip.

Approach and retract parts of force curves are different in many cases. Usually there exists a difference in the zero-force line due to several reasons like drag in liquid environment. This can be reduced by adjusting approaching or retracting speed. Differences can also be due to plastic deformation of the sample, or to nonlinearities and hysteresis in the piezo-electric actuators.

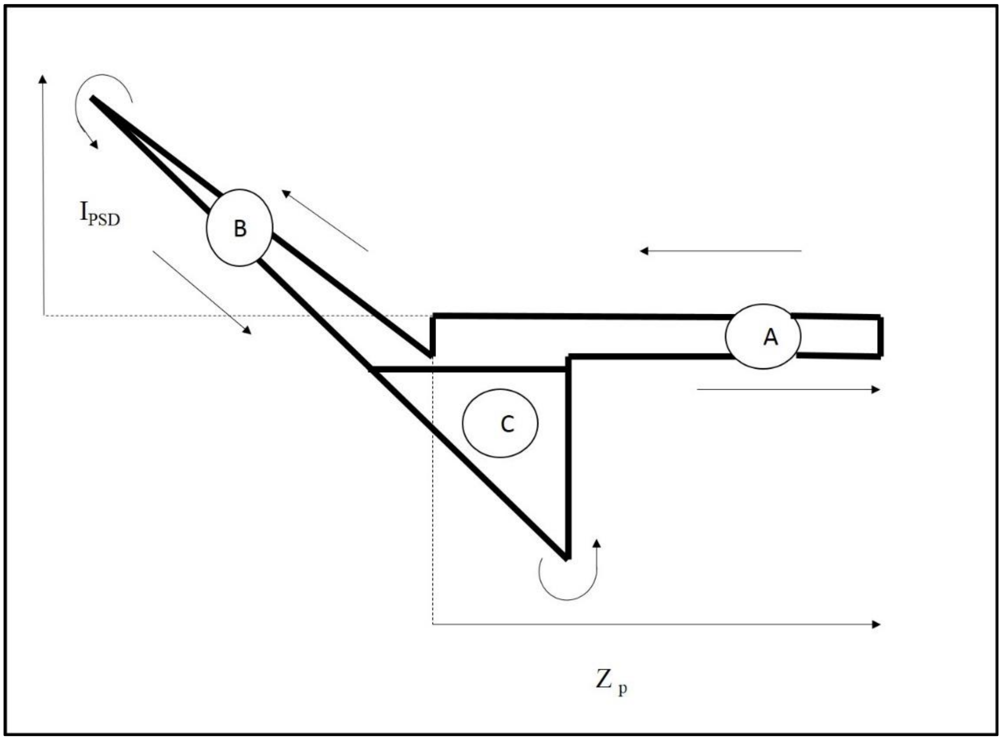

Figure 2.5: Schematic position sensitive detector current signal (I_{PSD}) vs. piezo position (Z_p) curve including approaching and retracting parts. Three types of hysteresis can occur: in the zero force line (A), in the contact part (B) and adhesion (C)

Designs of AFM instruments can vary to improve the quality of a specific study. We currently use a commercial AFM purchased from Bruker Corporation. Our AFM is equipped with an inverted optical microscope, probe holders, sample holding clamps, easy align and base plate[22]. In order to lower the bias in AFM data caused by the external noise and a vibration, the entire set up is stationed located inside an isolation hood and placed on a floating vibration isolation table. Following is the picture and detailed description of the major components of our Bruker AFM set up.

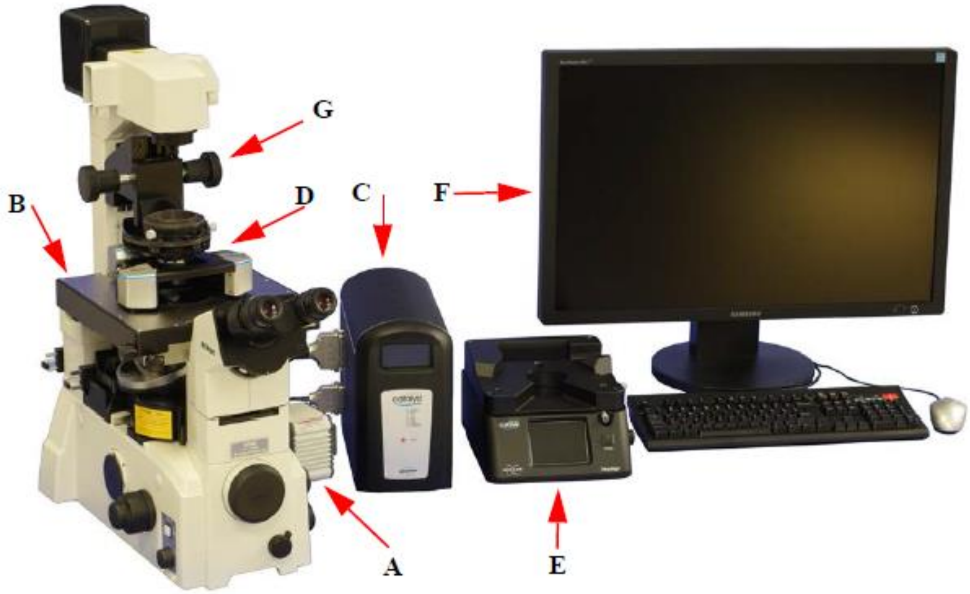

Figure 2.6: Components of AFM[24]

Table 2.1 Description and function of different components of AFM[24]

Code	Description	Function
A	Inverted Optical Microscope	Inverted microscope base
B	Baseplate	Provides XY piezo scanning and motorized XY stage for sample
C	Electronics Box	BioScope Catalyst Electronics Interface Box - Provides interface between SPM and NanoScope V controller and displays meter signals and system status information
D	Head	Provides Z piezo scanning, cantilever deflection detection optics and electronics and motors for coarse Z positioning and motorized SPM
E	EasyAlign	Provides an optical view of the SPM probe and laser for the easiest possible alignment of laser optics.
F	Monitor	Viewing NanoScope software application and images
G	Condenser	Provides illumination for light microscope

2.2.1. Bioscope catalyst head:

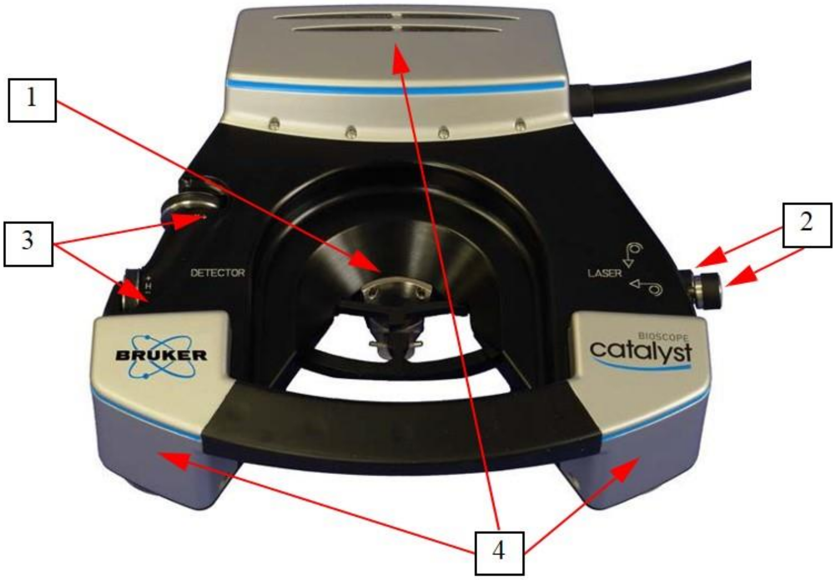

Figure 2.7. AFM head[24] (1- Piezoelectric Z scanner, 2-laser stage control knobs, 3- photodetector control knobs, 4- motors for course Z axis positioning)

In order to achieve stability, the BioScope Catalyst head sits on the baseplate on a three point mount. The head is composed of the following units:

1. Piezoelectric Z Scanner positions the cantilever holder along the Z-axis. The full vertical scan range of 16 μm is generated by -20 to +150 V_{dc}, fed to the piezo-element by the controller. Z-axis position data is measured independently by a sensor that doesn't depend on of the Z-scanner drive voltage. This eliminated hysteresis and ensures positioning fidelity. Such a scheme is called "closed-loop" operation.
2. The deflection measuring laser beam from the laser diode is aligned by two adjustment knobs to reach the back of the cantilever from where the laser reflects

off to yield a spot on a quad photodetector. These control knobs adjust horizontal and vertical positioning of the beam.

3. The quad photodetector (Figure 2.8) position is adjusted by the knobs shown. Output signals from the four sections of the photodetector are summed to produce a SUM signal. The SUM signal provides an overall measure of the total light reflected off the cantilever. It should be maximized to obtain optimal measurement conditions. When the cantilever bends vertically (while imaging) the laser spot moves, changing the distribution of light hitting the different sections of the photo diode. The vertical motion is measured by measuring the difference of photocurrent induced on the upper versus the lower sections of the photodiode, i.e. by $\Delta I_{vertical} = (I_A+I_B)-(I_C+I_D)$. This signal is used in contact and tapping AFM mode. The amplified differential signal between the sections A, B and C, D yields a measurement for the vertical deflection of the cantilever. While operating in the tapping mode, the differential signal is fed to a digital lock-in amplifier. The intensified differential signal between sections (A+C) and the (B+D) provides the measurement for the cantilever torsion, which can be used to measure lateral forces on the cantilever, for example during friction.

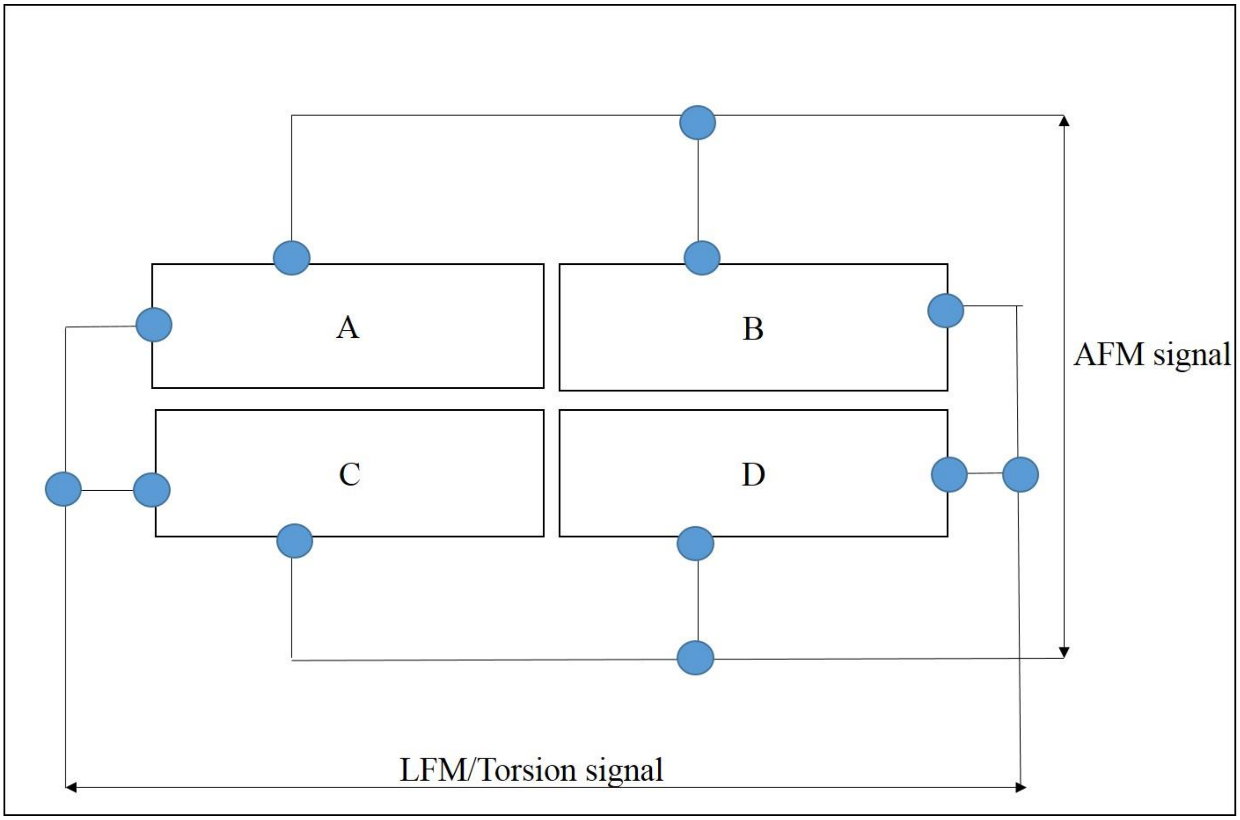

Figure 2.8. Photodetector structure

4. Three motors in the Bioscope catalyst head perform coarse positioning of the Z-axis over a range of approximately 8.4 mm or 0.33 in. The NanoScope V controller regulates these motors depending on input signal set by the user, movement of a joystick or automatically as part of a computerized approach routine. The computerized approach combines coarse (motors) and fine (piezo) motion to ensure that the cantilever tip touches the surface as gently as possible to avoid damage to the tip or sample.

2.2.2. AFM Probes:

The cantilever tip is made of the same material as the cantilever body. In general, it has pyramidal shape (with radius of curvature of less than 50 nm at the tip end). The resolution of obtained images or force curves are directly affected by the particular tip characteristics. The cantilever is usually selected depending upon the nature of the sample. Cantilevers with higher spring constants can be used to achieve topographical images of hard surfaces. Soft materials should be preferably investigated with cantilevers with lower spring constants. Single molecule force measurements are better done by low stiffness cantilevers with spring constant of order <0.1 N/m. The majority of our imaging applications involve biomolecules and are carried out in fluid (phosphate buffer saline and water). In order to reduce sample damage, imaging forces are chosen very low under these conditions. Unsharpened cantilevers of low stiffness are recommended for cell imaging applications as sharp probes tend to damage the cell membrane very easily.

Three examples of cantilevers used frequently in our experiments are as follows:

a) ScanAsyst-Air cantilevers have spring constant of approximately 0.4 N/m and tip radius less of than 10 nm.

b) ScanAsyst-Fluid cantilevers have spring constant of approximately 0.7 N/m and tip radius of less than10 nm (nominal value; max. = 15 nm).

c) ScanAsyst-Fluid+ cantilevers (with a SiNx coated tip) have spring constant of approximately 0.7 N/m, tip radius of 20 nm.

Cantilever chips often contain multiple cantilevers. Examples of layouts for different commercially available cantilever types are shown in Figure 2.9.

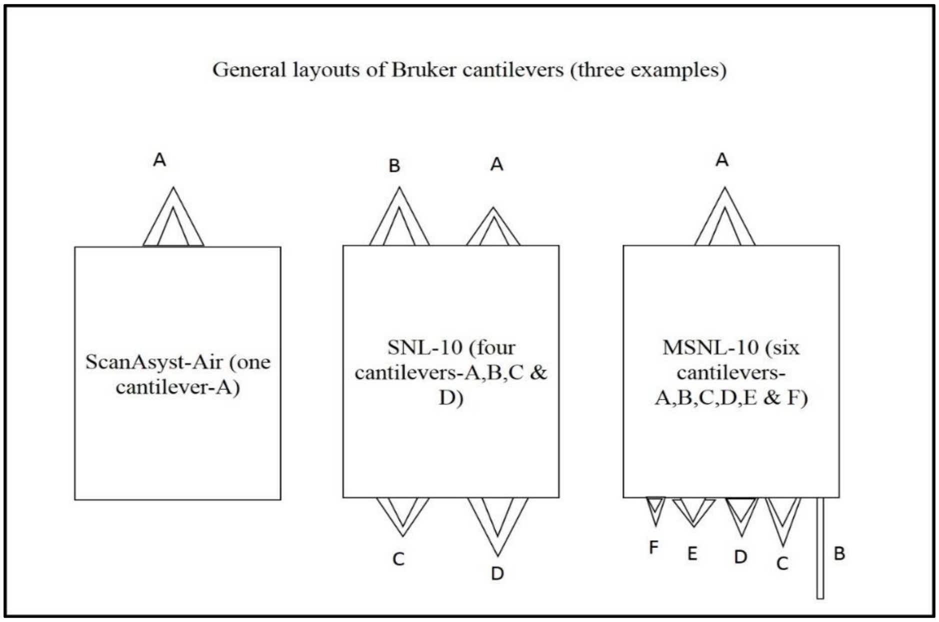

Figure 2.9. Examples of cantilever layout

2.2.3. Bioscope Catalyst Baseplate:

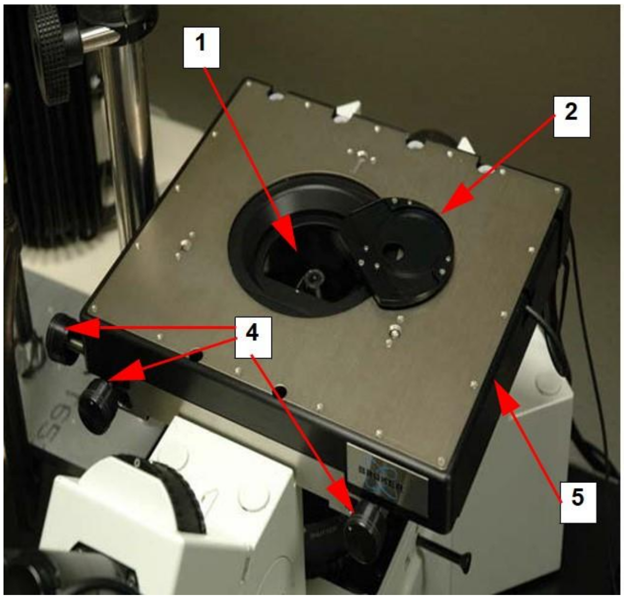

Figure 2.10. Baseplate Components, Controls and Accessories[24]

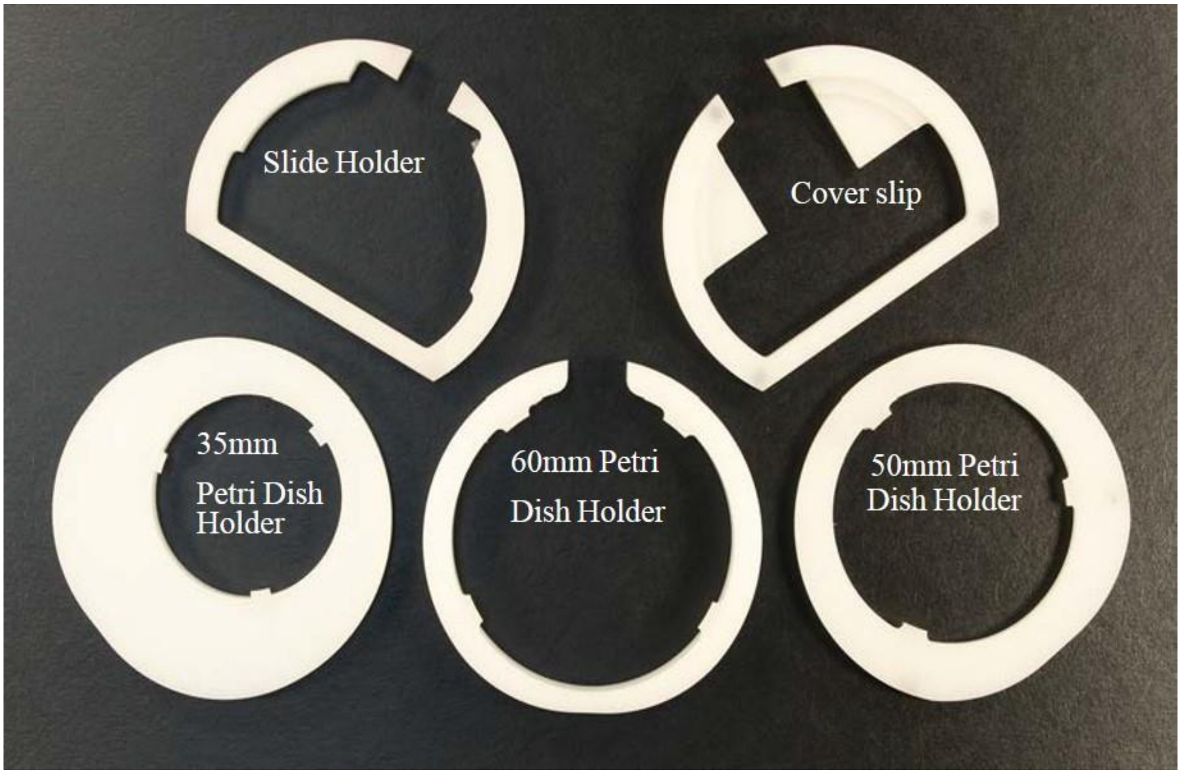

Figure 2.11: Component 3: Sample Substrate Clamps[24]

Component descriptions of the parts shown in Figures 2.10 and 2.11 are as follows:

1. XY stage: The baseplate contains the XY fine positioning stage. Scanner piezo elements control the fine positioning during imaging of a sample. The maximum XY scan range is 150μm. In order to achieve precise imaging, integrated sensors permit closed-loop operation of the scanning stage[24].
2. Sample Holder Plate: The sample holder plate sits in the XY scan stage. There are four magnets in this plate which lock with magnets located under the substrate clamps in order to achieve low noise operation. This plate is removed for weekly clean up procedure.
3. Sample Clamps: Clamps of different shapes depending the nature and shape of the various substrates are available. Clamps for the following five substrates are available.

   a. 25mm ×25 mm microscope glass cover slip.
   b. 25mm x 75mm (1” x 3”) microscope glass slide.
   c. Petri dishes (with 35mm, 50mm and 60mm diameters).

4. Optical Axis Alignment Knobs: Alignment of the SPM axis with the optical axis of the inverted microscope is done by using these knobs.

Motorized coarse motion XY sample stage: Positioning of the sample under the probe tip is executed by computer controlled motors in the bioscope catalyst baseplate. The control is done by the NanoScope V controller which depends on entered values by the user or movement of a joystick. The motor driven adjustment ranges through an area of 6.25mm (0.25”).

2.2.4. Cantilever holders:

Fig 2.12 shows all the cantilever holders in use. This assemblage contains:

- A linking joint to mount holder onto the Z scanner
- A spring clip to hold the probe and allow changing of the probe
- Three gold coated contacts help with electrical connection to tip
- A glass window to see through while imaging in fluid as well as allow the laser access to the cantilever.

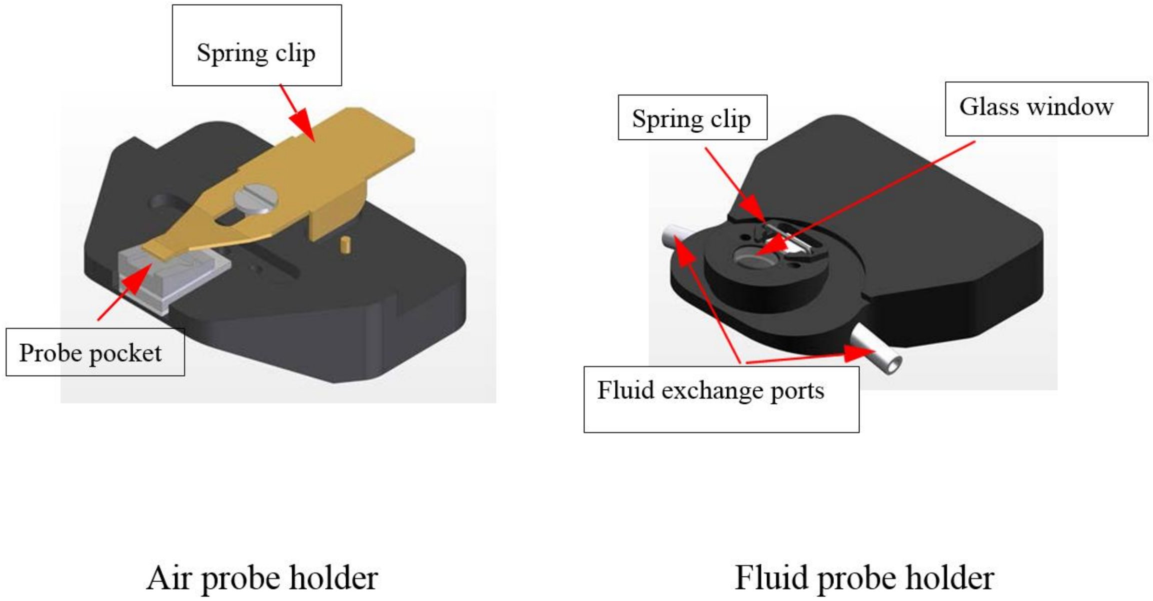

Air probe holder

Fluid probe holder

Figure 2.12. Probe holders[24]

2.2.5. EasyAlign:

EasyAlign is an independently powered unit [24] which allows easy alignment of the laser beam on the back of the cantilever before placing the AFM on top of the optical microscope. A built-in microscope with infrared sensitivity provides an image of the cantilever and infrared laser position. In order to improve the image quality, there are focus and illumination knobs on the side of EasyAlign. The EasyAlign unit also holds a Petri dish and allows the lever to be temporarily stored in solution, as well as the laser to be aligned in solution. This is important, because changes in refractive index of the medium will move the laser spot. When the Bioscope catalyst head is not used, it can kept be in vertical position on the EasyAlign holder.

2.3. Imaging modes:

AFM yields topographical image of the surface of the substrate as well as measures the force of interaction between the cantilever tip and the substrate. AFM imaging can be performed in various modes. Some examples of those modes are contact mode, tapping mode and Peak force QNM mode.

2.3.1. Contact mode AFM:

In contact mode AFM (Figure 2.13), the cantilever tip is scanned over the surface of the substrate and the instrument keeps track of the variation in the deflection of the cantilever with the help of the photodiode detector. A constant deflection between the probe and the substrate is maintained by a feedback loop by vertically moving the piezo scanner maintaining a set point deflection[24]. As a consequence, force remains constant. Force constants of the cantilever typically have values in the range of 0.01 to 1.0 N/m. The force is calculated from Hooke's Law: $F = -kx$ where k = spring constant, F = Force, x = cantilever deflection. Typical AFMs can measure cantilever deflections as low as 0.1 nm, thus the lowest theoretically achievable imaging force is about 1 pN. However, realistic imaging forces are typically of the order of 100-1000 pN.

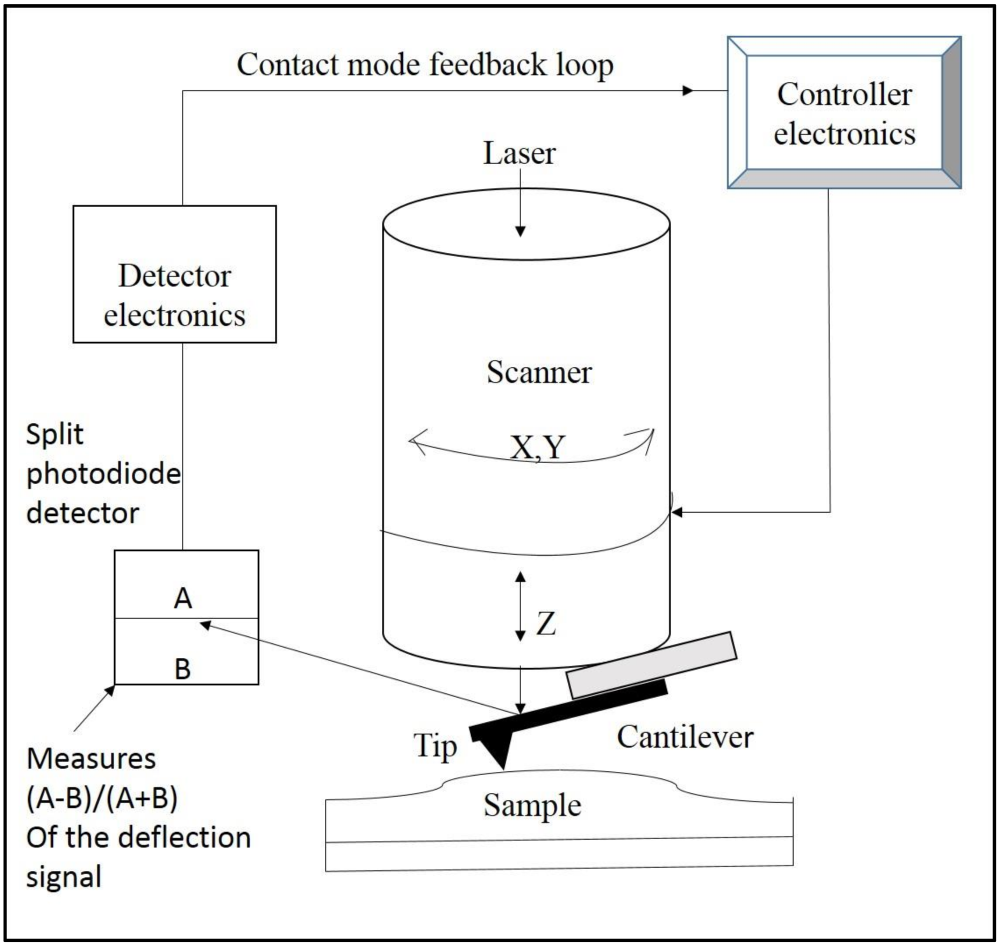

Figure 2.13**.** Feedback Loop Electronics

2.3.2. Tapping mode AFM:

In Tapping Mode AFM (Figure 2.14) the cantilever is oscillated slightly below its resonance frequency with oscillation amplitudes ranging from 20nm to 100nm. At the bottom of the each oscillation swing, the cantilever contacts the substrate while scanning. The feedback loop keeps a constant oscillation amplitude by varying the Z position.

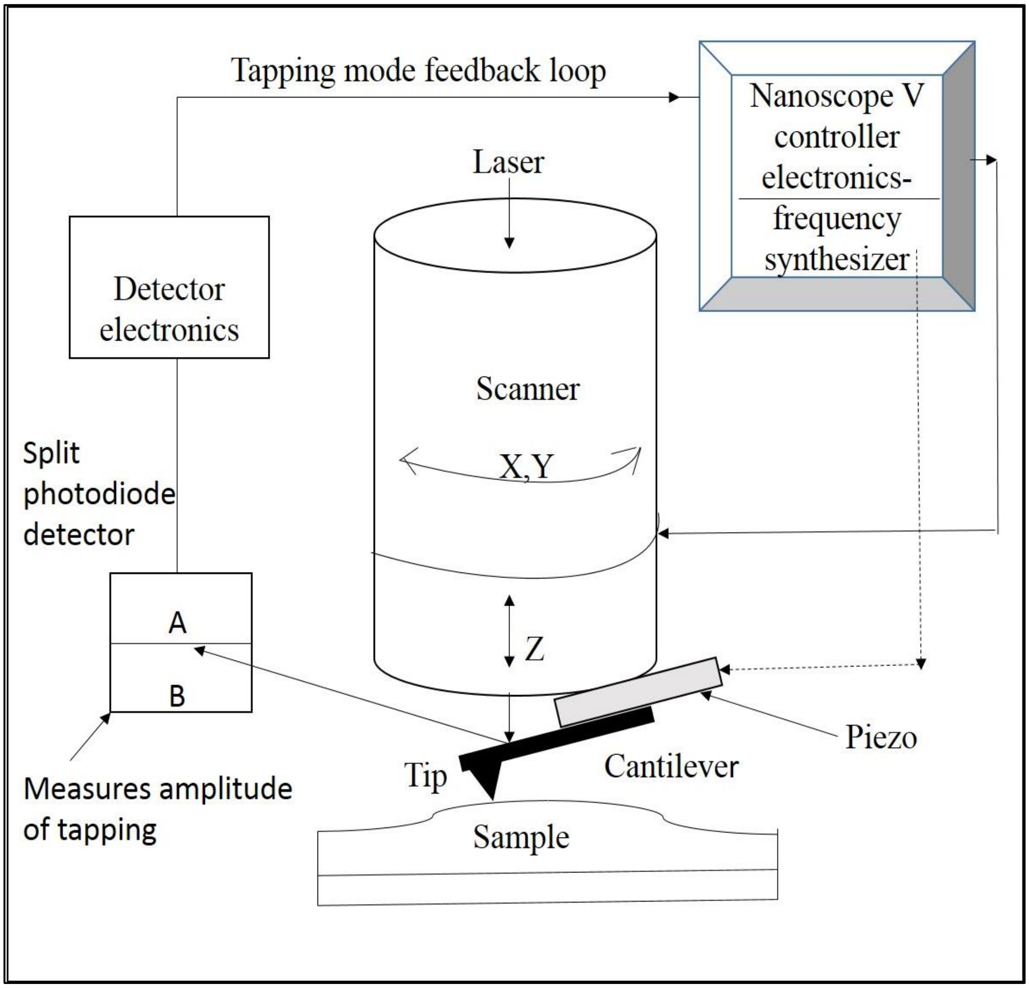

Figure 2.14. Feedback Loop Electronics

2.3.3. Peak force quantitative nanomechanical mapping:

Peak force QNM[25] (following the invention of peak force tapping mode in 1993) is revolutionary relatively new atomic force microscopy modes that comes with the ability of characterizing nanomechanical properties of materials. This imaging and force measurement mode has the ability to map and distinguishing between properties such as Young's modulus, adhesion and dissipation as well as produce high resolution topographical image at the same time. The range of Young's modulus this mode can measure is 0.001-50 GPa and the range for adhesion it can measure is 0.00001-10 μN. This mode is primarily built on the technologies of peak force tapping mode which can control the maximum applied forces on the substrate and thereby prevents damage of both cantilever and substrate. Phase imaging, Dual AC imaging and higher harmonic imaging are other techniques which produce contrast associated with properties of the substrates, but they can't differentiate between properties like adhesion and modulus.

2.3.3.1. Peak force tapping:

Peak force tapping[25] mode avoids the major reasons of damage of sample and cantilever such as the effect of lateral forces exerted by the sample on the cantilever and the application of large vertical forces on the sample. Large normal force can damage the cantilever as well as the substrate. In peak force mode, the probe and sample are periodically brought close to each other and make surface contact for a limited period of time eliminating the lateral force. This mode also regulates the maximum force exerted on the tip to reduce tip wear.

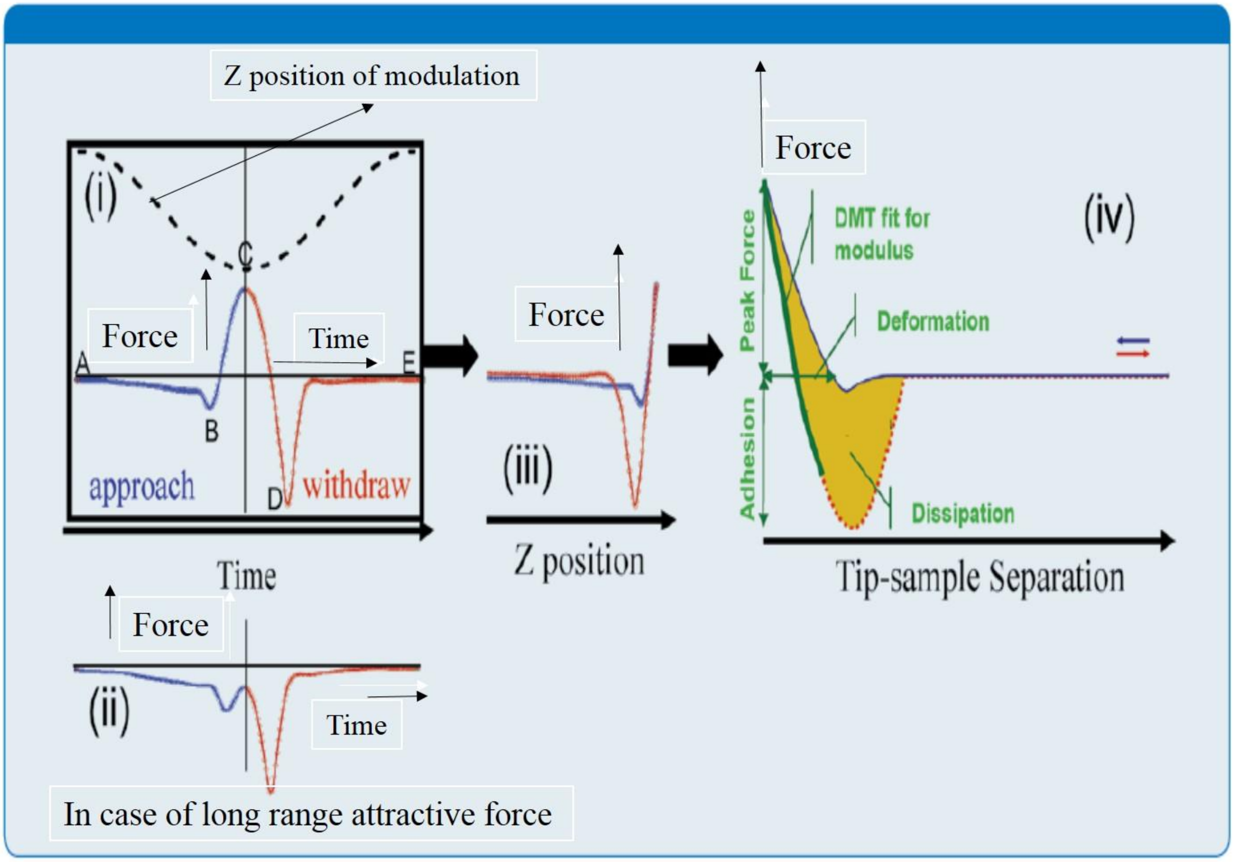

Figure 2.15. Diagrams explaining the principles of peak force tapping and peak force QNM mode[25]

Figure 2.15 (i) shows the force and Z-position versus time during one cycle of the cantilever motion. The dashed line corresponds to the Z-position of the modulation. The solid blue line represents the force exerted on the cantilever during the approach of tip towards the substrate and the solid red line represents the force exerted on the cantilever during the retraction of tip away from the substrate. The duration from A to E is of order milliseconds, i.e. typical frequencies used are far below the resonance of the cantilever and in the kHz range. At point A, tip is away from the surface and there is little or no force on the cantilever. As the approach of tip begins, the cantilever is lowered towards the substrate by attractive forces (shown as negative forces below the horizontal axis at B) such as van der Waals force, electrostatic force or capillary forces. Then the tip contacts the surface and the force rises until it peaks and the Z position of the modulation attains its lowest value at point C in the cycle. The peak force is controlled by the electronics to not exceed a preset peak force setpoint. The cantilever is then pulled away from the substrate and the force keeps decreasing till it goes down to a minimum value at D in the cycle. The adhesion is represented by the force at D. Once the tip comes off the surface at the pull-off point, long range forces can still influence the tip and these forces reduce to the minimum at point E of the cycle where the tip sample separating distance is maximum. As the tip scans over the sample surface, the feedback loop keeps the force at C at a constant value by controlling the Z piezo extension. Thus a constant peak force image is obtained.

Figure 2.15(ii) shows a case where the peak force is smaller than zero due to large long-range attractive forces. The total force is the sum over all of the atoms on the cantilever tip. The tip apex atoms experience a short-range repulsive force as well as a long-range attractive force. However, the peak force mode is still able to distinguish the local maximum and regulate the imaging process even if the peak force is negative.

In Figure 2.15(iii), the force is plotted as a function of the Z piezo motion, while Figure 2.15(iv) shows the force as a function of actual tip-surface separation by taking the cantilever deflection into account. In this plot, we can see how quantities such as elastic modulus, tip-sample adhesion, energy dissipation and maximum deformation can be extracted from the data.

2.3.3.2. Quantitative Material Property Mapping:

The basis of property mapping with peak force QNM[25] is its capacity to capture and analyze an individual force curve at each contact point, as discussed above. The software performs the required calculations “on the fly” and produces images of nanomechanical properties. Through offline analysis functions, we can measure statistics of the mechanical properties. The “High-Speed Data Capture” function enables capture of 64,000 force curves in one cycle of scanning for later analysis.

a) Elastic Modulus:

In order to measure the Young’s Modulus, the retract curve is fitted to the solid bold green line in figure 2.15(iv) using the Derjaguin–Muller–Toporov model (DMT model). The reduced modulus, $E*$, is found as a result of this process and with the actual value of Poisson’s ratio, the Young’s Modulus of the substrate can be directly derived from the software.

$$F - F_{adh} = \frac{4}{3} E^{*} \sqrt{R(d - d_0)^3} \tag{2.15}$$

$$E^{*} = \left[\frac{1 - v_s^2}{E_s} + \frac{1 - v_{tip}^2}{E_{tip}} \right]^{-1} \tag{2.16}$$

Here, R is the tip end radius, $(d - d_0)$ is the deformation, $(F - F_{adh})$ is the difference between forces on the probe and the adhesion force. The Poisson’s ratio usually varies between 0.2 and 0.5 which yields a difference of 4-25% between the reduced modulus and the sample modulus. This mode can measure modulus in the range of 700kPa to 70GPa with appropriate probe selection and calibration.

b) Adhesion:

The adhesion force is represented by the minimum force in figure 2.15(iv). Any attractive force between the tip and substrate can cause this force. The adhesion rises with higher tip radius. Simple models assume the adhesion to be changing proportionally with the tip end radius. The area which is located beneath the zero force reference and above the withdrawing curve is defined to as ‘the work of adhesion’. Adhesion force is a very significant quantity if the tip is decorated with molecules or functionalized where the adhesion represents the interaction between molecules attached to the tip and sample.

c) Dissipation:

Energy dissipation is defined as the force multiplied by the probe velocity integrated over one period of the vibration (indicated by the golden region in the figure 2.15.(iv)):

$$W = \int \vec{F} \cdot d\vec{Z} = \int_0^T \vec{F} \cdot \vec{v} dt \qquad (2.17)$$

Here *F* represents the force vector, *dZ* stands for the displacement vector and *W* represents amount of energy dissipated in a complete interaction cycle. For ideal elastic deformation, hysteresis can’t exist between the repulsive regions of the loading-unloading curve. As a consequence of this situation, work of adhesion emerges as a major contributor to energy dissipation.

d) Deformation:

The maximum deformation is defined as the piercing of the tip into the substrate at the peak force (after getting rid of cantilever compliance). As the force on the sample increases, the deformation goes up to a maximum value at the peak force. We calculate the maximum sample deformation from the difference in distance from the point of zero force to the peak force point following the approach curve (in figure 2.15.(iv)).

2.3.3.3. Calibration of the spring constant:

Spring constant values can vary significantly for the same type of lever and deviate from values provided by the manufacturer. The reason of this big difference between them is the fabrication techniques of the cantilevers. AFM cantilevers are manufactured similar to electronic chips. The manufacturing process involved etching, which results in small variations in cantilever dimensions. As seen in equation (2.5), the cantilever stiffness depends on the cube of the thickness. Thus, even small differences in the etched thickness of the cantilever can change the cantilever stiffness by a significant measure.

This is why proper calibration methods for obtaining the stiffness of the cantilever accurately are extremely important in order to calculate and interpret measured forces by AFM. Various techniques can be used to calibrate the cantilever spring constant: thermal approaches, loading and geometry-based methods. One of the major sources of AFM noise is thermal motion and it can be exploited for achieving the accurate value of the cantilever stiffness. In thermal approach, the cantilever can oscillate freely under the thermal influence. The cantilever can be modeled as a harmonic oscillator with a single degree of freedom and spring constant of approximately $\frac{K_B T}{<x^2>}$. Here K_B represents the Boltzmann constant, T represents the medium temperature and mean square cantilever deflection is represented by $<x^2>$. Voltage variations caused by the photodiode (as a result of cantilever's deflection over specific time period) is measured by an oscilloscope. Those data can be transformed into deflection by the use of the photo diode sensitivity factor. Deflection sensitivity factor is usually calculated by a force curve taken on a solid substrate. From the Fourier transform of the time domain data (totaled and averaged upon a wide frequency range), we end up with a resulting amplitude peaking around the cantilever resonant frequency.

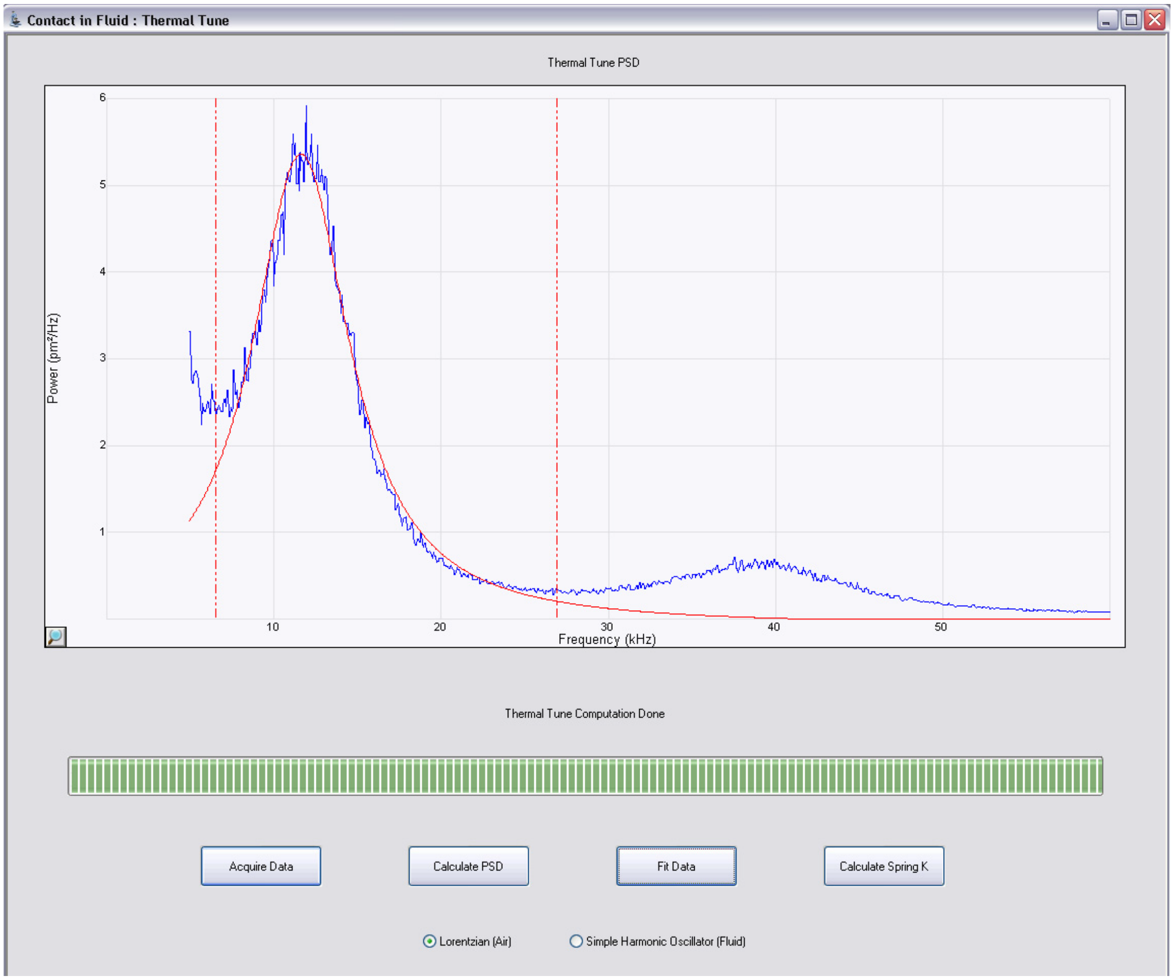

Thermal Tune Computation Done

● Lorentzian (Air) ○ Simple Harmonic Oscillator (Fluid)

Figure 2.16. Calibration in air[26]

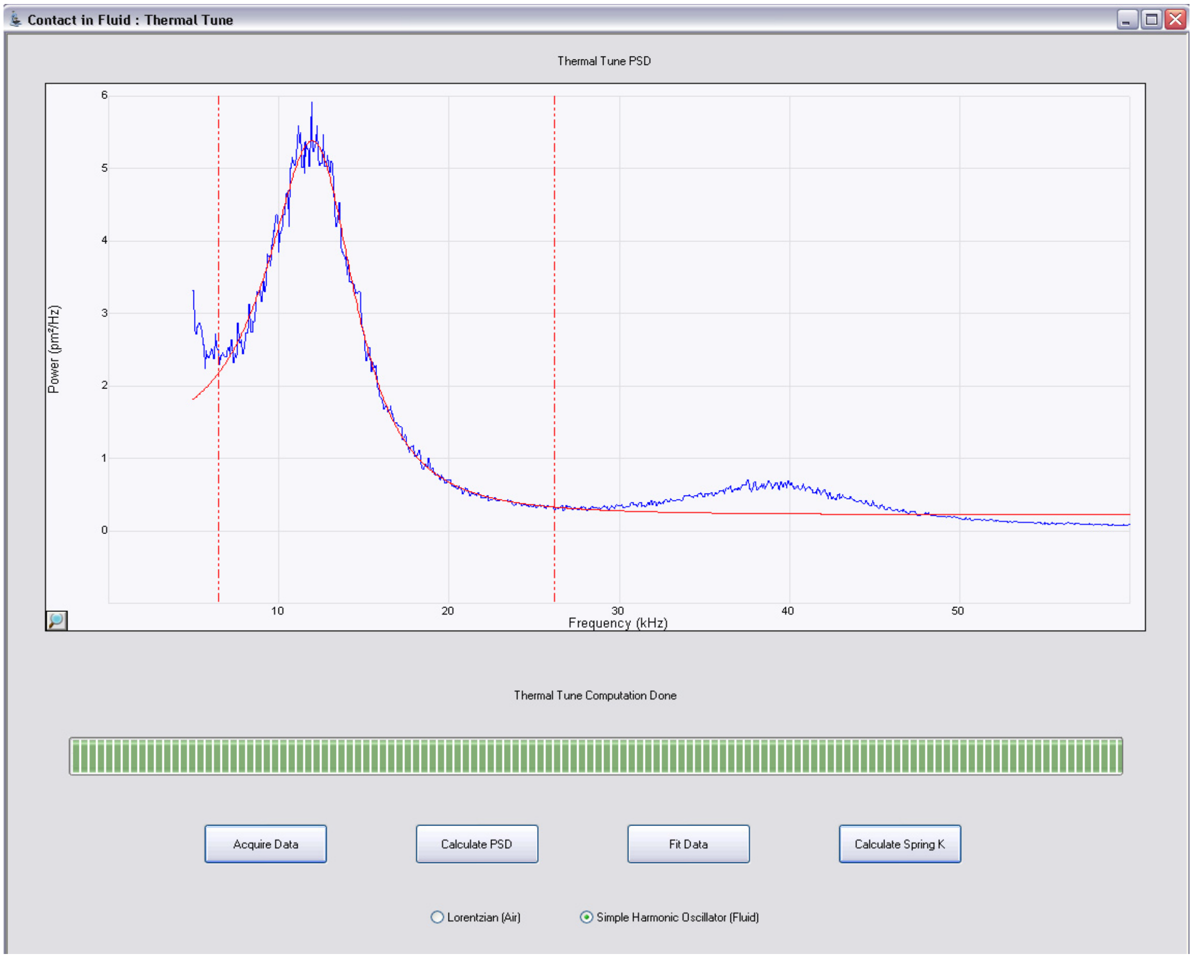

Thermal Tune Computation Done

○ Lorentzian (Air)

● Simple Harmonic Oscillator (Fluid)

Figure 2.17. Calibration in liquid[26]

The Lorenzian equation is used to fit the data for air imaging:

$$A(\nu) = A_0 + \frac{C_1}{(\nu - \nu_0)^2 + C_2} \tag{2.18}$$

Where A_0 = the baseline amplitude, $A(\nu)$ defines the amplitude as a function of frequency ν, ν_0 represents the center of the resonant frequency and C_1, C_2 represent fit parameters.

The simple harmonic oscillator equation used to fit the data for liquid imaging is:

$$A(\nu) = A_0 + A_{DC} . \frac{\nu_0^2}{\sqrt{(\nu_0^2 - \nu^2)^2 + \frac{\nu_0^2 \nu^2}{Q^2}}} \tag{2.19}$$

Where A_0 = the baseline amplitude, $A(\nu)$ = the amplitude as a function of frequency ν, A_{DC} represents the amplitude at zero frequency, ν_0 represents the center of the resonant frequency and Q represents is the quality factor[26]. Once the amplitude of oscillation is determined, we can also determine the root mean square of cantilever oscillation too. By using the formula, mentioned in the beginning of this section, the cantilever spring constant can be determined.

2.3.4. MIRO:

MIRO[27] stands for “Microscope Image Registration and Overlay”. This is an interactive software which allows us to register optical and AFM images. Multiple optical mages from same device or other devices may be imported and overlaid with AFM images. We can define regions of interest on the optical images (Figure 2.18), and then direct the AFM to image these regions. To get perfect agreement of optical and AFM images, registration parameters, such as position, angle and stretch need to be determined by an initial calibration process.

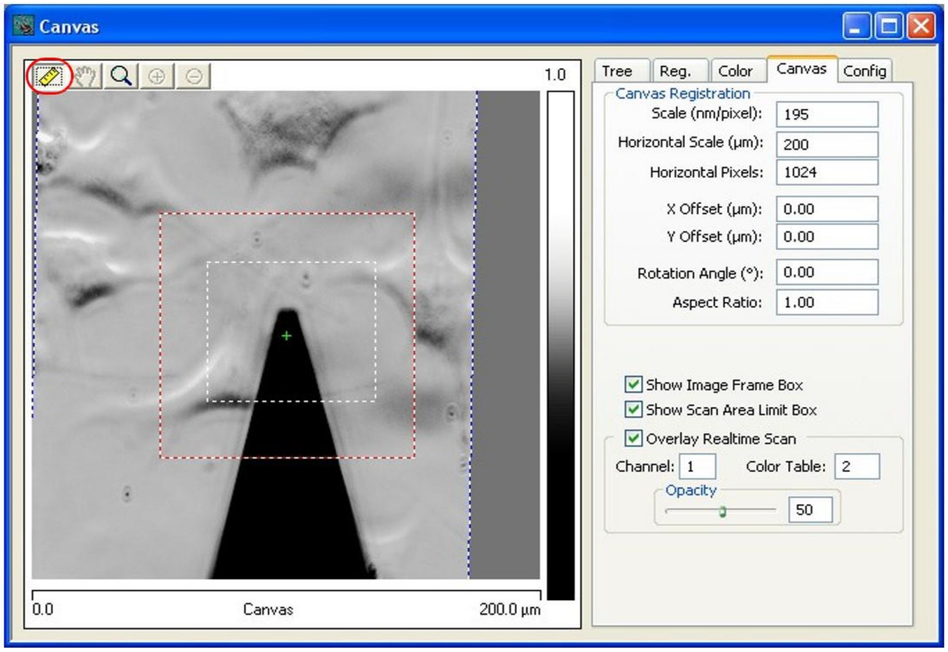

Canvas Registration

Scale (nm/pixel): 195

Horizontal Scale (µm): 200

Horizontal Pixels: 1024

X Offset (µm): 0.00

Y Offset (µm): 0.00

Rotation Angle (°): 0.00

Aspect Ratio: 1.00

☑ Show Image Frame Box

☑ Show Scan Area Limit Box

☑ Overlay Realtime Scan

Channel: 1

Color Table: 2

Opacity: 50

Figure 2.18. Canvas view of MIRO software[27]

2.4. TOTAL INTERNAL REFLECTION FLUORESCENCE MICROSCOPY (TIRFM):

2.4.1. Fluorescence Microscopy:

Fluorescence microscopy is a branch of optical microscopy that exploits fluorescence to generate an image and characterize different properties of the sample. The specimen in this kind of microscopy is initially radiated with UV or laser light. Fluorophores absorb that light and emit light of longer wavelengths and different colors. Fluorescence microscopes usually comprise of a light source, an excitation filter, a dichroic mirror or beamsplitter and the emission filter. The light source is usually a Xenon or mercury lamp, but can also be a laser (Fig 2.19). The incident light is separated from the emitted fluorescence (with a smaller frequency) via spectral emission filter. The filters and the dichroic mirror are selected according to the spectral excitation and emission behavior of the fluorophores. The distribution of a single emission color is imaged and finally different color images, corresponding to different fluorophores can be overlaid.

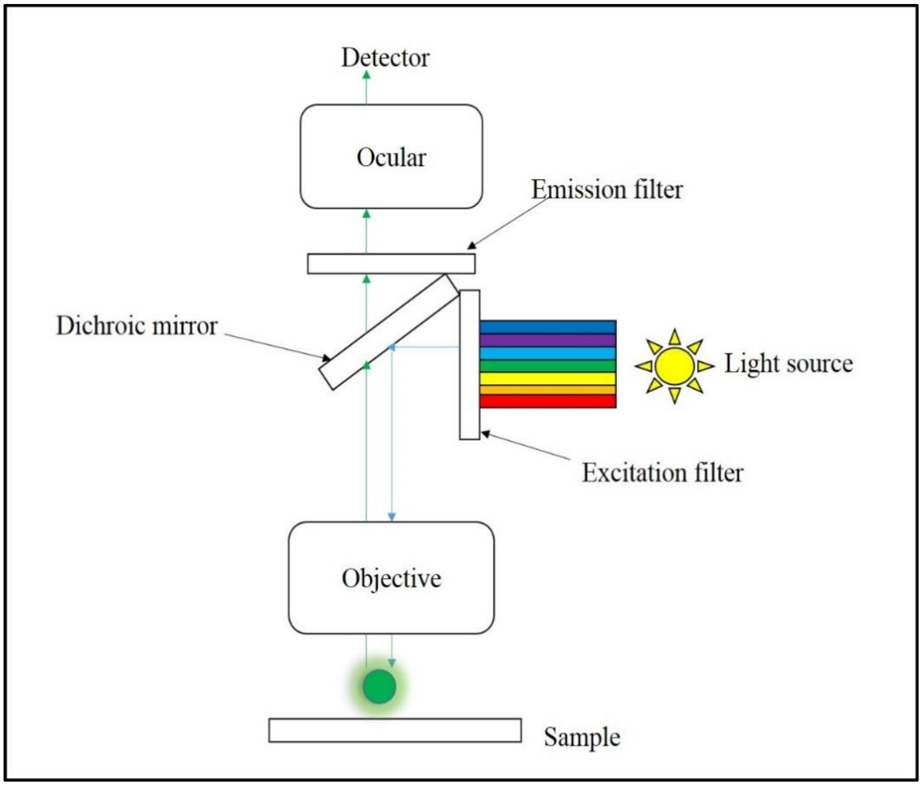

Figure 2.19.Schematic Diagram of Fluorescence Microscopy

2.4.2. Advantages of combining AFM and Fluorescence Microscopy:

The Atomic Force Microscopy, a very important tool in Biophysics, is a high resolution imaging technique which can measure forces down to nanoscale. But it doesn’t provide time resolution and functional specifications as good as fluorescence microscopic techniques. If these two methods are combined and synchronized, we can use their advantages to solve many unanswered problems in biophysics. AFM can measure molecular recognition forces which sheds light into structural and functional mechanisms of bio-molecular aggregation. In addition AFM, if combined with fluorescence microscopy[28] can recognize biomolecules depending on fluorescence labeling and high-resolution topography imaging.

2.4.3. Total Internal Reflection Fluorescence Microscopy:

Total internal reflection fluorescence microscopy (TIRFM) is an important technique that reduces noise to a large degree and improves the optical axial resolution quality significantly (of the order of 100nm) over the conventional confocal microscopy techniques (0.5 micrometer). This is primarily due to the fact that this technique can confine fluorescence only to the molecules in a thin region just above the substrate–sample interface by restricting the excitation light to that region.

2.4.3.1. Theory of Total Internal Reflection Fluorescence Microscopy:

When a light wave is incident from a medium of higher refractive index (for example glass, n =1.5) to a medium of lower refractive index (for example water, n =1.3), a certain amount of light is transmitted into the medium of lower refractive index and another certain amount of light is reflected back into the medium with higher refractive index (Fig 2.20). The amount of transmission and reflection depends on the angle of incidence and the difference between the refractive indices. The refraction angle follows Snell's Law:

$$n_1 \sin\theta_i = n_2 \sin\theta_t \tag{2.20}$$

where θ_i is the angle of incidence and θ_t is the angle of transmission.

When angle of incidence = critical angle (θ_c), the angle of transmission will be 90° and the refracted light grazes across the glass water interface. The critical angle will be approximately 61°-63° for glass water interface.

$$\theta_c = \sin^{-1}\left(\frac{n_1}{n_2}\right) \tag{2.21}$$

If the angle of incidence is greater than the critical angle, an interesting phenomenon happens. The incident light is entirely reflected back into the initial medium of higher refractive index. This is termed as total internal reflection. Using Maxwell's electromagnetic wave equation, it can be proven that this kind of situation generates a special kind of wave called evanescent wave. This evanescent wave is generated in the water medium and travels horizontally along the glass water interface. It penetrates the water surface with an exponentially decaying intensity and moves away from the interface. The decaying intensity along *z* direction is given by

$$I(z,\theta) = I(0,\theta)\exp\left(-z/d_p\right) \tag{2.22}$$

$I(0,\theta)$ is the intensity of the incident light at incident angle and z=*0*.

$$d_p = \frac{\lambda}{4\pi\sqrt{n_2^2 sin^2\theta - n_1^2}} \tag{2.23}$$

λ is referred as vacuum wavelength and d_p is the penetration length. The latter signifies the distance over which the intensity of the evanescent wave falls off to 1/e of its value at the glass water interface. The main advantage of evanescent-wave imaging is its capacity to excite only fluorescent molecules that are situated at or extremely close to the glass–water interface. Noise arising from Raman scattering or background blurring from fluorescent molecules, positioned away from the focal plane are eliminated in this TIRF method.

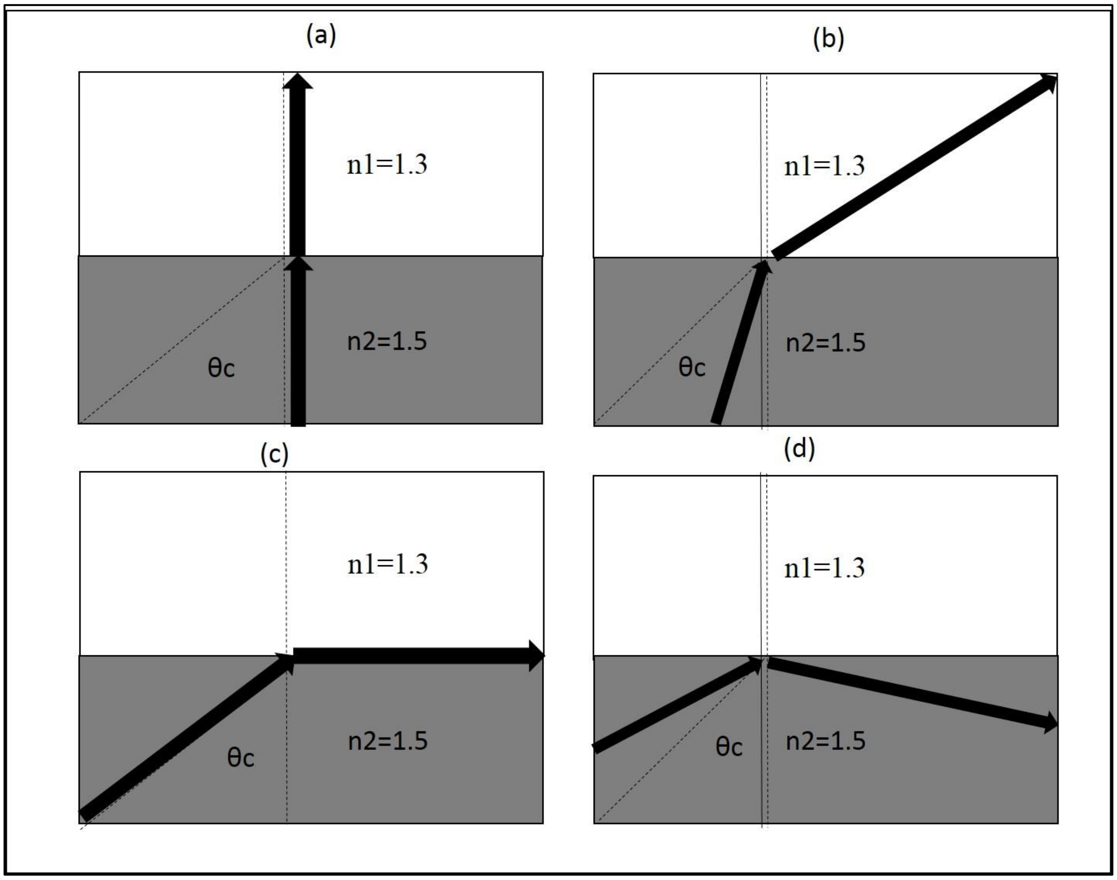

Figure 2.20. (a) Light wave is incident normally from glass (n =1.5) to glass-water interface and it is transmitted normally to water (n =1.3), (b) The transmitted light wave is refracted into water at an angle which is greater than its angle of incidence at the interface, (c) The angle of incidence is the critical angle here and it's approximately 60° for glass-water interface. The angle of refraction is 90° and the transmitted light wave grazes at the glass-water interface, (d) The angle of incidence is greater than the critical angle. So the entire incident light is reflected back to the glass media. This event is mentioned as total internal reflection.

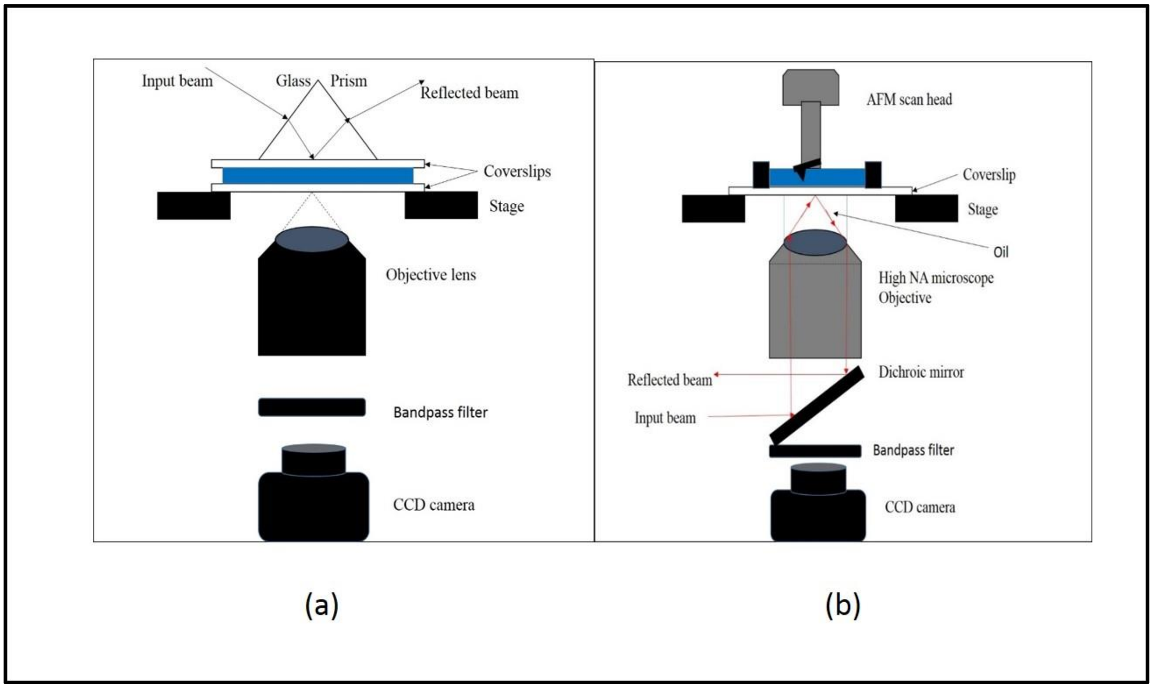

Figure 2.21.: Schematic diagrams of the three basic TIRF microscope configurations (not to scale). (a) In the prism-based geometry, a beam of light is directed through a prism (with high index of refraction such as glass or sapphire), which has been optically coupled to a glass cover slip with a thin layer of index-matching oil. (b) The objective-based TIRF microscope requires the use of objectives with an NA .1.3.

2.4.4. Combining AFM & TIRFM:

The idea of combining complementary capabilities of AFM and TIRFM[29, 30] opens up possibilities in biophysics towards understanding critical cellular interaction phenomena. While AFM provides the capability of manipulating single cell or bio-macromolecule, TIRFM can be used to analyze the resulting effects. Multiple studies in this area capture different features and applications, such as:

(a) TIRF can capture cell response to localized mechanical stimuli generated by an AFM tip. Similarly, an AFM tip with long aspect ratio can deliver small macromolecules into living cells without significant damage. TIRFM can monitor the molecular dynamics inside the cell.

(b) Mathur et al.[31] used TIRFM to observe redistribution of basal membrane focal contacts as well as focal contact area increase while applying nano-Newton range forces to the apical membrane of adhering endothelial cells using an AFM cantilever.

(c) Similarly, AFM cantilever has been used as an intracellular injector tool for delivering single fluorescent beads into live BALB/3T3 cells. Observations were made using TIRFM and it is clear that this combined process can be used for targeted gene manipulations.

(d) Recently developed technique called evanescent nanometry involving AFM and TIRFM can be used to study mechanical forces related to single molecules inside living cells. This technique essentially exploits the depth-dependent intensity profile of the evanescent wave.

All these studies demonstrate that AFM and TIRFM provide complementary knowledge about a biological system that cannot be extracted if they are used independently.

In our research, we will use a new AFM-TIRF combination to validate our recognition imaging and single molecules force measurements, by specifically labeling target proteins with fluorescent tags.

CHAPTER 3: AFM ON LIVE CELLS

3.1. Introduction:

After its invention (more than a decade ago), atomic force microscopy (AFM) quickly became an efficient technique to image and manipulate biological samples. AFM has helped to discover new information about cell mechanics, cell division, shape, signaling, adhesion and tissue development. With the ability to perform experiments on samples in various temperature ranges and in liquid, AFM allows imaging and probing biological substrates in physiological environment (perfect moisture, temperature 37 degree Celsius, pH 7.3, combination of air and 5% of CO_2 and an environment without contamination). Foremost application of this technique in biology has been high resolution imaging. AFM has also been used to apply forces to cells to obtain information about their mechanical and adhesive properties and the cell's response to mechanical stimuli.

3.2. Single-molecule measurements on live cells:

Different techniques of microscopy have been used to directly observe different sections of the cell and single molecules[1, 32, 33]. Single-molecule spectroscopy in vivo can lead to new information about molecular processes which form the groundwork of the physiology of a cell. This permits us to picture the distribution of molecules with nanometer resolution in the cell as well as helps us to characterize their motion with very high precision. Single molecules may be traced with epifluorescence microscopy or total internal reflection fluorescence (TIRF) and photo-Activation (PA)[34] . High spatial resolution may be achieved by using a super-resolution imaging that can locate a fluorophore with very high resolution far beyond the diffraction limit. An example of such a technique is stochastic optical reconstruction microscopy (STORM)[35] .

Single-molecule imaging of cells in vitro permits us to study and learn about of single molecules in a regulated environment. This setup is different from the environment of a cell in vivo. In order to know more information about the intracellular localization, we can use fixation methods to measure the distribution of single molecules inside cell but the measurements on fixed cells do not usually provide any information about the temporal dynamics of molecules. Techniques used for identifying and tracking single molecules in live cells are as follows:

a) Using labeling: By using a particular marker adhering to a molecule, the molecule can be tracked. One of the most widely expressed detection strategies is fluorescence microscopy. Fluorescently labeled molecules may be obtained by attaching a fluorescent dye to the target molecule. This process is used if cultured cells are being imaged. Fluorescently labeled molecules can also be microinjected into live cells or antibodies can be applied on cells fixed on a surface. Specificity of labeling can be very high which means only the labeled proteins are fluorescent. We can also use different fluorescent molecules to image different protein molecules at the same time. In order to detect signal generating from single molecules, bright fluorescent markers should be used as that signal should be stronger than the background fluorescence created by other molecules inside cell.

b) Using isolation of single molecules: In order to confirm the source of the generated signal and distinguish it from background signal, the intensity of the measured fluorescence signal and a reference signal obtained on single fluorescent molecules are compared. By controlling the particle functionalization carefully, the presence of one linker for each particle can be assured.

c) Using TIRF: Total Internal Reflection Fluorescence (TIRF) microscopy depends on the principle of selective illumination of a thin portion of the sample. The function and principle of this technique are described in detail in a previous chapter. The background fluorescence which is mainly generated by molecules which are out of focus is lowered in this technique. This technique leads to increased signal-to-noise ratio and helps to identify weaker fluorescence signal generated by single molecules. The evanescent wave in TIRF microscopy restricts the analysis to structures of cells located very close to the glass coverslip–sample interface.

3.3. Imaging cells (live and fixed) and cellular segments:

Studies conducted on cell surfaces using AFM have yielded promising results[1, 32, 33]. Maintaining cells for AFM experiments does not generally need chemically labelling of cells. Cells are usually kept in culture medium during AFM experiments which gives the users several hours of time for experiment. AFM, as a label-free way to obtain high-resolution images of live cells, has been applied to image a diverse range of cells and cell lines. For cell imaging in vitro, AFM needs the cells to be properly attached to a surface (usually to the bottom of a Petri dish) to prevent its displacement by the cantilever while being scanned.

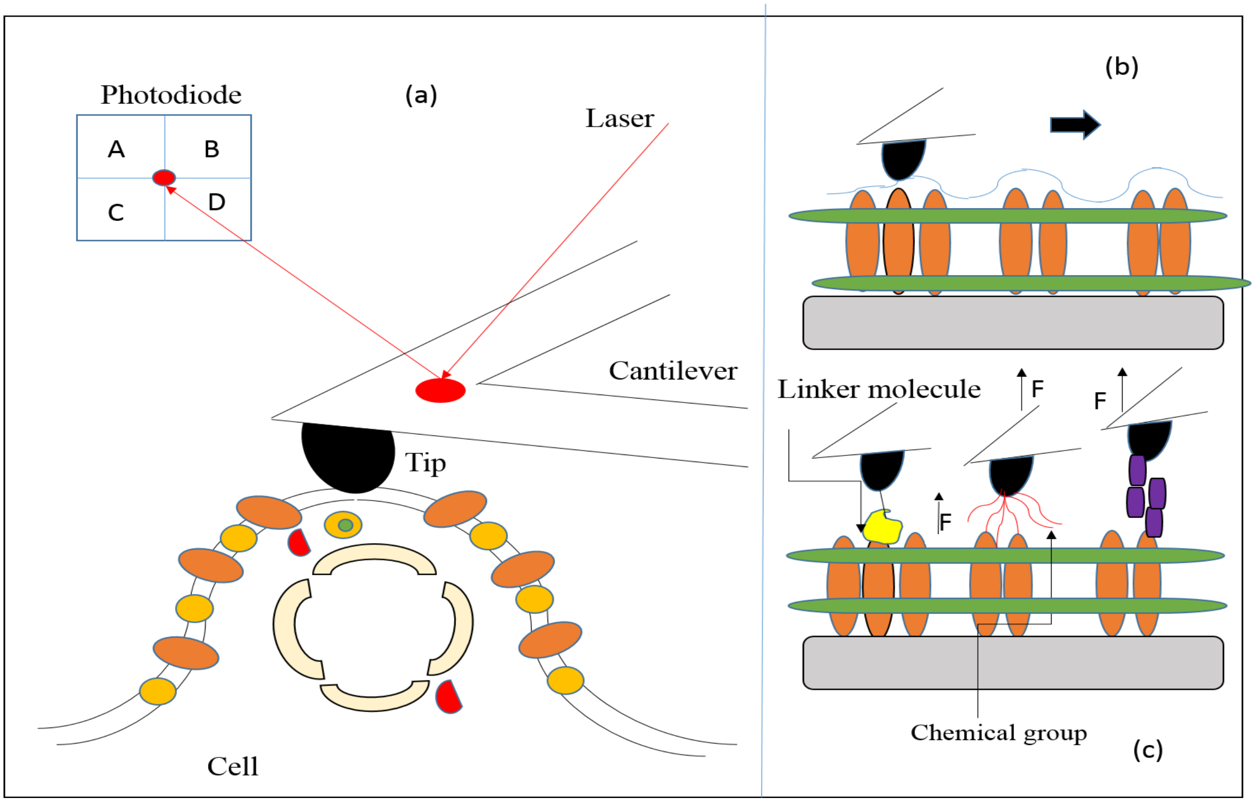

Figure 3.1.AFM-based nanoscale microscopy technique of live cells. (a) AFM characterizes a sample by detecting the small interaction forces between the cell surface and the cantilever tip. (b) The AFM tip is scanned through the surface of the cell (arrows) in order to receive the surface topography (indicated by dashed line). (c) The cantilever tip is applied for the measurement of cell-surface interactions. Examples display a functionalized tip: left most tip is tagged with a ligand to measure interaction forces with its cognate receptor, middle tip is functionalized with chemical components in order to figure out chemical interactions and right most tip is decorated with cell-adhesion molecules in order to figure out interactions between hemophilic or heterophilic components and other cell-adhesion molecules.

Fibroblasts or epithelial cells which are very adherent may be directly imaged on coated or uncoated glass plates or dishes. Non-adherent or weekly adherent cells can be immobilized on poly-L-lysine coated glass plates or Petri dishes. Yeast and bacteria (suspension cells) may be immobilized using membranes and microwells. However, only the top surface of the cell is available for AFM imaging. The largest concern about using cantilever tip on cells is that it can damage the cell or cell membrane. This concern is reduced by adjusting AFM scan parameters such as choosing low scan speed and force, and using compatible cantilever tips (not too sharp). Experiments with dyed cells have helped to conclude that the cantilever tip does not permeate the cell membrane or influence the cell behavior negatively [36].

However, hours of live cell imaging may reduce the AFM lateral scanning resolution. Even the softer cantilevers used for live cell imaging are ten times stiffer compared to cell membrane. Therefore, it is crucial to keep the scanning force below or equal to 50 pN to keep the cantilever tip from invading the membrane and damaging intricate cellular structures. Chemical substances like glutaraldehyde cross-linkers can restore these flexible structures while imaging the sample with cantilever. These types of chemical fixation techniques increase the stiffness of the cell membrane.

AFM tips which are not sharp (with tip radius of approximately 20–50 nm) produce better images of biological samples compared to sharp tips (with tip radii less than 10 nm), because of the lower pressure exerted on the cell. However, there is a tradeoff, since the maximum imaging resolution is ultimately determined by the tip radius, i.e. if the tip is too blunt, imaging resolution is also reduced. Usually low cantilever tip velocity as 2μm/s will enhance the quality of sample. In live cell imaging, the scanning force applied influences the detailed description of cell structure reported in AFM images. With increasing scanning force, the cantilever tip will disrupt the cell membrane and push it against the comparatively stiffer cortical actin cytoskeleton.

3.3.1. Analysis of the dynamic cellular procedures:

An intriguing use of AFM is to monitor morphological changes linked with dynamic restructuring of the plasma membrane [36]. For example, AFM time lapse imaging of live cells exposes dynamic membrane events associated with neurite extension[37]. These type of interactions between intercellular protuberances and extracellular matrix constituents can be pursued with single molecular level resolution. Even granula fusion during platelet activation can be detected using this method[38]. One of the drawbacks of time-lapse experiments is that it takes several minutes to acquire data. This time issue may be resolved by reducing or modifying numbers of pixels per scan line. AFMs which have z scanning range of 15–20 μm are capable of tracking membrane structures[1, 32, 33] with lower heights as well as higher regions of the cell. Comparatively flatter regions of cells may be scanned with lower acquisition time. Recently, ultrafast AFM methods have been developed, but they work best on very flat samples, such as purified proteins.

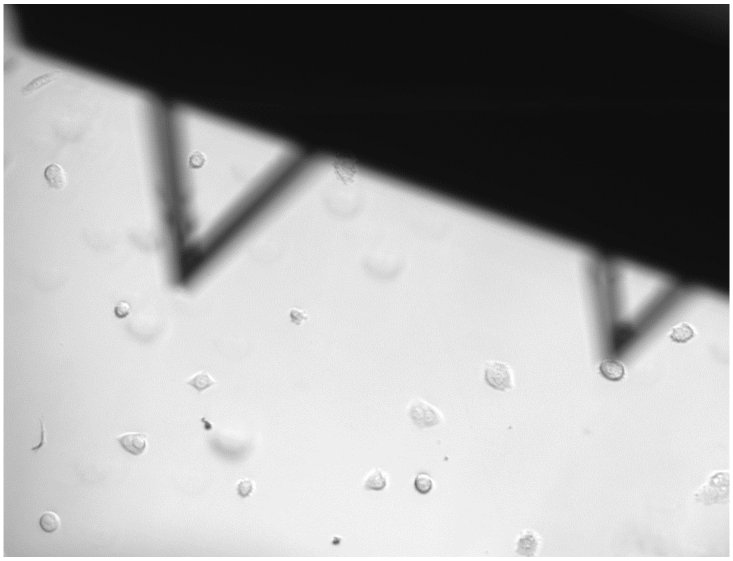

(a)

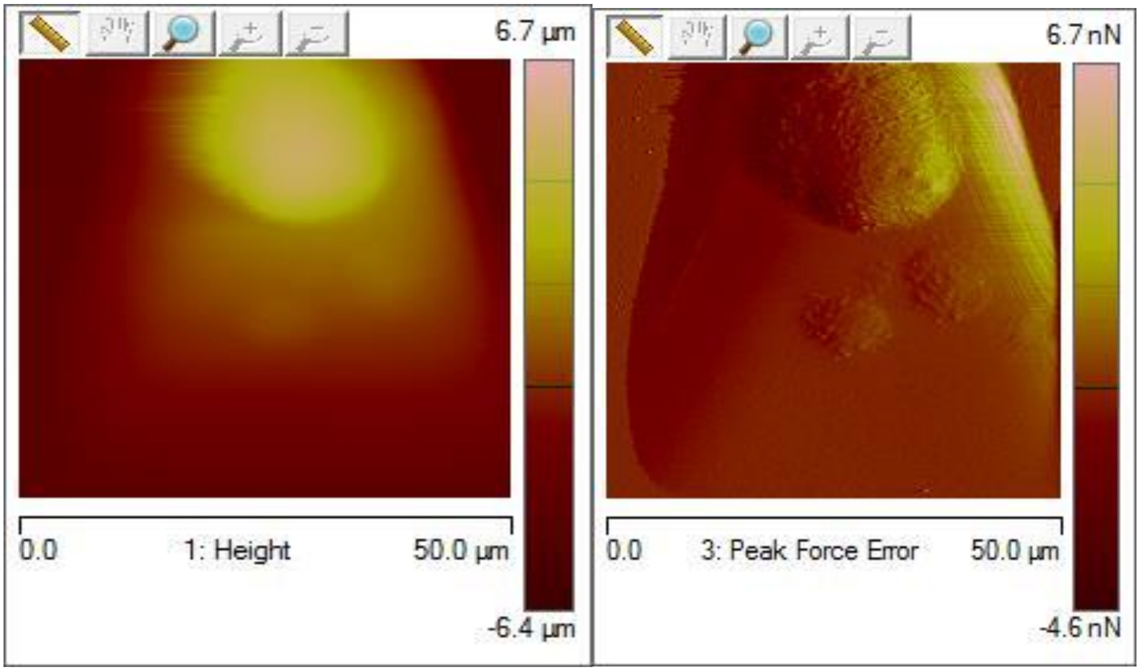

(b) (c)

Figure 3.2.(a) represents the field of view where we can see the AFM cantilever tip (DNP-C cantilever from Bruker corporation) scanning on top of BXPC-3 cells, (b) represents height image of that particular cell, tip is scanning on; (c) represents deflection error image of that particular cell. Average size of those cells are 25-30μm. Both (b) and (c) are 50×50 μm^2 images.

3.3.2. Discovering cellular compartments:

AFM is most frequently used to study the extracellular portion of membrane. It has also been applied to image the compartments located inside the cell. In order to make intracellular cellular pockets available for AFM imaging, these can be accessed by the use of procedures like hydrodynamic shear, which ruptures the cell. If the intracellular components stay attached to the support after opening up the cell, AFM scanning can be performed. Components like nuclear pore compound ion channels can be isolated on glass or mica substrate for AFM scanning.

3.4. Measurement of cell adhesion at single cell level:

AFM (as force spectroscopy technique) may be applied to characterize molecular mechanisms behind cellular adhesion of live cells and cell–cell interactions. For single cellular force measurements, a live cell is fixed to a tipless lectin-functionalized cantilever[39]. Another approach is to culture the cells on the cantilever for hours before experimental measurements[40]. The cantilever (with cell adhering to it) is brought close to the surface of a cell located on a substrate until they are in contact.

After some incubation time, the cantilever with attached cell is pulled back with a constant speed and a force-distance curve is registered. These curves yield the maximal detachment force. These detachment forces can be registered over at least four orders of magnitude using AFM[39, 41].

The smallest trackable rupture events correspond to the detachment of a single receptor-ligand system. A dynamic force spectrum can be produced by probing these receptor-ligand interactions over a large range of pulling speeds[42]. The receptor-ligand bond strength and life time, and the potential barrier width can be obtained using Standard theory or Bell Evans theory of bond rupture under application of a force (see Chapter 4). The specificity of the interaction can be assured by the use of blocking antibodies or excess free receptor or ligand[36].

3.5. Deformation of cell membrane by pulling in AFM experiments:

The force needed to deform a cell membrane is at first approximation determined by the Young-Laplace equation, if we see the cell as a bubble. This equation relates the shape of the bubble to the pressure between inside and outside a curved interface and the surface tension of the interface:

$$\Delta P = \gamma \left(\frac{1}{R_1} + \frac{1}{R_2}\right) \tag{3.1}$$

where R_1 and R_2 are the principal radii of curvature, and γ stands for surface tension. However, in the context of membrane deformation by the AFM cantilever tip, analysis for an actual deformed cell shape is a quite complex geometrical problem due to the deformed shape. For example, an indentation model was presented by Discher et al.[43] using a number of simplifying assumptions such as that higher order effects of bending were neglected and the primary resistance against indentation was assumed to be isotropic. Beyond the complex geometry, the membrane deformation problem gets further complicated due to the influence of the cytoskeleton. However, under small deformation condition, the relationship between force of deformation and the deformation of cell membrane remains fairly simple. Discher et al.[43] arrived at a cubic relationship to fit experimental observations of force under different cell membrane indentation where the coefficients depend on the amount of pre-stress, membrane dilation modulus and tip geometry.

Scheffer et.al.[44] looked at cell membrane deformation under pulling conditions. They found that a linear function represents the force vs. deformation relationship quite well, where the constant slope involves the bending modulus. Hence, the (linearly) fitted curve can be used to estimate bending modulus. A concave deformation is caused in the cellular membrane by indentation of the cantilever tip into the membrane and the indentation decreases when the tip is retracted at a constant speed. In this approach, the model of the axisymmetric bending of a thick annular plate model was used to describe the bending of cell membrane due to pulling.

In general, a polynomial fit can be used to fit force profiles upon pulling on a cell membrane, as long as the pull distance is short (not exceed a few 100 nm). Also, the experimental time scale must be quite fast and not give the cell time to internally rearrange its cytoskeleton.

Under these conditions, the pull force is determined by purely physical properties of the cell membrane and cytoskeleton. In practice, we can follow the approach taken in Mayyas et al.[45], where the non-linearity of the force profile due to the presence of linkers was fitted to a parabolic equation, and the fitting parameters were explicitly included in the subsequent analysis of the force data. In this view, the membrane deformation just changes the force profile as we pull on a bond, and can be fitted in the same fashion. Since we measure the force profile, we can fit each profile individually, extract the fitting parameters (α, k_t and k_{app}) from BE-WLC model, average them and then calculate our kinetic parameters of the bond rupture.

CHAPTER 4: BACKGROUND AND THEORY OF FORCE SPECTROSCOPY

Complex bonds can be studied by using AFM in the force-distance mode. In this mode, a force is applied to the bond between two molecules, until the bond breaks. The force at which the bond breaks is called the rupture force. The applied force deforms the activation barrier of the interacting molecules and changes the lifetime of their bond. Experiments show that by increasing the applied force rate on a complex bond, the rupture force increases. This observation can be employed to understand the mechanism of protein interaction and extract parameters characterizing their complex bond. A standard theory, based on a thermal activation model, is widely used to analyze the AFM rupture force data because it yields parameters like bond length and dissociation rate fairly easily. The following discussion shows the details of this theory, and focuses on problems with the theory and suggested solutions.

4.1. Standard theory (Bell-Evans theory):

Survival probability[4, 5] is defined as the fractional portion of complex molecular bonds that hasn't yet dissociated. According to first order kinetics, the survival probability, *S(t)*, of a complex bond is represented as:

$$\frac{dS(t)}{dt} = -k_{off}(f)S(t) \tag{4.1}$$

where k_{off} is the dissociation or "off" rate, which depends on force *f*, and *t* is time. The off-rate depends on the height of the activation barrier, E_b, according to transition state theory, as follows

$$k_{off} = \tau_D^{-1} exp(-E_b(f)/k_B T) \tag{4.2}$$

Here, τ_D represents a diffusion time scale, T denotes the absolute temperature, E_b represents the activation barrier and f represents the applied force. The applied force modifies the height and shape of the activation barrier. Solving equation (4.1), an expression for the survival probability can be derived:

$$S(t) = exp\left(-\int_0^t k_{off}\,(f(t'))dt'\right) \tag{4.3}$$

A definite rupture probability in a finite time interval dt corresponds to a lowering of survival probability. This is expressed as:

$$P(t)dt = -dS = k_{off}(f(t))S(t)dt \tag{4.4}$$

As we want P as a function of the force, a change of variables can be performed:

$$P(t)dt = P(f)df \tag{4.5}$$

Combining equations (4.4) and (4.5), the probability distribution of rupture forces can be expressed as:

$$P(f) = \frac{k_{off}(f)}{\dot{f}} exp\left(-\int_0^f \frac{k_{off}(f\prime)}{\dot{f}\prime} df'\right) \tag{4.6}$$

The dissociation rate, K_{off}, is dependent on the activation barrier. The primary (simplifying) assumption is that the applied force reduces the height of the activation barrier, but does not change the position and shape of the barrier. Considering $x*$ to be the location of the transition state, an expression for k_{off} can be obtained as

$$k_{off}(f) = \tau_D^{-1} exp[-(E_b^0 - fx^*)/k_B T] = k_{off}^0 exp(fx^*/k_B T) \tag{4.7}$$

where $k_{\text{off}}{}^0$ is the off rate at zero applied force. With this, and assuming that the load rate df/dt $=\dot{f} = r_f$ = constant, the above equations can be solved in closed form to yield an expression:

$$P(f) = \frac{k_{off}^{0}}{r_f} exp\left(\frac{f}{f_c}\right) exp\left[\frac{k_{off}^{0} f_c}{r_f}\left(1 - exp\left(\frac{f}{f_c}\right)\right)\right] \tag{4.8}$$

where $f\,c = k_B T / x^*$ is a characteristic force for the complex bond at absolute temperature T.

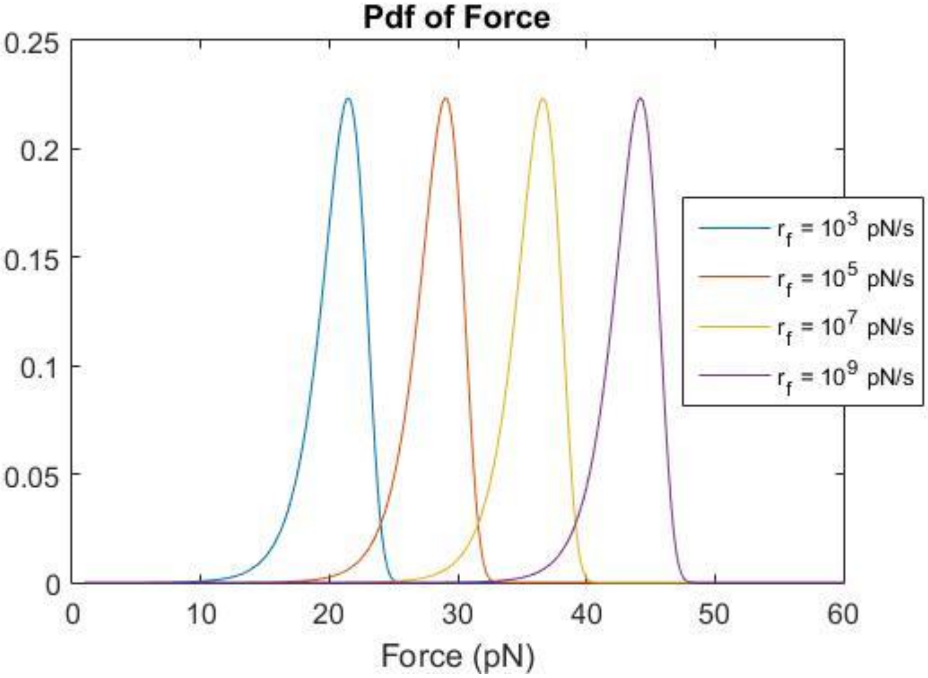

Figure 4.1. Theoritical simulation of probability distribution function (pdf) according to standard theory.

As shown in Figure 4.1, the resulting probability distributions of the force are skewed towards lower force values indicating the fact that increase in applied force leads to exponential decay of the bond lifetime. The maximum of this force distribution is given by

$$f_p = f_c \, ln\left(\frac{r_f}{k_{off}^{0} f_c}\right) \tag{4.9}$$

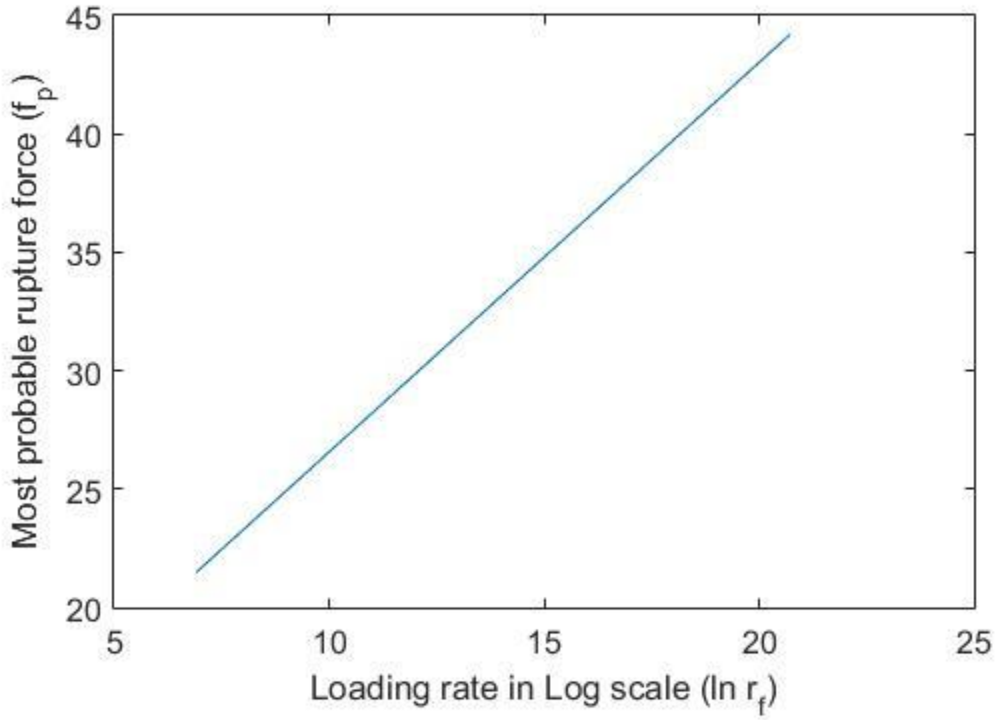

Figure 4.2. shows linear relationship between f_p (the most probable rupture force) and the logarithm of the load rate, r_f according to standard theory.

This leads to a linear relationship between f_p (the most probable rupture force) and the logarithm of the load rate r_f, as shown in Figure 4.2.

4.1.1. Limitations of this theory:

The standard theory has two major limitations:

1. Non-linearity of applied force: The basic theory assumes that the bond is loaded at a constant load rate, r_f. However, even if the piezo retracts the cantilever linearly, the protein and any linker molecule will behave like a polymer, and the force will change non-linearly. If we are not taking this into account, the fit of equation (4.9) for force

data (experimental) will produce too high a value of k_{off} (as much as one order of magnitude) and too low a value of x^*.

2. High force tail: The probability density function (Pdf) shown on Figure 4.1, produced by the standard theory, does not fit most experimental rupture force histograms. The experimental rupture force histograms often contain a broad tail toward higher forces, which is not seen in these theoretical curves. Assuming non-linear loading as discussed above does not solve this problem. Typically two possible explanations are put forward to explain the high force tail in the force histograms: Either there is a significant portion of *multiple attachments* (i.e. situations where more than one protein is attached to the tip and the two rupture at the same time, making it appear as a single rupture event), or there is significant heterogeneity in the bond conformation (for example by pulling at the bond through different angles), which is usually expressed by allowing for a range of values of x^*.

4.2. Bell-Evans-worm-like chain model (BE-WLC model):

We can model the nonlinear force by using the worm-like chain model (WLC Model). The contour length of the used linker can then be calculated from a fit of the force to this model. The force obtained from a WLC-force modified standard theory or Bell-Evans model can be extended in a power series to explore the effects of linkers on the measured forces. The WLC force is given by

$$f(x) = \left(\frac{k_B T}{l_p}\right)\left(\frac{1}{4}\left(1-\frac{x}{l_c}\right)^{-2} - \frac{1}{4} + \frac{x}{l_c}\right) \tag{4.10}$$

Where l_c is the contour length and l_p is the persistence length. The contour length refers to the length of the linker at the maximum extension, while the persistence length is associated with a characteristic length over which the polymer cannot be easily bent, i.e. it represents the stiffness of polymer linker. The cantilever system, tether, and complex bond can be visualized as a system of three springs in series. The force acting on the linker is the same as the force acting on the bond or cantilever. The loading rate can be expressed as

$$\dot{f} = \frac{df}{dt} = \frac{df}{dx}\frac{dx}{dt} = \frac{df}{dx}v \tag{4.11}$$

Where

$$\frac{df}{dx} = \frac{k_B T}{2 l_p l_c}\left[(1 - x/l_c)^{-3} + 2\right] \tag{4.12}$$

The apparent stiffness at the rupture point is given by

$$k_{app} = \frac{k_B T}{2 l_p l_c}\left[(1 - x_{max}/l_c)^{-3} + 2\right] \tag{4.13}$$

Equations (4.10) and (4.12) can be solved numerically to obtain the distribution of probable rupture forces. Alternatively, we can approximate the expressions. This can be accomplished by expanding the tether stiffness expression around x_0 as a Taylor series:

$$\frac{df}{dx} = \sum_{n=0}^{\infty} \frac{1}{n!}\left(\frac{d^n(df/dx)}{dx^n}\right)_{x_0}(x - x_0)^n \tag{4.14}$$

x_0 represents a tip location at which forces just begin to become visible. If the used linkers are short in length, the first two terms in the expansion dominate[46]. We find:

$$f(x) \approx k_t(x - x_0) + \alpha(x - x_0)^2 \tag{4.15}$$

$$\frac{df}{dx} \approx k_t + 2\alpha(x - x_0) \qquad (4.16)$$

According to the WLC model, α and k_t are expressed as follows:

$$\alpha = \frac{3k_BT}{4l_pl_c^2}\left[(1 - x_0/l_c)^{-4}\right] \qquad (4.17)$$

$$k_t = \frac{k_BT}{2l_pl_c}\left[(1 - x_0/l_c)^{-3} + 2\right] \qquad (4.18)$$

By the use of equations (4.11), (4.15), and (4.16), the probability distribution equation can then be expressed as

$$P(f) = \frac{k_{off}^0}{\nu\sqrt{k_t^2+4f\alpha}} exp\left(\frac{f}{f_c}\right). exp\left(-k_{off}^0 \int_0^f \frac{exp(f/f_c)}{\nu\sqrt{k_t^2+4f\alpha}} df'\right) \qquad (4.19)$$

Using $r_f = k_{app}v$ in (4.19), we generate a transcendental equation between most probable rupture force and loading rate:

$$\frac{2\alpha}{k_t^2+4f_p\alpha} - \frac{1}{f_c} + \frac{k_{app}k_{off}^0}{r_f\sqrt{k_t^2+4f_p\alpha}} exp\left(\frac{f_p}{f_c}\right) = 0 \qquad (4.20)$$

This relationship indicates the rupture force does not vary linearly with respect to the logarithm of the loading rate. There are two different sections of this relationship –

a) The dependence is highly non-linear at low loading rates.

b) The dependence appears to be almost linear with the logarithm of the loading rate at high loading rates.

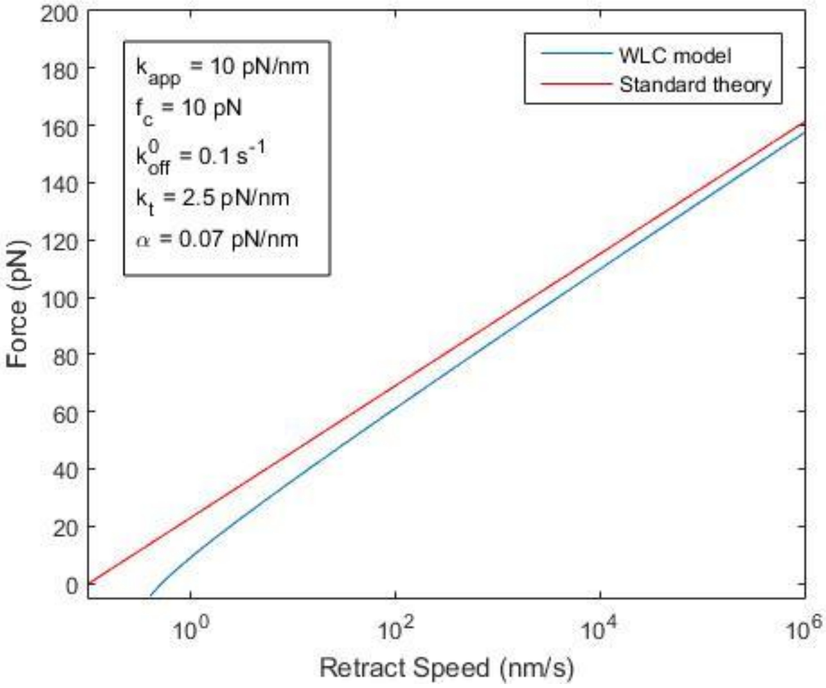

Figure 4.3. Theoretical simulation of rupture force (pN) vs retract speed (nm/s) according to standard theory and worm-like chain model

4.3. Raible's work to improve standard theory:

Evans and Ritchie's standard theory[4, 5] has been the basis to interpret and analyze experimental rupture data over many years. Raible et al.[9, 47, 48] calculated rupture force data from various experiments and demonstrated that they do not behave according to the assumptions of the standard theory. They suggested modifications to the standard theory which yielded results agreeing the experiments by taking heterogeneity of the chemical bonds into account.

4.3.1. Heterogeneity of chemical bonds:

The idea of the heterogeneity of the chemical bonds is has been advanced to explain the high force tail of the force distributions. To show the presence of bond heterogeneity, Raible et al.[9] observed that the expression *-vln(S(f))* should not depend on pulling velocities if the standard theory were to hold, where *S(f)* is the survival probability of the bonds, given by:

$$S(f) = exp\left(-\frac{1}{v}\int_{fmin}^{f}\frac{k_{off}(f')df\prime}{\frac{df\prime}{dx}}\right) \tag{4.21}$$

This can be rewritten in the following fashion:

$$S(f) = exp\left(-\frac{1}{v}\int_{xmin}^{x}\frac{k_{off}(f')\frac{df\prime}{dx}dx}{\frac{df\prime}{dx}}\right) \tag{4.22}$$

from which we find:

$$-v\ln S(f) = \int_{xmin}^{x}k_{off}(f'(x))dx \tag{4.23}$$

which is independent of the pulling velocity.

However, the force dependent dissociation rate k_{off} *(f)* is not necessarily a single-valued function of the force, but may be statistically distributed from measurement to measurement. These statistical variations of the off-rate can be due to: (a) Random fluctuations in the local molecular environment, which can be caused by water, solvent molecules and ions, pH and electric fields which can effect dissociation of the molecular assemblies; (b) Thermal activation, which may cause fluctuations of structures and can bring about various changes in molecular conformations; and (c) Fluctuations in orientation of the molecular assembly (relative to the direction of the pulling force directions), which may lead to different dependencies of dissociation rate k_{off} *(f)* on force (*f*). Different orientations of attached linker molecules may also lead to above variations. In addition to these reasons, there may be other sources of randomness which have been overlooked so far. The quantitative modeling of the influence of these statistical variations is not a trivial task.

In order to quantify the above ideas, we express the dissociation rate as $k(f) = k(f;\vec{\lambda})$ with a statistically distributed parameter set $\vec{\lambda}$ (which may include energy barriers, bond distances, bond angles etc.). These parameters have a random distribution with probability density of $\rho(\vec{\lambda};\vec{\mu})$, where $\vec{\mu}$ is a set of fitting parameters for the probability distribution (such as mean and standard deviation in case of a Gaussian distribution). The dependence of the dissociation rate on λ leads to a bond survival probability distribution up to applied force f, $p_v(f) = p_v(f;\vec{\lambda})$. This yields a new expression for $p_v(f)$ as follows:

$$p_v(f;\vec{\mu}) = exp\left\{-\frac{1}{v}\int_0^f \frac{k\left(f';\vec{\lambda}\right)}{F'\left(F^{-1}(f')\right)}df'\right\} \tag{4.24}$$

In order to compare experimentally determined survival probability distributions $S(f)$ to $p_v(f)$, we need to average over the probability distributions of the parameters.

$$\bar{p}_v(f;\vec{\mu}) = \frac{\int d\vec{\lambda}\rho(\vec{\lambda};\vec{\mu})p_v(f;\vec{\lambda})}{\int d\vec{\lambda}\rho(\vec{\lambda};\vec{\mu})p_v(f_{min};\vec{\lambda})} \tag{4.25}$$

The denominator in the above equation represents the fact that rupture forces under some f_{min} are indistinguishable from thermal fluctuations and normalizes the function for $f = f_{min}$. The experimentally determined survival probability, $S(t)$ is obtained from a set of measured rupture forces (f_1, f_2, …, f_N) by evaluating:

$$S(f) = \frac{1}{N}\sum_{n=1}^{N}\Theta(f_n - f) \tag{4.26}$$

where Θ is the Heaviside function. In order to fit the experimental survival probability to the fit function (4.22), a cost function was chosen as follows

$$Q(\vec{\mu}) := \sum_{n,v}[\mathrm{S}(f_n) - \bar{p}_v(f_n;\vec{\mu})]^2 \tag{4.27}$$

The above equation is summed over all experimental rupture forces f_n and pulling speeds v, and then numerically minimized with respect to the parameters $\vec{\mu}$.

In order to use this approach, assumptions about the functional form of $\rho(\vec{\lambda};\vec{\mu})$ and $k_{off}(f;\vec{\lambda})$ have to be made. Assuming the force-extension characteristic to be linear, the force can be expressed as:

$$F(s) = \kappa s \tag{4.28}$$

$k(f)$ can be expressed by equation (4.7), written in short-hand as

$$k(f) = k_0 e^{\alpha f} \tag{4.29}$$

$$\alpha = f_c^{-1} = \frac{x^*}{k_B T} \tag{4.30}$$

$p_v(f;\vec{\lambda})$ can be expressed as (writing equation (4.8) in sort-hand):

$$p_v(f;\vec{\lambda}) = exp\{-\frac{k_0}{v\kappa}\frac{e^{\alpha f}-1}{\alpha}\} \tag{4.31}$$

The heterogeneity of chemical bonds can be described by randomizing the two parameters k_0 and α, i.e. $\vec{\lambda} = (k_0, \alpha)$. Because of the exponential dependence on a, it is expected that any dependence on variations in α will outweigh the dependence on k_0. Therefore, Raible et al. assumed k_0 to be fixed and α to be the random parameter, i.e.

$$\vec{\lambda} = \alpha \tag{4.32}$$

The probability distribution of α is represented as a truncated Gaussian as follows

$$\rho(\alpha;\vec{\mu}) = \mathcal{N}\, exp\left\{-\frac{(\alpha-\alpha_m)^2}{2\sigma^2}\right\}\Theta(\alpha) \tag{4.33}$$

where $\vec{\mu} = (k_0, \alpha_{m\,,} \sigma)$. N represents the normalization constant. With this equation (4.32) is numerically fitted to the experimentally obtained survival probability using the cost function (4.28).

4.4. Akhremitchev's work to improve standard theory:

Most of the theoretical models that are employed to analyze experimental rupture force data assume dissociation of a single molecular bond during a given rupture event. The finite size of the AFM cantilever and nonzero grafting density make it plausible that multiple bonds may form at tip-sample contact. If the multiple tethers joining different bonds are approximately equal in length, these bonds might rupture simultaneously. The total measured rupture force in this case is distributed among various bonds.

Majority of the theoretical models assume the fact that the total rupture force is equally distributed among different bonds. However, force distribution among bonds is most likely to be unequal. Possible reasons for unequal distribution of forces are polydispersity of tethers, sample & tip roughness, and variation in the attachment positions of the tethers. The bond which experiences comparatively higher force is most probable to rupture first. When the first bond ruptures, a portion of the overall force transfers to the other bonds and can cause rupture of a second bond at the same time as the first rupture event[8, 49-52]. The peaks of the rupture force distributions due to these two bond ruptures might overlay with each other. An analytical model published recently describes the rupture of two separate bonds probed by tethers of different length simultaneously[8, 49]. This model helps us to derive kinetic parameters in the presence of multiple bond ruptures.

The two-bond rupture model explained below has been employed to analyze biotin-streptavidin interaction forces. This ligand-receptor system has a very high affinity and high specificity. There are two distinct energy barriers in their energy landscape (found by molecular dynamics simulation). One streptavidin molecule can form bonds with four biotin molecules and this multiple valency increase the probability to create multiple bonds. Sharp probes featuring 10–50 nm radius of curvature do not ensure the formation of a single bond at a time. In order to lower the number of simultaneous bonds, water-soluble polymeric tethers were used to attach biotin molecules to the AFM probes. By using comparatively longer tethers with 30 nm contour length, the specific and nonspecific ruptures can be recognized separately.

4.4.1. Two-bond rupture model:

If application of the same force leads to loading of two molecular bonds simultaneously, the total force is distributed between those two polymeric tethers. The two polymeric tethers are presumed to be loaded in parallel and their end-to-end distances and Kuhn lengths are also assumed to be equal. The first tether is loaded with force F1 and the second with a force F2 at the same time. The total survival probability of the two bonds is given by the survival probability of the first bond multiplied by the survival probability of the second bond, because we assume that breakage of either bond is an independent event. The total bond survival probability is given by:

$$S(F_\Sigma) = S_1(F_\Sigma)S_2(F_\Sigma) \tag{4.34}$$

Where the total force on the two bonds is:

$$F_\Sigma = F_1 + F_2 \tag{4.35}$$

From this we find for the total rupture probability:

$$P(F_\Sigma) = -\frac{dS(F_\Sigma)}{dF_\Sigma} = -\frac{d[S_1(F_\Sigma)S_2(F_\Sigma)]}{dF_\Sigma}$$

$$= S_1(F_\Sigma)\left[-\frac{dS_2(F_\Sigma)}{dF_\Sigma}\right] + S_2(F_\Sigma)\left[-\frac{dS_1(F_\Sigma)}{dF_\Sigma}\right]$$

$$P(F_\Sigma) = S_2(F_\Sigma)P_1(F_\Sigma) + S_1(F_\Sigma)P_2(F_\Sigma) \tag{4.36}$$

In case of parallel loading of two polymeric tethers, the force dependence of the survival probability of a first bond will be a little bit different from that of the second bond (due to variation in dynamics of loading). By ignoring these small differences, $S_1(F_\Sigma)$ can be written as $s(F_1)$ and $S_2(F_\Sigma)$ can be written as $s(F_2)$, i.e. we use the same functional dependencies of the survival probability for both bonds, and since they break independently, they only depend on the force applied to each bond. In that case, the previous equation can be expressed as

$$P(F_\Sigma) = s(F_2)\left[-\frac{ds_1(F_\Sigma)}{dF_\Sigma}\right] + s(F_1)\left[-\frac{ds_2(F_\Sigma)}{dF_\Sigma}\right]$$

$$= s(F_2)\left[-\frac{ds_1(F_\Sigma)}{dF_1}\frac{dF_1}{dF_\Sigma}\right] + s(F_1)\left[-\frac{ds_2(F_\Sigma)}{dF_2}\frac{dF_2}{dF_\Sigma}\right]$$

$$=s(F_2)\left[p(F_1)\frac{dF_1}{dF_\Sigma}\right] + s(F_1)\left[p(F_2)\frac{dF_2}{dF_\Sigma}\right] \tag{4.37}$$

The relative difference in the contour lengths for two polymeric tethers is not controlled in the experiments and is represented as

$$\delta L = \frac{L_2 - L_1}{L_1} \tag{4.38}$$

The probability distribution function for two bonds breaking needs to be averaged over all differences in contour lengths to account for variability during the measurements, i.e. it is represented as

$$\Pi(F_\Sigma) = \frac{\int_0^{\delta L_{max}} p_t(\delta L) P(F_\Sigma,\delta L) d\delta L}{\int_0^{\delta L_{max}} p_t(\delta L) d\delta L} = \frac{\int_0^{\delta L_{max}} P(F_\Sigma,\delta L) d\delta L}{\delta L_{max}} \tag{4.39}$$

Where $p_t(\delta L)$ refers to the probability to achieve a particular value of difference in contour length of the tethers and $\Pi(F_\Sigma)$ represents the mean probability density in case of rupture of two bonds. δL_{max} stands for the relative difference in contour lengths below which two individual rupture events cannot be experimentally distinguished. By applying some linearization, assuming $p_t(\delta L)$ to be a constant, and substituting equation 4.38, we can arrive at an approximate expression for mean probability density for rupture of two bonds.

$$\Pi(F_\Sigma) \approx (1 + 2\delta L_c^{max}) s\left(\frac{F_\Sigma}{2}\right) \frac{[s(F_2) - s(F_1)]}{F_1 - F_2} \tag{4.40}$$

Here, *s(F)* is the survival probability for one bond and it is expressed as a function of force. F_Σ represents the overall force distributed over two bonds. The force on each bond is assumed to act in the same direction. In case that the lengths of the two tethers are the same the probability density function in equation 4.37 will be

$$P(F_\Sigma) = \frac{s(F_\Sigma)}{2} \frac{p(F_\Sigma)}{2} \tag{4.41}$$

This implies that in case of independent loading of two bonds with the same force, the probability distribution will peak at a force smaller than two times f_p (the most probable rupture force for one bond) due to the presence of the factor $\frac{s(F_\Sigma)}{2}$.

The measured rupture forces in most experiments can be caused by single-bond as well as two-bond and multiple-bond ruptures[47, 48]. Usually, a low grafting density[1, 7] of molecules is used, and therefore only single- and two-bond ruptures are considered here. The total probability distribution (PD) of rupture forces can be fit by combining one- and two-bond rupture probability[53-56] distributions as follows:

$$P_{total} = A_1 p_1(F) + (1 - A_1)\Pi(F) \tag{4.42}$$

A_1 is the fraction of single-bond rupture events and $p_1(F)$ is the probability distribution (PD) of the single-bond ruptures. $\Pi(F)$ represents the PD of the two-bond ruptures. If we substitute the value of $\Pi(F)$ from equation 4.40 and value of $p_1(F)$ from the standard theory, we can get an equation to express the total probability distribution in terms of total rupture force. The approximated value of $\Pi(F)$ from equation 4.40 will lead to a probability distribution function that is overestimated towards the higher forces as this model assumes that the tethers are aligned normal to the surface. In reality, any tilting of the tethers will cause lowering of forces along them. We will be able to see the first peak due to single bond rupture (Bell- Evan's theory) towards the lower forces and another smaller peak towards the higher forces (according to the contribution from the two bond ruptures in the last equation), possibly explaining the presence of the high force tails in experimental measurements. The rupture force for two bond ruptures is greater than rupture force for single bond rupture but less than the summation of rupture forces of two individual bonds.

4.5. Conclusions and Summary

In this chapter, we described the "standard" theory for calculating rupture force distributions, dependence of most-likely rupture forces on pulling rates, and ways to extract kinetic parameters from rupture force measurements. We also discussed the shortcomings of the standard theory which prevent the precise measurement of kinetic parameters like bond lengths and activation energies. We discussed how the constant loading rate assumption of the standard theory is not correct and how nonlinear force were addressed by BE-WLC model. We could prove that if we take nonlinear stiffness of the linkers into account, the relationship between the most probable rupture force and logarithm of the loading rate were not linear.

Following work by Raible et al.[9], we also discussed the influence of bond heterogeneity, which was parametrized by introducing randomness of bond length in the survival probability equation. From our discussion of Akhremitchev's work, we found that the simultaneous rupture of multiple bonds during experiments can lead to a high force tail in the rupture force distributions, even if obvious multiple ruptures are excluded from the analysis. In Chapter 5, we will further explore the influence of bond heterogeneity and multiple attachments on single-molecule measurements through experiments on a model system and Monte Carlo simulations.

CHAPTER 5: FORCE MEASUREMENTS USING AVIDIN-BIOTIN MODEL SYSTEM

We use atomic force microscopy (AFM) to measure dissociation in protein systems and protein-protein interaction forces at single molecular level. As discussed in Chapter 4, the Bell-Evans Standard Theory[4, 5], used for analyzing rupture force data (contingent on the concept of thermal activation and the deformation of the activation barrier) yields a rupture force distribution function which is skewed to the left (towards low force). However, most of the experimental measurements of rupture force data generate a probability distribution function (pdf) with a high force tail. The probable cause of this high force tail in the rupture force pdf is either multiple attachments (though recognizable multiple ruptures are typically removed from rupture force analysis) or heterogeneous bonding. To study the effect of multiple attachments, we created a varying density of active sites using self-assembled monolayer by incubating the substrate in mixed solutions of active (biotin) and inactive (methyl-terminated) PEG molecules and pursued imaging and force measurements with avidin functionalized AFM tip. Here, we present a combined approach to answer the question of how much of the high force tail can be attributed to either cause. We found that the presence of multiple attachments, while significant, accounts for only a fraction of the events in the high force tail of the distribution.

5.1. Materials and methods:

5.1.1. Sample preparation: In order to distinguish between specific and non-specific interactions, molecules of interest are covalently attached to the free ends of flexible polymeric tethers[3, 57], such as polyethylene glycol (PEG), which are bound to the chemically functionalized AFM tip and substrate. The use of linkers allows us to distinguish between specific and non-specific interactions using the resulting offset of the rupture point from the contact point as a discriminating measure. Furthermore, flexible linkers allow the attached molecules to access various orientations, which increase the binding probability[58]. Probable causes of discrepancy between analysis of experimental rupture force data and theoretical expectations are the effects of the non-linear stiffness of polymeric tethers (used for attaching the molecules to cantilever tip and substrate), the violation of the constant loading rate assumption, and non-linearity of the applied force. The density of the molecules attached to AFM tip or the substrate can be changed by varying the number of active PEG linkers attached to the surface. Polyethylene glycol (PEG), one of the most widely used cross-linker is accessible with various active terminal groups: In this study, we used silane PEGs to attach directly to the oxidized silicon tip and silicon substrate. Avidin -biotin interactions were chosen to serve as a model system for our measurements. Silane-polyethylene-glycol-biotin (Silane-PEG-Biotin) with average molecular mass of 2000 Da and silane PEG,methoxy-polyethylene-glycol (Silane PEG, mPEG) with averaged molecular mass of 2000 Da were purchased from Nanocs Inc (New York, USA).

Salt-free avidin with a combined molecular mass of 67 KDa was bought from Thermo Scientific, Pierce Biotechnology (Rockford, Illinois, USA). MLCT-Bio probes (rectangular silicon nitride probes with a silicon tip) were purchased from Bruker Corporation. We used MLCT-A with nominal spring constant of 0.06 N/m. Silicon squares (15*15 mm^2) were used as substrates. For cleaning, they were rinsed with 70% Ethanol followed by ultra-deionized water (18.2 MV_cm) for 10 minutes and air dried. The silicon pieces kept inside a clean Petri dish sealed with parafilm to protect them from moisture and air contamination until they were functionalized.

5.1.2. Protocol of decorating the AFM tip and the substrate with PEG linkes:

The number of active sites on the silicon substrates was adjusted by incubating the substrates in a mixed solution of biotin-terminated PEG molecules and mPEG. The mPEG does not bind to avidin, which permits us to regulate the density of active sites. In order to control the ratio of the biotin-PEG molecules in the mixture, we prepared two separate solutions (both solutions were prepared with same 1000 μM molality) of the biotin PEG molecules and mPEG molecules. The solutions were mixed later to produce six different 5 ml solutions with ratios of the biotin PEG molecules at 2%, 4%, 20%, 30%, 50% and 100%. We used cleaned silicon pieces as substrates and attached the square silicon pieces at the bottom of a clean 50 mm Petri dish. To functionalize the substrates with these mixed PEG solutions, we cleaned each of the six coated silicon pieces with hexane, ethanol and ultra-DI water to remove hydrophobic and hydrophilic contaminants. This step was followed by gently blow-drying the samples with high-purity nitrogen. The substrates were then immersed in the mixed PEG solutions and put on the shaker for 15 minutes of incubation inside the biohood. After incubation, the substrates were again rinsed with ultra DI water. They were transferred to clean containers, covered with room temperature phosphate buffer saline (PBS with PH 7.2). The substrates were then stored in filtered PBS at 4 °C until we performed experiments.

The cantilevers were first functionalized with silane PEG NHS (with averaged molecular mass of 3400 Da) using the exact method described above and incubation time in this case was 2 hours. The cantilever was then stored in filtered PBS at 4 °C overnight. The cantilever was taken out of buffer the next day and kept outside for 1 hour so that the temperature of the solution reaches room temperature and the following procedures were executed in order to functionalize the cantilever tip with avidin:

Reaction with protein: The cantilever was then incubated with 0.05 M and 5 ml solution of avidin for one hour. After that, it was washed for one time with PBS buffer.

Finally the cantilever was again transferred to a clean container filled with 5 ml of PBS buffer and preserved in refrigerator at 4 °C until experiment.

5.2. Force measurement procedure:

Single molecule force spectroscopy measurements were executed using a Bruker Bioscope Catalyst (Billerica, MA, USA) AFM. The cantilever spring constants were determined with the help of built-in thermal tuning method. At first, control experiments were performed with either the tip or the substrate or with both un-functionalized. All the experiments were performed in pH 7.2 PBS at room temperature. An Aqua-Hold pap pen from Thermo Fisher Scientific (Waltham, MA, USA) was used to draw a circle around the buffer drop on the sample to prevent buffer leakage into the objective lens area. The probe was scanned over a 5 x 5 μm^2 square area on the substrate using Peak Force QNM mode to obtain good topographical images and at least 1000 force curves were collected for each biotin sample. We performed more than 7000 force curves overall using functionalized tips and substrates with the tip velocity ranging from 10 to 10000nm/s. The force interactions were measured at different locations of the sample surface. The same cantilever tip was used repeatedly for many hundreds of measurements without noticeable degradation of the lever. The calibrated spring constant using thermal tuning method (mentioned in detail in Chapter 2) was 0.0693 N/m.

5.3. Measurement procedure and data analysis:

The functionalized cantilever tip was manually approached close to the substrate so that the avidin and biotin can bind. The probe was then retracted to measure the minimum force needed to break the bond (rupture or unbinding force). Figure 5.1 represents an example of a deflection error (nm) vs Z(nm) curve to portray the changes in the force acting on the cantilever tip with the changes in the piezo extension.

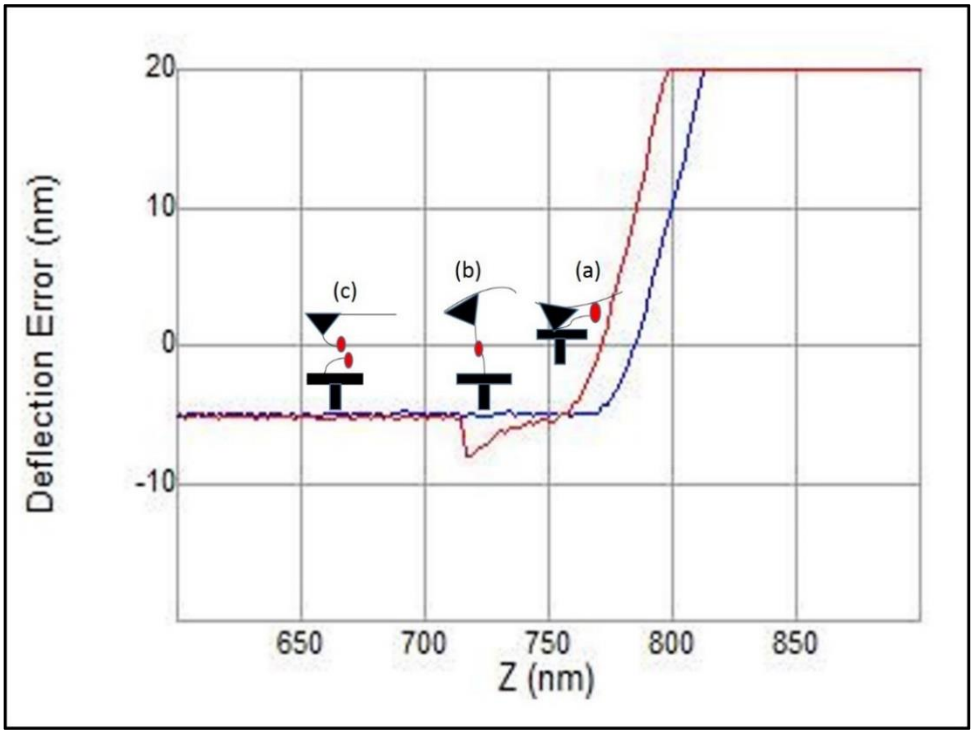

Figure 5.1. Experimental force curves: Blue is approach and red is retract. (a) Cantilever is in contact with surface, bond forms, (b) Bond experiences maximum stretch, (c) Bond breaks.

Fig 5.2 represents different situations occurring in protein-protein interaction force measurements during experiments. This figure represents various scenarios including interaction of single protein molecules, nonspecific interaction of either of relevant protein molecules with the substrate or with just the PEG linker molecules, and multiple attachment events involving more than protein molecules[6]. Case A represents the ideal interaction of two protein molecules (one attached to the tip and another attached to the substrate) where maximum stretching of the linker molecule is twice the contour length. In this case, the force acting on the cantilever is same as force acting on the bond. B represents the attachment of a protein molecule to the substrate and C represents the attachment of protein molecule to a linker molecule. D and E represent multiple attachment interactions (involving multiple protein molecules). In case B (non-specific interactions), the measured linker length will be only equivalent to a single linker length (compared to two linker lengths in the case of the specific interaction in A), allowing for disnguishing specific from non-specific interactions.

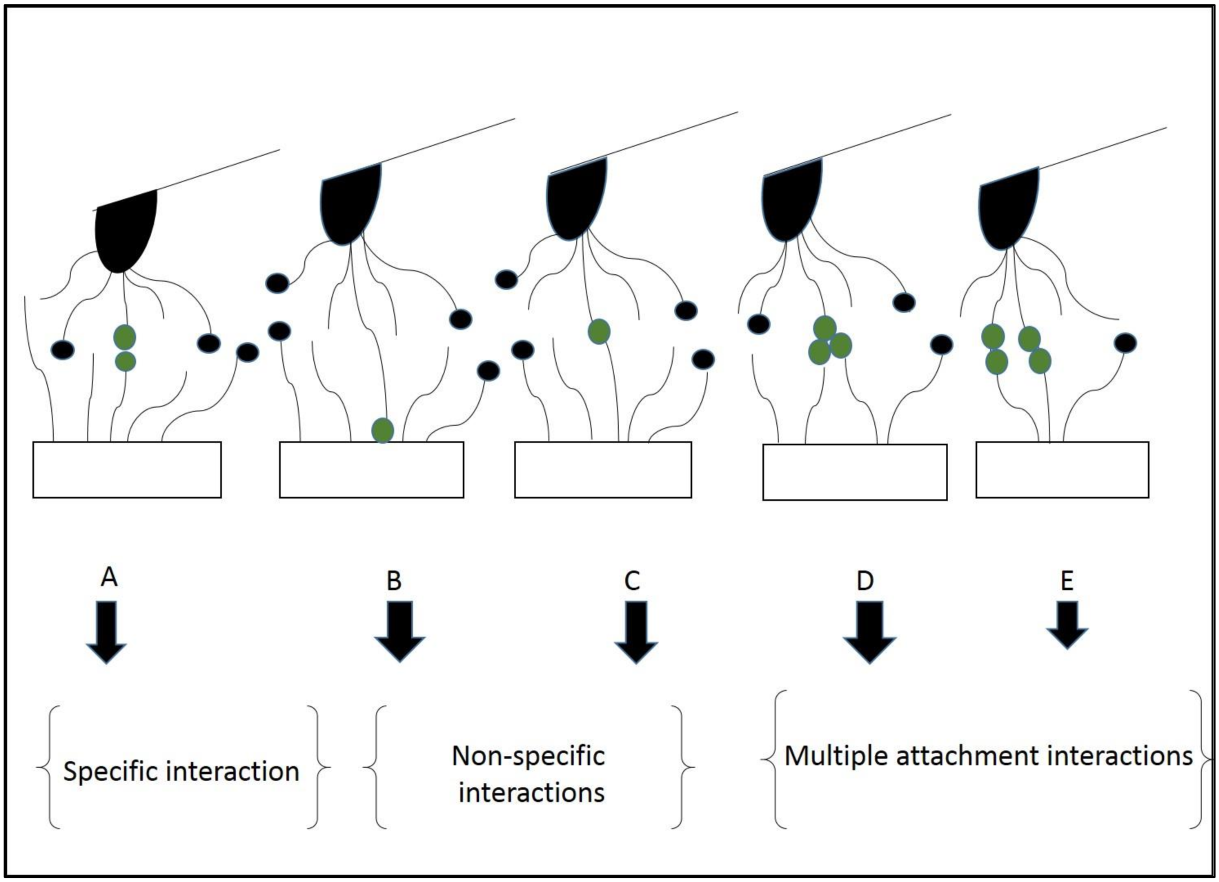

Figure 5.2. Different arrangements of molecular interactions

Several attempts have been made to go beyond the constant loading rate assumption and incorporate non-linear loading of the polymeric tethers into Bell-Evans Standard Theory. Ray, Brown and Akhremitchev presented a model that yields an expression of the systematic errors introduced by non-linear loading (considering the freely-jointed chain model for the polymeric tether)[8, 49]. This analytical model demonstrates underestimation of the derived width of the activation barrier and overestimation of the dissociation rate constant if experimental rupture force data is analyzed according to Bell-Evans standard theory without considering the elasticity of the polymeric tethers.

Even with taking the non-linear linker stiffness into account, the overall shape of the rupture force histogram is expected to change little. In general, theory predicts that rupture force histograms skew towards low force with a sharp cutoff at higher forces. This is because the probability of a rupture increases exponentially with the applied force. However, most of the measured rupture force distribution instead exhibit a pronounced tail to the right, i.e. towards higher forces. This cannot be explained by the standard or modified standard models.

Raible et al.[9] (discussed at length in Chapter 4) applied the loading rate equation (5.1) to the survival probability of bond equation (4.3)

$$\frac{df}{dt} = v\frac{df}{dx} \tag{5.1}$$

It led to the following equation for the survival probability of the specific bond:

$$S(f) = exp(-\frac{1}{v}\int_{fmin}^{f}\frac{k_{off}(f')df\prime}{\frac{df\prime}{dx}}) \tag{5.2}$$

According to equation (5.2), $-v\, ln(S(f\,))$ should not depend on pulling velocity and all the relevant data should fall into a single master curve at different retract speeds.

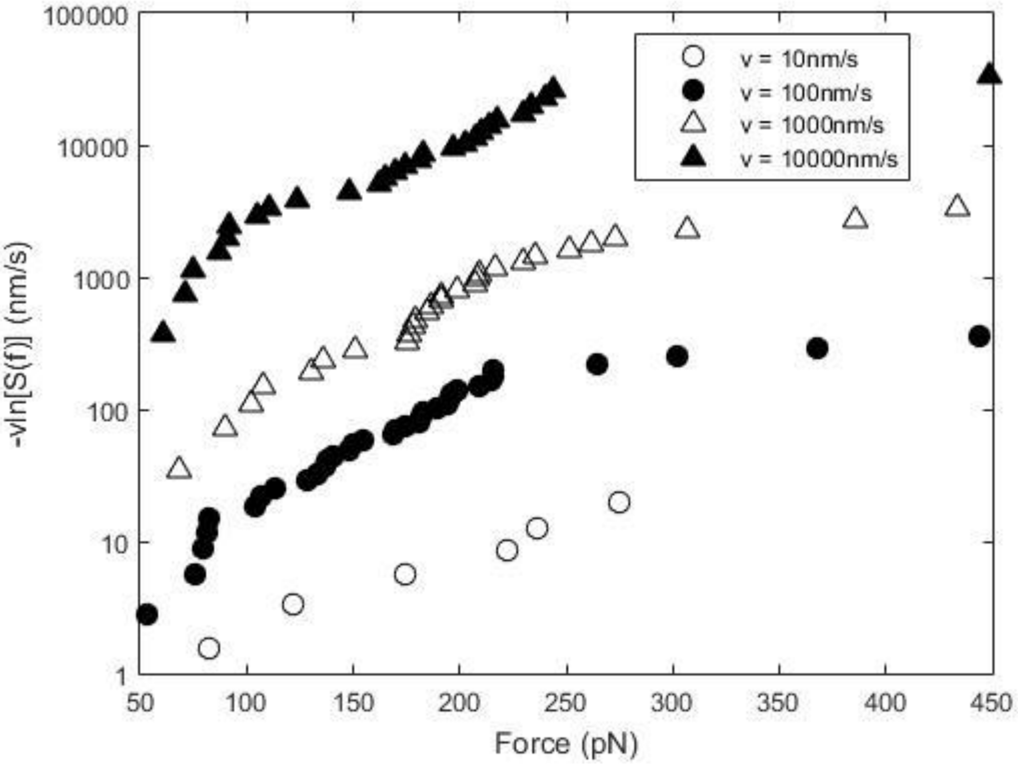

Figure 5.3. –vln(S(f)) (in $\log_{10}$ scale) vs rupture force (pN) plot for different pulling velocities (ranging from 10 nm/s to 10000 nm/s)

Our experimental plot (Fig 5.3) clearly shows that *–vln(S(f))* is dependent on pulling velocity and does not collapse on one master curve. This conflict between theory and experiment can be resolved if a parameter is added in equation (5.2). That parameter has to represent the randomness of the bond length.

There are model (discussed in Chapter 4) that can explain the existence of the high rupture force tail due to either heterogeneous bonding or multiple attachments. If we can control multiple attachments, but still notice high force tail region, then its existence can likely be attributed to heterogeneous bonding. To control multiple bonding, we modified the surface density of active sites, as described above. Note that we cannot functionalize the cantilever with only a single molecule.

5.4. Measurements on substrates with varying densities of active sites

Surface density of active PEG molecules (biotin PEG) is approximately equal to the linker surface density multiplied by the fraction of biotin-PEG in the biotin-PEG/mPEG mixture used to functionalize the substrate. We measured binding probabilities and multiple attachment probabilities with avidin functionalized cantilever tip to validate our method of varying surface density of active PEG molecule and to understand how binding and multiple attachment probabilities[8] are affected by increasing biotin ratios.

The binding probability is defined as follows:

$$\text{Binding probability} = \frac{\text{Number of force curves that show at least single rupture event}}{\text{Total number of force curves performed on the substrate}}$$

In order to validate measured binding probabilities statistically, we collected 1000 forces curves for each of the biotin ratios and force measurements for all of those ratios were performed with the same tip velocity of 2 μm/s.

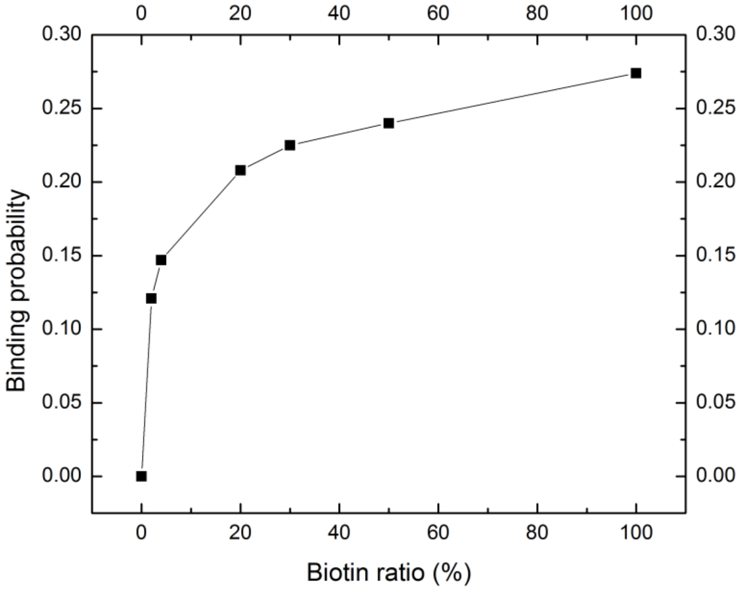

Figure 5.4: Binding probability vs Biotin ratio plot

Figure 5.4 represents the nature of binding probability with increasing biotin ratio. It demonstrates that the probability increases rapidly for low biotin ratio regimes and saturates at high biotin ratio (similar to Langmuir isotherm). This validates our method of controlling surface density. We used the same scanning speed and same avidin functionalized cantilever (MLCT-A with nominal stiffness of 0.07N/m) throughout the experiment for all the biotin samples. We also performed a large number of force curves on different regions of the sample to prevent the binding probabilities getting affected by different retract speeds or various distributions of avidin molecules on the cantilever tip.

5.4.1. Multiple attachment probability:

The fraction of multiple attachments is defined as:

Multiple attachment probability =

$$\frac{\text{Number of Force curves that demonstrates at least two binding events}}{\text{Number of force curves that demostrates at least one event}}$$

For 100% biotin ratio, the interaction forces between biotin and avidin display 35.7% multiple attachments. Multiple attachment probability (Fig. 5.5.) increases with increasing biotin ratios following a similar behavior as the binding probability (Fig 5.4). We used multiattachment probability in order to calculate the probability of multiple rupture events happening at the same

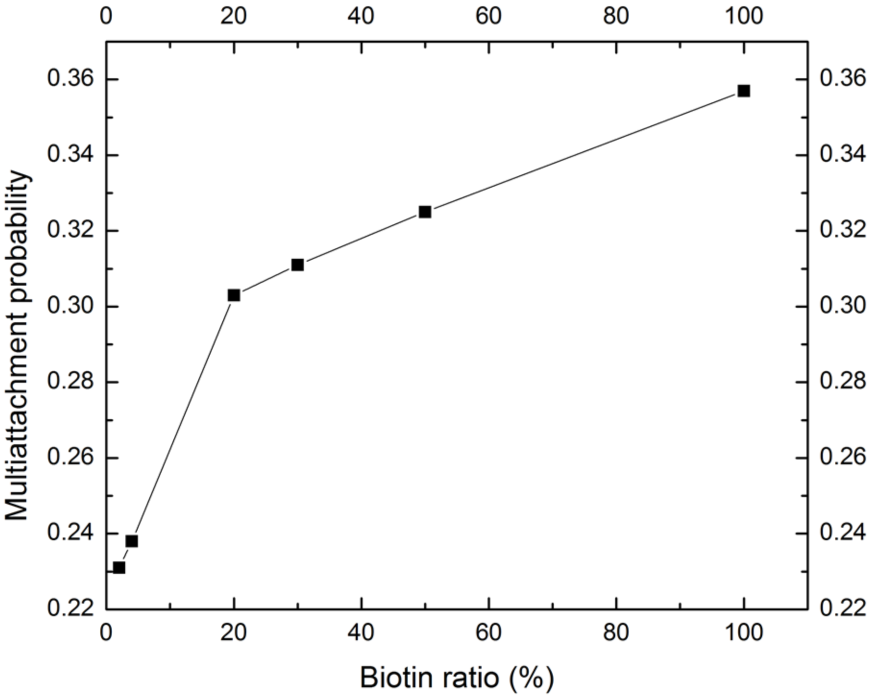

Figure 5.5: Multiattachment probability vs biotin ratio (%)

time or at the same piezo extension. The probability to observe multiple attachments should be greater than probability to observe single attachment and we observed that in experimental results too.

Using the molecular weight and bond structure, we found that the contour length of used PEG molecules is approximately 20-25 nm. For all the detected single rupture forces at all biotin ratios, we plotted contour length histograms in order to figure out if our single rupture force measurements are specific or there is a range of forces for which the contour lengths are below the theoretically measured contour length values. We did not notice any contour length reading below that value in our measurements. So, we are considering all the single rupture forces corresponding to those contour lengths. An example of a contour length histogram (for 50% biotin) is shown in the following figure.

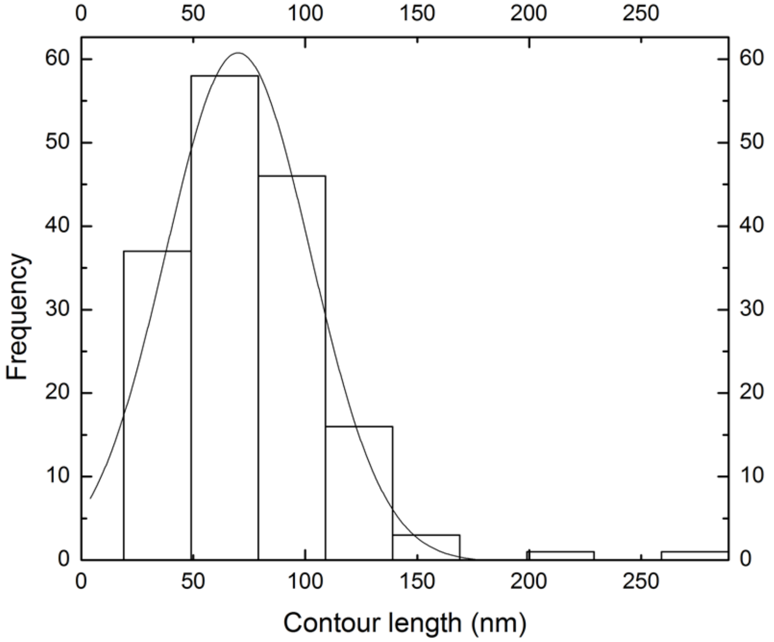

Figure 5.6: Contour length histogram for 50 % Biotin data

We plotted probability distribution functions (pdf) of the rupture force (for all the measured single rupture forces for all the biotin ratios) corresponding to all the contour lengths. From the peak of the Gaussian fit of the rupture force histogram, the most probable rupture force was measured. An example of pdf of the rupture forces for 50% biotin data is shown below (Fig 5.7) where the most probable unbinding or rupture force is 107.7 pN. We noticed the fact that our experimental rupture force histograms contained a large shoulder and tail contrary to the standard theory. We used the number of events which are located to the right of peak beyond the mean plus one standard deviation in order to calculate the tail percentage (described in this chapter later) for each biotin ratio.

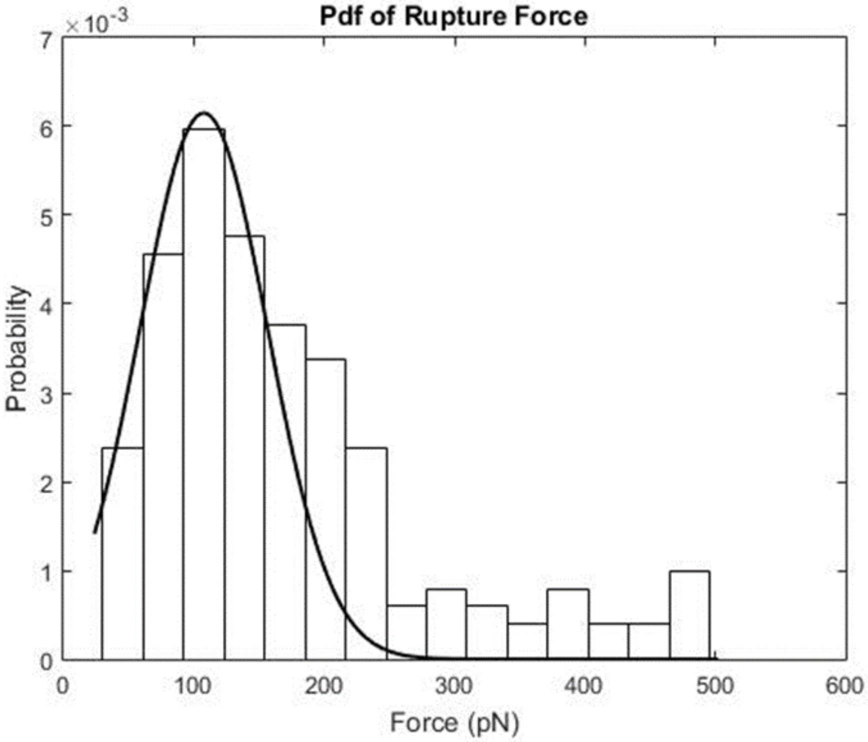

Figure 5.7: Pdf of rupture force for 50% biotin data where peak of the Gaussian fit signifies the probable rupture force (107.7pN in this case).

In the case of multiple binding, we may see several well-separated rupture events. Such measurements are excluded from the analysis. However, multiple bond ruptures can occur at the same piezo-extension of the cantilever, and therefore appear as a single rupture event. We call these hidden multiple rupture events “zero-distance ruptures”. Typically, more than two attachments are unlikely and we only need to consider double ruptures. For double rupture events, the zero-distance multiple attachment probability can be calculated by measuring the spatial separation between multiple rupture events occurring in the same force curve, plotting a histogram of these separations, and extrapolating it to zero distance. For this histogram, we only considered measurements with two visible rupture events and discarded the rare occasions when we measured more than two. This distribution of rupture distances, $P_2 (\Delta R)$, is expected to peak at zero, because the PEG tethers are roughly of similar length. The rupture location fits a Gaussian distribution, and it is shown below that the expected distance between multiple events would be a modified Gaussian as well. The distribution of rupture locations is given by:

$$D\,(R) = \frac{A}{(2\pi\sigma^2)^{1/2}}\, exp\left\{-\frac{(R - \overline{R})^2}{2\sigma^2}\right\} \tag{5.3}$$

Here, A is normalization constant, R is the rupture location, $\overline{R}$ is the average and σ is the standard deviation of R distribution. The probability for a rupture event to occur at the location range $R \pm dR/2$ *is* $dP(R) = D\,(R)\,dR$. This can be used to obtain the distribution of the location difference (ΔR) between two successive events. Statistically, the rupture events occurring at different locations are considered as independent[6] events, so the probability to observe them simultaneously is given by

$$dP\,(R,\acute{R}\,)=D\,(\acute{R})dR\;D(\acute{R})d\,\acute{R} \tag{5.4}$$

By substituting $R' = (R + \Delta R)$ into $dP(R, R')$ and integrating it over R, we obtain the probability distribution function of ΔR:

$$dP\,(\Delta R)= D\,(\Delta R)d\Delta R= \int_0^\infty D\,(R)\; D(\,R+\Delta R\,)dR \tag{5.5}$$

We substituted the value for $D\,(R)$ in this equation:

$$D\,(\Delta R)d\,\Delta R =\frac{A^2}{2\pi\sigma^2}\int_0^\infty exp\,\{-\,\frac{(R\text{-}\overline{R})^2}{2\sigma^2}\}\;exp\;\{-\frac{(R+\Delta R\text{ - }\overline{R})^2}{2\sigma^2}\}\,dR \tag{5.6}$$

$$= \quad \frac{A^2}{2\pi\sigma^2}\;exp\,(\text{-}\frac{(\Delta R)^2}{2\sigma^2}\;)\int_0^\infty exp\,\{-\,\frac{2(R\text{-}\overline{R})^2}{2\sigma^2}\}\;exp\;\{-\frac{2\,\Delta R\,(R-\overline{R})^2}{2\sigma^2}\}dR$$

$$= \frac{A^2}{2\pi\sigma^2}\;exp\,(\text{-}\,\frac{(\Delta R)^2}{2\sigma^2}\;)exp\,(\frac{(\Delta R)^2}{4\sigma^2})\int_0^\infty exp\,\{\,-\,\frac{2(R\text{-}\,\overline{R})^2}{2\sigma^2}\}\;exp\;\{-\frac{2\,\Delta R\,(R-\overline{R})}{2\sigma^2}\}\,dR$$

$$= \quad \frac{A^2}{4\pi\sigma^2}\,.\;\sigma\sqrt{\pi}\;exp\,(\text{-}\frac{(\Delta R)^2}{4\sigma^2})$$

$$= \frac{A^2}{4\sigma\sqrt{\pi}}\,.\;\;exp\,(\text{-}\frac{(\Delta R)^2}{4\sigma^2}) \tag{5.7}$$

So, rupture location distribution function $D\,(\Delta R)$ is a Gaussian with standard deviation $\sqrt{2}\sigma$ and it has a peak at the origin. An example of the experimental pdf of ΔR for 50% biotin data is represented below:

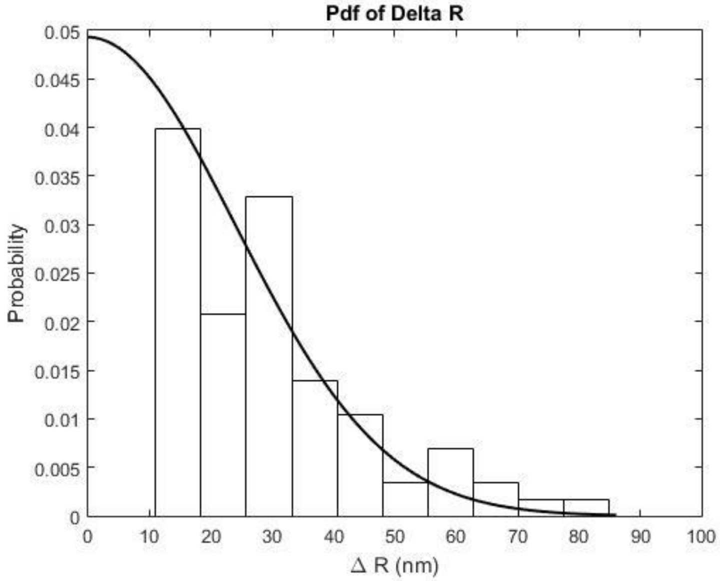

Figure 5.8: Pdf of ΔR for 50% biotin data

In our experimental data, we could not identify double rupture events which are less than 9 nm apart. So, we integrated the Gaussian fitted ΔR histogram from 0 to 9 nm in order to calculate the fraction of double binding events that are not distinguishable from single-binding events. This fraction of "invisible" double events is denoted by p_{mi}. For the 50% biotin data shown in Figure 5.8, we found $p_{\mathrm{mi}} = 0.295$. We categorized the experimental rupture events as follows:

a) Apparent single rupture events (multiple rupture events happening at a distance of less than 9 nm) with probability p_{mi}

b) Easily distinguishable multiple rupture events with probability p_{md}

c) True single rupture events with probability p_1

By using probability calculations, we calculated the zero-distance multiattachment probability using the following equation:

$$\text{Zero-distance multi-attachment probability} = \frac{p_{mi}p_{md}}{(1-p_{mi})(1-p_{md})} \tag{5.8}$$

According to the above equation, zero-distance multi-attachment probability for 50% biotin is = $(0.325 \times 0.295)/(1-0.295)(1-0.325)$ = 0.201. In order to verify whether shoulder and tail region to the right of rupture force histograms can be attributed to simultaneous multiple attachments, we plotted a graph of zero-distance multiple-attachment probability and tail percentage vs biotin ratio (%).The open circles in Figure 5.9 represent the the zero-distance multi-attachment probability and solid circles represent the tail percentage as a function of varying biotin density. From this figure, we can clearly conclude that zero distance multiple attachment probability and tail percentage both increase with increasing biotin ratio, however there is a considerable gap between them. So, high force shoulder and tail cannot be completely attributed to multiple attachments. The heterogeneous binding seems to play a more important role than multiple attachments in causing the high force region in the rupture force histograms.

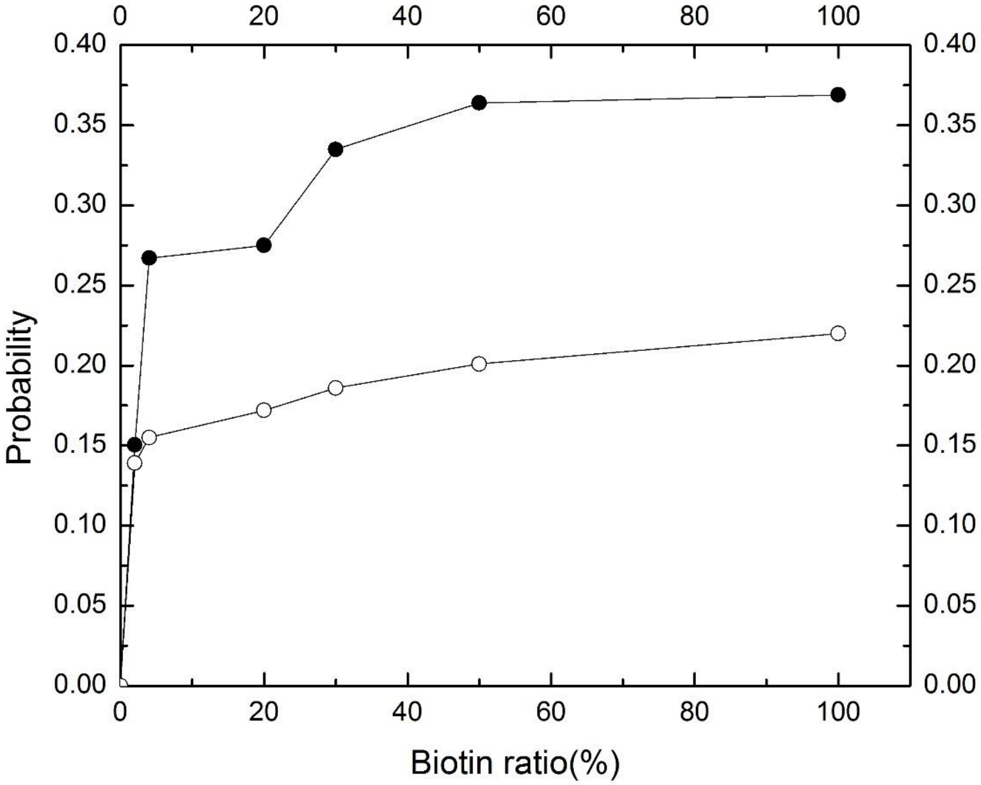

Figure 5.9. Zero-distance multiple attachment probability and tail percentage vs biotin ratio (%): open circles indicate zero distance multiple attachment probability and closed circles represent tail percentage

We also performed Monte Carlo simulations of various scenarios, using a 1D Markov-chain algorithm to match experimental results with theoretical expectations. In case of Markov system, the current state of the system is determined just from the previous state of the system through transition probabilities. If a bound state (state 1) and dissociated state (state 2) are the possible states of two molecules, the current probability with which the system can be found in state 1 can be represented by P_1 and the probability with which the system can be found in state 2 can be represented as P_2. The transition probabilities between these states include, for example,

p_{11} (the probability that the system stays in state 1) and p_{21} (the probability that the system switches from state 2 to 1). For such a two-state system, the transition is given by

$$(P_1' \quad P_2') = (P_1 \quad P_2)\begin{pmatrix} p_{11} & p_{12} \\ p_{21} & p_{22} \end{pmatrix} \tag{5.9}$$

For single bond formation, the system can be initially prepared in the bound state, represented by $(P_1\ P_2) = (1\ 0)$ and the corresponding transition matrix is given by:

$$M = \begin{pmatrix} 1 - k_{off}dt & k_{off}dt \\ 0 & 1 \end{pmatrix} \tag{5.10}$$

The transition probability in a definite interval of time *dt* can be represented by the product of the transition rate and the interval of time. We set p_{21} at 0 and p_{22} at 1 to make sure that there is no chance for a bond to bind again after its breakage. k_{off} in the last equation can be represented (according to standard theory) as

$$k_{off}(f) = k_{off}^0 exp(fx^*/k_BT) = k_{off}^0 exp(f/f^*) \tag{5.11}$$

f^* is called the characteristic force and x^* is the spatial separation between the equilibrium and the transition state.

During the simulation, first the probability of the system being in the state 1 and state 2 is determined through applying equation (5.9) with the transition matrix (5.10). Using the determined probabilities, simulations are performed using a Monte Carlo algorithm to determine the current state of the system. This is done by usage of a uniform random number *r* over [0, 1]. If this random parameter *r* is less than P_1, the system stays in state 1 and if this parameter is greater than P_1, the system switches to state 2. If the later situation happens, the current force is considered as the rupture force. If the bon d does not break (system stays in state 1), the force is incremented according to a chosen force rate and the same simulation experiment is repeated until the bond breaks. This is repeated N times for generating rupture force histograms.

To simulate double bond ruptures, we can define a multiple attachment probability as p_m. The bond rupture is in the simulation considered as double bond rupture if a random number r is less than p_m. To represent the force on both linkers, a force vector is defined as $f = (f_1, f_2)$. We also defined individual transition matrix for each of the bonds depending on the current force acting on each bond. If both bonds break, the simulation experiment repeats itself. In general, once one bond breaks, the second breaks shortly after. Considering small ΔL values, most double bond ruptures can be assumed to happen almost simultaneously and would appear as an apparent single rupture in experiments.

When we use polymeric tethers in our experiment, the nonlinear force can be expressed using freely-jointed chain or BE-WLC model. Here we used a simplification by using approximation of linear force. This does not seem to change the shape of the probability distribution of the force. If the two linkers have ΔL as length difference, the total force on them can be expressed as:

$$k_L(d - x) = k_p x + k_p(x - \Delta L) \tag{5.12}$$

where d is tip sample distance, x represents extension of the linker, $(d – x)$ represents the deflection of the cantilever, k_L represents the stiffness of the cantilever and k_p represents the polymeric tethers' effective stiffness . From the last equation x can be solved as

$$x = \frac{k_p \Delta L + k_L d}{2k_p + k_L} \tag{5.13}$$

The individual force on the first and second linkers can be written as $f_1 = k_p x$ and $f_2 = k_p(x - \Delta L)$. Upon the rupture of any of them, the force will redistribute itself over the other linker. In case that the bond on linker 2 ruptures first, the force applied to first linker can be expressed as:

$$f_1 = k_p \frac{k_L d}{k_L + k_p} \tag{5.14}$$

In case that rupture of the bond on linker 1 happens first, the force which will be applied to second linker can be expressed as:

$$f_1 = k_p \frac{k_L d + k_p \Delta L}{k_L + k_p} \tag{5.15}$$

To include bond heterogeneity, we chose $x*$ as a normally distributed random variable with a standard deviation in the range of 10-20%, i.e. each simulated experiment was performed with a randomly chosen value of x^* selected from this distribution.

Results from the simulation are shown in Figure 5.10. It can be seen that both multiple bond formation and bond heterogeneity lead to a high force tail in the force distributions. However, the shape of the tail is quite different: In case of multiple bonding, we see a secondary small peak, while heterogeneous binding produces a high force shoulder, making the distribution more symmetric. Comparing this to our measurements (Figure 5.7), we can see that both a high force shoulder and a secondary peak are present, indicating the influence of both processes.

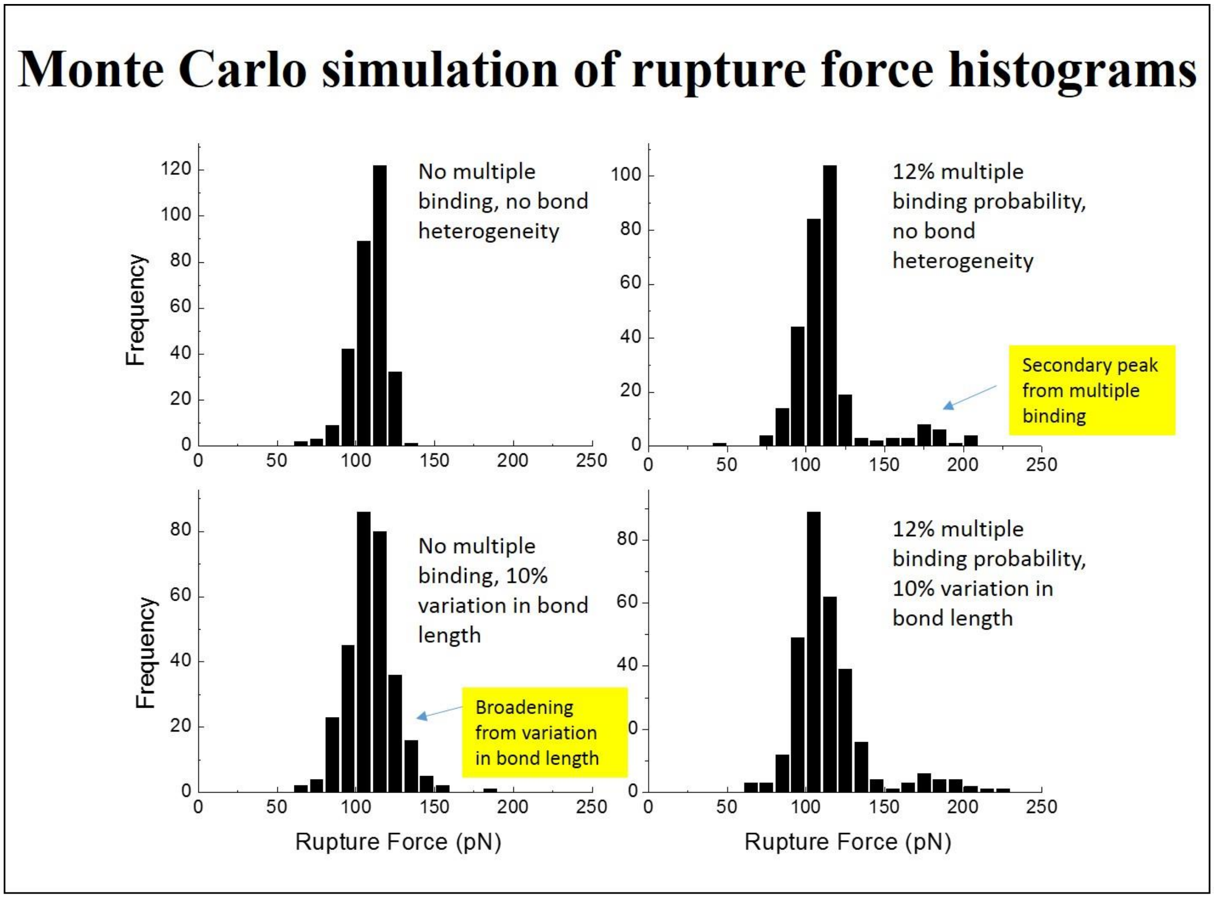

Figure 5.10: Simulated rupture force histograms with different scenarios

5.5. Influence of active site density on measurements

Silane PEG biotin molecules are expected to be about 4.6 nm[59] apart from each other on the surface of the substrate, assuming dense coverage. The number of bonds that can be formed and binding probability both increase with increasing biotin ratios in the low biotin ratio region as number of bonds that can be formed is proportional to the grafting density σ (number of linker molecules per unit surface area) of linker molecules in low biotin ratio region [60].

$$number\ of\ bonds = 2\pi RL\sigma \tag{5.16}$$

Where *R* refers to the interaction radius and *L* refers to the contour length. Grafting density for 100% biotin data can be expressed as

$$\sigma_{100\%} = \frac{1}{(4.6\ nm)^2} = 0.047nm^{-2} \tag{5.17}$$

Similarly, we could calculate the grafting density for samples with 2%, 4%, 20%, 30%, 50% and 100% biotin ratios and determine the number of bonds that can be formed according to equation 5.16. The maximum number of bonds that can be formed for 2% biotin ratio is 3, for 4% biotin sample its 6, for 20% biotin sample its 30, for 30% biotin sample its 45, for 50% biotin sample its 72, for 100% biotin sample its 148. Due to clustering of molecules in the high biotin ratio regions, existence of islands with multiple biotin molecules is plausible. This does not mean that when the avidin functionalized probe is coming very close to those islands, it is always forming multiple bonds, because of the finite interaction time. However, because of these effects, binding probability is not proportional to grafting density σ in the high biotin ratio regions. Overall, the dependence of the binding probability on grafting density follows the pattern of a Langmuir isotherm and saturates at high densities.

For small densities, we can also justify our binding probability results by using Poisson's distributions (which represents the probability of events that occur in a definite interval of spatial separation or time where the events are independent of each other) for a particular biotin ratio. From this, we can calculate the binding probability and double and triple attachment probability theoretically. The Poisson distribution can be written as [61, 62]

$$f(k,\lambda) = \frac{\lambda^k e^{-\lambda}}{k!} \tag{5.18}$$

Where k=0, 1, 2, ……

But first we need to determine the probabilities of no attachments, one attachment, or multiple attachments from our measured data. The binding probability (BP) and multiple attachment probability (MBP) for the 2% biotin sample are given by:

$$BP = (P_1 + P_2 + P_3) = 0.12 \tag{5.19}$$

$$MAP = \frac{(P_2+P_3)}{(P_1+P_2+P_3)} = 0.22 \tag{5.20}$$

Here, P_1 represents the probability of single bond rupture, P_2 represents the probability of double bond ruptures and P_3 represents the probability of triple bond ruptures. By solving this set of equations, we find,

$$P_1 = 0.094 \tag{5.21}$$

$$(P_2 + P_3) = 0.026 \approx P_2 \tag{5.22}$$

$$P_0 = 1 - (P_1 + P_2 + P_3) = 0.88 \tag{5.23}$$

From this we can determine the mean number of attachments to be used in the Poisson distribution as

$$\lambda \approx P_1 + 2P_2 = 0.15 \tag{5.24}$$

From this, we can now calculate the expectation values from the corresponding Poisson distribution, $f(0)$, $f(1)$ and $f(2)$. The theoretically derived binding probability *f(1)*=0.13 matched our experimental result (0.094) reasonably well. The value of $f(2)$ = 0.013 was significantly lower than our experimental result (0.0264), which may indicate clustering.

5.6. Conclusion:

We succeeded in reducing the number of measurements in the high force tail of force histogram by combining biotin PEG and m-PEG to certain percentages and functionalizing substrates with those solutions. We were able to get good force curves as inactive m-PEG sites were able to block multiple attachments, such that the binding probability and zero distance multi-attachment probability were reduced due to reduction of active biotin PEG molecules. However, even at the lowest percentages we used (2% biotin) a significant high force tail remains. The difference between the tail percentage and zero-distance multiple-attachment probability indicates that the unaccounted high force tail in the rupture force histogram cannot be completely attributed to multiple attachments, but may instead be due to bond heterogeneity. Monte Carlo simulations confirmed the importance of possible bond heterogeneity in these types of measurements. They indicate that multiple attachments tend to create a long tail, while bond heterogeneity produced a shoulder in the force histograms.

CHAPTER 6: DDR1-COLLAGEN INTERACTION FORCES

6.1. Introduction:

AFM can be applied to measure Young’s modulus of the cell membrane, cell-cell interactions, receptor-ligand interaction kinetics and receptor distribution on live cells. Live cells must be preserved in cell incubator (with 37^{o} C temperature, 7.3 pH, cell growth medium, air with 5% of CO_2 and sterile conditions). In our experiments, live cells were maintained in the incubator as mentioned above. They were only taken out of the incubator to perform experiments for a few hours. Measurement of the receptor-ligand interaction forces on live cells requires attaching ligands to the AFM cantilever tip. The live cells are typically attached to the bottom of a Petri dish and surrounded by growth medium. In our study, we are interested in the measurement of interaction forces of DDR1 receptors and their ligand, collagen. Upon collagen binding, activated discoidin domain receptors (DDRs) switch on many signaling networks to facilitate normal cellular function. In metastasis state of cancer, hijacking of DDRs by tumor cells causes dysregulated cellular communication and initiates pro-invasive processes. So far, only a limited amount of information is available on these receptors (potential therapeutic targets in cancer research). So, we are using AFM to know more about how DDRs behave in normal and pathological conditions.

6.2. The extracellular matrix:

The extracellular matrix[63] is an assembly of molecules (located outside the cell and deposited by cells) that assists the structural and biochemical activities of the cell. The structure of extracellular matrix (ECM) is different in different multicellular organisms but it serves similar purposes such as communication between cells, cellular adhesion and differentiation.

As a consequence of its various forms and constituents in different systems, ECM is capable of performing important cellular functions including providing support mechanism for cells, controlling cellular communication and transporting cellular growth factors (naturally occurring protein or hormone helping cellular growth)[1, 64]. As a consequence, ECM formation is important for processes such as wound healing, cell differentiation and cellular growth. As such, cell-ECM interactions also play an important role in cancer, where cell growth, cell differentiation and cell migration all become important aspects in disease progression. A clear idea about the ECM components will help us to interpret complicated mechanisms involved in tumor and metastasis state of cancer. For example, metastasis involves local reorganization, destruction and reconstitution of ECM by enzymes. The elastic properties of ECM play a crucial role in cellular adhesion, migration and differentiation.

6.2.1. ECM components:

Elements of ECM are generated by the cells and deposited outside the cell through exocytosis (a transportation process through which cell transmits molecules outside the cell). Those transmitted molecules, especially proteins and glycosaminoglycans (GAGs), form an assembly with existing components of ECM[65-67]. The major components are described as follows:

1) GAGs are carbohydrate polymers which assemble with ECM proteins to produce proteoglycans (densely glycosylated proteins.). Proteoglycans help to keep ECM hydrated and controls the storage of growth factors.

2) Collagen, the most abundant fibrillar proteins in ECM in human body constitutes about 30% of all protein content in a human body. This protein helps to support and stabilize ECM structures[63, 64, 68]. Collagen is deposited by the cell as procollagen. Procollagen proteases catalyze the formation of collagen fibers. Different kinds of collagen present in the ECM are fibrillar and non-fibrillar collagen.
3) Elastins (mainly generated by fibroblasts) are groups of ECM proteins that help to make tissues elastic. They are found in skin, lung and blood vessels.
4) Fibronectins (a form of glycoproteins) join cells with collagen fibers which permit cells to move through ECM. Fibronectins attach to both collagen and integrins (cell-surface proteins) and help in organizing and facilitating movement of cells. Attachment to integrins allows fibronectin molecules in producing dimers (structures created by two same subunits). Fibronectins also bind to platelets at the location of injury and thereby play a crucial role in wound healing.
5) Laminins (proteins mainly located in the basal laminae) form mesh-like structure and prevent ECM from getting damaged by excess force and helps with cellular adhesion.

6.2.2. Cell-ECM adhesion:

Cells attach to elements of ECM in mainly two ways: either by joining the ECM to cellular actin filaments[65] or by joining the ECM to filaments like keratin. Majority of the ECM-cell adhesions is controlled by integrins (cell-surface proteins) which help to link cells to ECM structures (like fibronectin and laminin).The joining of fibronectin to the cell triggers signaling networks and helps in forming an assembly with cytoskeleton.

6.2.3. Creation of ECM:

Many types of cells help in developing ECMs in different tissues. Fibroblasts are most abundant cells of these types which help to synthesize and build structure of ECM by providing the base substance.

6.3. Collagen:

Collagen[1, 69-71] is a naturally occurring protein which is a primary component in the ECM, connective tissues and flesh of animals. Collagen is usually found in the form of long fibrils in tendon, ligament and skin. Fibroblast cells generate collagen[70]. Collagen is also abundant in bone, blood vessels, gut, cornea and cartilage. It serves as an important component of endomysium (a layer of connective tissue that encloses each individual muscle fiber or muscle cell) in the muscle tissue. Collagen comprises of a triple helix structure. All three of these chains are left handed and they twist together to form a super helix. The general motives of amino acid chain of collagen are glycin–proline X and glycine-X-hydroxyproline. Here X represents any unique amino acid other than glycine, proline or hydroxyproline. There are 28 different forms of collagen. Collagen I and Collagen IV bind to ligands DDR1 and DDR2 respectively. Collagen I is found in bone, skin, tendon, vascular ligature, organs and Collagen IV is found in hair, placenta and cell surfaces.

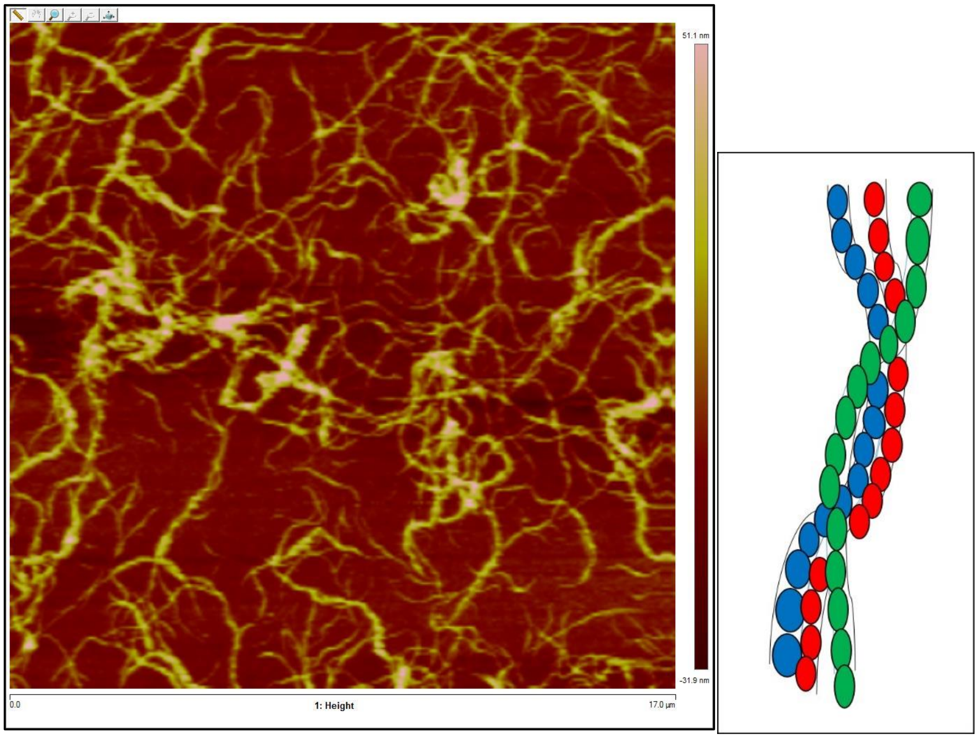

(a) (b)

Figure 6.1. (a) AFM image of rat tail collagen type I attached to glass coverslip (scan size 17 μm), (b) represents polypeptide chains of collagen fibril.

Fibrillar collagen forms structures like fibers and planar layer networks. Collagens[1, 67] which are not fibrillar may create various kinds of supramolecular network.

6.4. Cell surface receptors:

Cell surface receptors[72] or transmembrane receptors are membrane proteins which transduce signals between the cell and the molecules in extracellular components like hormones and growth factors. All of the ECM components react with cell receptors to cause changes in cellular mechanisms. This process of transducing signal involves receptor-ligand binding which triggers chemical changes inside the cell.

6.4.1. Structure and function:

Cell surface receptors[1, 72-78] comprise of multiple peptide chains (strings of amino acid monomers joined by amide molecules). The cell surface receptors usually accumulate on the surface on cell membrane with a heterogeneous spatial distribution. Receptor monomers attach to different ligands, leading to the receptors to dimerize through their interactions with ECM. The capability of membrane proteins to laterally migrate inside the membrane bilayer enables dimerization. Dimerization triggers cell signaling through attached kinase domains through autophosphorylation.

The three domains of cell surface receptors are:

a) EXTRACELLULAR DOMAIN: The extracellular domain extends outside from the cell. It consists of polypeptide chains forming loops. Upon recognition (specific binding) of different ligands like ions and hormones, this domain gets activated (changes shape).

b) TRANSMEMBRANE DOMAIN: The transmembrane domain anchors the membrane protein in the cell membrane. Generally, the transmembrane domain consists of hydrophobic alpha-helix structures.

c) INTRACELLULAR DOMAIN (CYTOPLASMIC DOMAIN): This domain interacts with the area inside the cell and transmits cellular signal. It can either use effector protein (molecules that bind to a particular protein and changes its activity) interaction or receptor linked with enzymes (like tyrosine kinase receptors) to transduce signals.

6.4.2. Transmission of signals through cell surface receptors:

Cell generates extracellular signaling molecules which can move to neighboring cells. These signaling molecules attach to receptor proteins and transmit the signal inside the cell through a conformational change of the receptor. The conformational change of the intracellular domain of the receptor activates intracellular signaling proteins and triggers several signaling networks. Activated signaling pathways vary the behavior of the target proteins and these proteins modify the cellular behavior.

6.4.3. Role of kinase in signaling:

Enzyme-coupled receptors can be subdivided into six categories: receptor-like tyrosine phosphatases, receptor tyrosine kinases, receptor serine/ threonine kinases, tyrosine kinase associated receptors, histidine kinase associated receptors and guanylyl cyclase receptors. They behave like enzymes and activate signaling networks when they get stimulated. These receptors respond to extracellular signal proteins which control cellular growth, cell differentiation and cell survival strategies.

Among these receptors, we are mainly dealing with one particular kind of receptor tyrosine kinases (RTK)[79-82] in our project. RTKs are transmembrane receptors for hormones and growth factors and these receptors belong to the bigger family of protein tyrosine kinases. Tyrosine is an amino acid that cells employ for synthesis of proteins. There are 20 different classes of RTKs that have been identified (example: EGF receptor family and insulin receptor family). RTKs control normal cellular processes as well as regulate progression of many types of cancer. Majority of these receptors exists as a monomeric unit in the beginning but there are few RTKs which form dimeric or multimeric complexes initially before ligand binding (for example: insulin receptor family). Upon ligand binding to the ECM portion of the initial monomeric RTKs, they form dimers. The monomeric state of these receptors comprises of 25-38 amino acids, N terminal section (extracellular part) and C terminal section (intracellular part). The extracellular part of these receptors forms ligand-binding regions to bind to ECM ligands. The intracellular part of these receptors comprises of catalytic domains which stimulate kinase activity within RTKs and autophosphorylation of receptors.

Kinase is an enzyme which stimulates the transit of phosphate groups from particles of high energy like ATP to another substrate. The attachment of a phosphate group to a protein is termed phosphorylation. Phosphorylation and the reverse process dephosphorylation can activate and deactivate enzymes and modify their functions. As a consequence, these two processes play a crucial role in most of cellular processes like activating signaling networks, transmitting signals and secreting particles. The phosphorylation state of a molecule, whether it be a protein, lipid, or carbohydrate, can affect its activity and its ability to bind other molecules. Therefore, kinases are critical in metabolism, cell signaling, protein regulation, cellular transport and secretory processes.

6.5. Integrins:

Integrins[83, 84] (types of transmembrane receptors) are the main receptors involved in direct interactions among cells and the ECM. For example, these receptors transmit signal to platelets to initiate interaction with coagulation factors to help wound healing. Activated integrins initiate chemical signaling networks to transmit signal inside the cell, typically by modulating the behavior of associated receptor tyrosine kinases (RTKs). Integrins work in cooperation with other transmembrane receptors like cadherins. Integrins bind to collagen, laminin and fibronectin. Integrins consist of two separate α and β chains. Number of α and β subunits varies in different organisms.

6.5.1. Structure:

The complete structure of integrins (other than α5β3) is not understood despite of application of light scattering, X-ray crystallography, nuclear magnetic resonance and other high resolution imaging technique to explore the integrin chains. The ligand binding sequence of integrins is assumed to trigger changes in cell behavior. Changes in shape of these receptors make ligand-binding sites available to cells and initiates intracellular signaling.

6.5.2. Activation:

Freshly synthesized integrin dimers are discovered in the ‘bent’ conformation. This conformation is assumed to prevent the interaction between the integrins and their ligands. The α and β chains of integrins are class-I transmembrane proteins and they go through the cell membrane in the form of single transmembrane long helices. The helices are tilted with respect to each other and the plane of the membrane. Talin, another cellular protein, binds to integrin β chain tail, changes the angle of the tilt for integrin and activates integrin.

6.5.3. Function:

The two major functions of integrins are:

1. Cell- to-ECM attachment
2. Transmission of signal from the ECM to the cell

Integrins link the ECM to the cytoskeleton inside the cell. Depending on the constituents-α and β subunits, integrins can attach to ligands like fibronectin, collagen, laminin and vitronectin[1, 41, 85, 86]. The bridge between ECM and cell support the cell to withstand forces without getting detached from the ECM. The connection between cell and ECM serves as the building block for a multicellular organism[1, 87, 88]. Integrins help to transmit critical signals to cell about its immediate surroundings. The attachment process of cell involves creation of cellular adhesion assemblies. These assemblies consist of integrins and other proteins like talin and paxillin. These control kinases like focal adhesion kinase (FAK). The integrins link membrane networks of ECM and the actin filamentous system inside the cell. Focal adhesions (larger molecular assemblies) are created by the interaction of ECM and integrins and these molecular assemblies contribute towards forming balanced signaling complexes[1, 87, 88]. Integrins play a very important role in signaling by regulating the cellular signaling pathways of protein kinases. The regulatory effects of integrins on receptor tyrosine kinases [89-93] enable normal cellular functions like cell growth, division, survival and differentiation. Connections between integrins and tyrosine kinase receptors lead to select new therapeutic targets in curing cancer.

6.5.4. Types of integrins:

Different major types of integrins are $\alpha_1\beta_1$, $\alpha_2\beta_1$, $\alpha_3\beta_1$, $\alpha_4\beta_1$, $\alpha_5\beta_1$, $\alpha_5\beta_1$, $\alpha_5\beta_3$ and $\alpha_5\beta_5$. Different ligands for these different types of integrins include collagen, firbronectin, laminin, fibrinogen and vitronectin.

6.6. Discoidin domain receptors (DDRs):

DDRs[10-12] are tyrosine kinase receptors and are found in the plasma membrane of cells. There are two common mammalian DDRs: DDR1 and DDR2. Molecular weights of DDR1 and

DDR2 are, respectively, 125 and 130 kDa. The binding of collagen to the extracellular domain of DDR stimulates the activation of the tyrosine kinases inside the cell to generate a signal through phosphorylation. Autophosphorylation of DDRs usually take a long time compared to other receptor tyrosine kinases. The two types of DDRs display tyrosine phosphorylations which are capable of relaying the signal by interacting with cytoplasmic effector proteins. These proteins enter substructures inside a cell and they are gathered into a complex structure. DDRs play a role in the regulation of collagen, wound healing, cell proliferation and gland development[1, 10, 11, 94, 95]. DDR1 and DDR2 have been related to human cancers over the past few years. These receptors serve as potential novel therapeutic targets in cancer research and experiments. That is why we are interested to study more about their behavior and interactions using AFM.

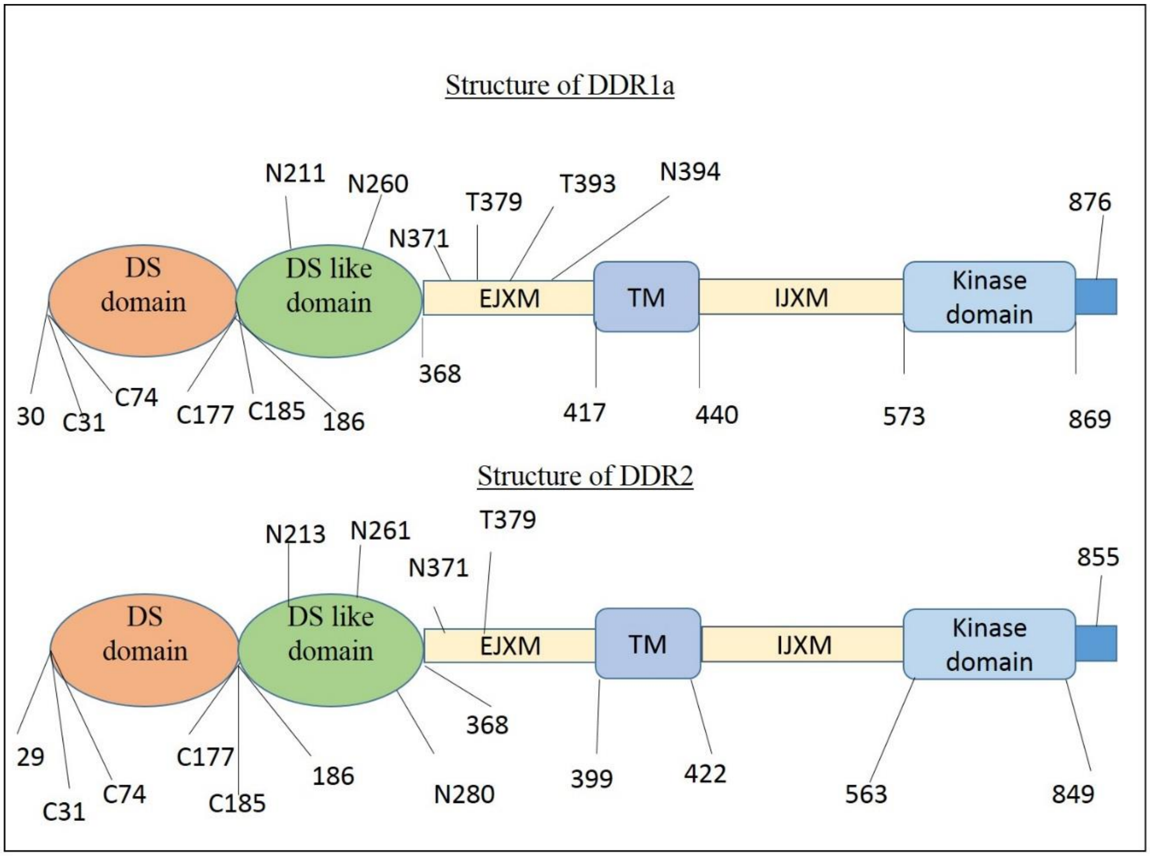

Figure 6.2.Basic structure of DDR1a and DDR2

Fig 6.2 shows the basic structure of DDR1a [95] and DDR2. DDR1 and DDR2 are type I transmembrane glycoproteins which are types of membrane proteins crossing the entire cell membrane. These proteins are permanently attached to the membrane. DDRs are characterized by the presence of six different segments: a discoidin[17] domain, domain, a DS-like domain (discoidin like domain) an extracellular juxtamembrane (EJXM) region, a transmembrane (TM) segment, a long intracellular justramembrane region (IJXM), and an intracellular kinase domain [96]. DDR collagen binding sites are located within the DS domain. Upon collagen binding to the DS domain, the cytosolic kinase domain becomes activated and sends a cellular signal. The cellular responses are generated in the following way:

Receptor tyrosine kinases appear as monomers initially with their extracellular regions in the ECM and intracellular regions in the cytoplasm. Upon binding of signaling molecules or ligand molecules to extracellular regions of these receptors, they dimerize. This leads to conformational changes of the tyrosine kinases and activation of the receptors. Their activation leads to phosphorylation which transfers the phosphate groups from multiple ATP molecules to multiple tyrosine kinases. These activated and phosphorylated receptors have sections floating in the cytoplasm and the inactive relay proteins of cytoplasm attach to those sections and get activated. As more than one relay protein can attach to these dimers, one tyrosine kinase receptor system can cause at least 10 cellular responses leading to regulation of cell growth in a more efficient way.

Research studies focused on the structural details of DDRs have found that DS domains are composed of two antiparallel sheets of eight β sheets (within jellyroll configuration). This domain has six loops in the topmost position which form a pattern that binds to collagen. The structure is strengthened by four cysteine residues, which form two disulfide bonds. These residues are Cys-74, Cys-177 (these two residues link loops 2 and 6), Cys-31 and Cys-185[1, 10, 11, 94, 95].

Differences in patterns or sequences in the loops determine the specificity for a particular ligand among constituent proteins of DS domain. Residues from first, second and fourth loops play a crucial role in fibrillary collagen binding and therefore control collagen-DDR interactions. Separate regimes inside the DS domain have the ability to distinguish fibrillar collagen from non-fibrillar collagens. DS-like domain (which consist of 182 residues) is the segment that follows DS domain. This domain also consists of two antiparallel layers made of eight β strands. The DS-like domain comprises five extra filaments extending between the first and second filaments. The exact role of the DS-like domain is not completely known. However, research data so far indicates that it plays a role in receptor activation, induced by collagen.

In case of human DDR1s, the EJXM region has 49 residues in DDR1. The EJXM regime has 31 residues in DDR2. The EJXM segment (containing many N-glycosylation and O-glycosylation sites which may contribute to ligand induced receptor activation) links the DS domain to the transmembrane domain. The transmembrane domain (containing 20 residues) connects the ectodomain (ectodomain is a domain made of membrane proteins that extends into the space outside the cell) and the intracellular domains of DDRs. This domain also plays a crucial role in receptor dimerization. This shorter segment comprises of a set of leucine residues (assumed to build leucine zipper motif which is important for signaling of the receptors). A very long IJXM region (consisting of 130 –140 residues) links the transmembrane domain with the kinase domain. This region contains a large number of tyrosine residues (assumed to construct docking regimes for cytoplasmic regulators that are needed for transduction of signal). A kinase domain (containing

300 residues) comes after IJXM regimes in DDR2, DDR1a, DDR1b, and DDR1c. Upon collagen binding, kinase domains gets activated and sends cellsignal[1, 10, 11, 94, 95].

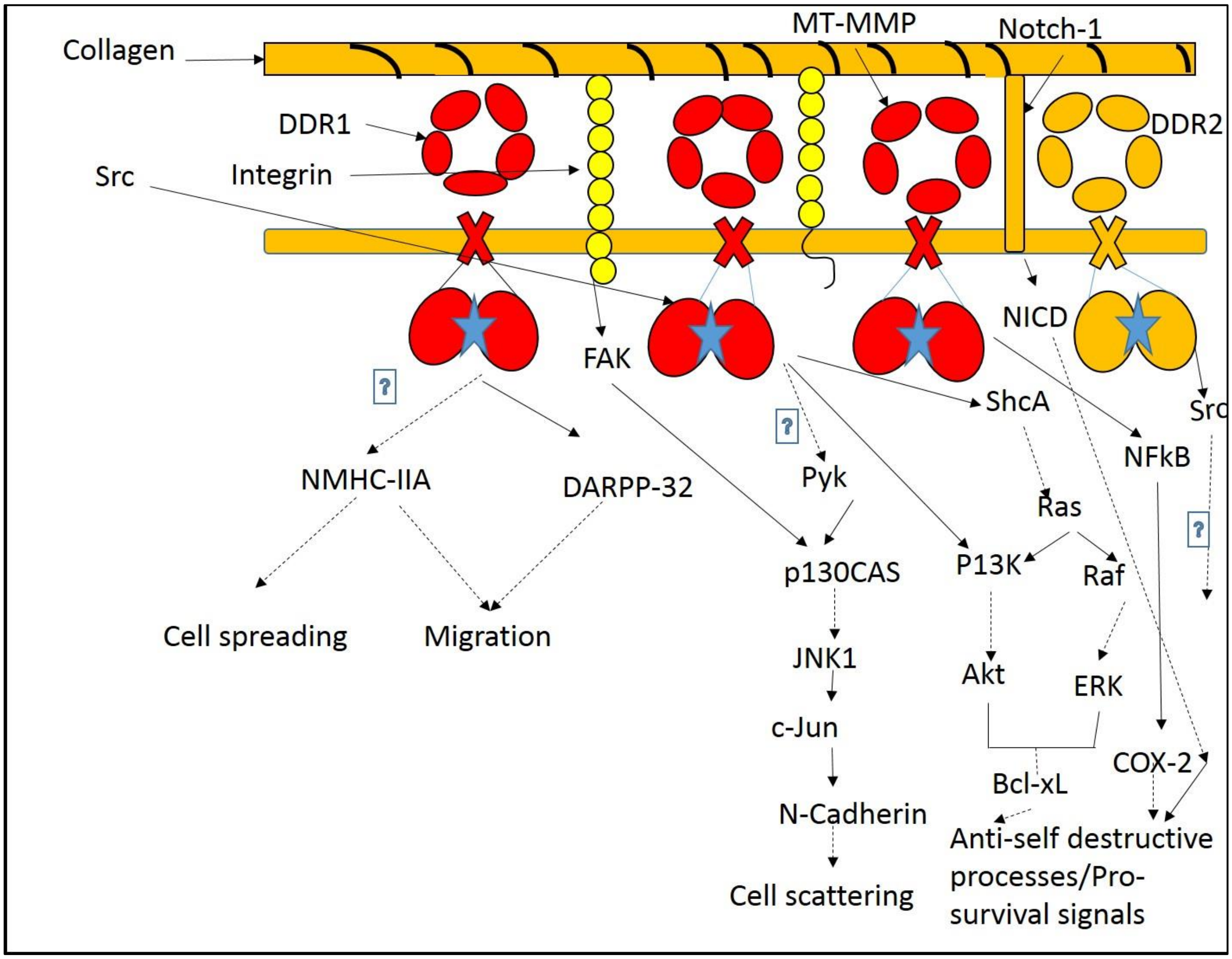

Figure 6.3.Role of DDRs and other receptors in downstream signaling pathways

Figure 6.3 sums up DDR controlled downstream signaling events (especially those recognized in cancer cells) supported by other receptors. Solid lines in this picture represent direct effects. Dashed lines indicate indirect interactions or effects that involve intermediate steps. Unknown interactions are represented with a question mark. Activated DDRs are represented by a blue star.

Among all these receptors mentioned in the picture, DDRs and integrins are the two most broadly expressed receptors of collagen. With DDR1 playing a crucial role in organogenesis and DDR2 helping in growth of bones, both of them seem to be very important in development. Female mice, deficient in DDR1 demonstrate many reproductive defects. Unusual mammary gland branching was also noticed in those mice. The deficiency of DDR1 also leads to kidney and inner ear defects. Expression of DDR1 has been noticed during the entire mammary development in case of normal mice. It has been proved that DDRs took part in signaling pathways which control lactation. DDR1 regulates cellular sinalling, differentiation and synthesis. In mice, DDR1 and α2β1 integrin control different stages of the mammary gland branching and they don't work in conjunction in this case. In mice, DDR2 has been noticed to regulate gonadal functions and deficiency of DDR2 in mice caused dwarfism. DDR2 plays a major role in bone growth. In case of osteoblasts, the interaction of DDR2-collagen leads to secrete an enzyme which stimulates collagen fibers' cross linking and this procedure is important step in bone strength.

DDR2 is also important in skeletal growth in human and the deficiency of DDR2 leads to short limbs. DDR2 mutations have been noticed in the human cancer cell lines and the mutated DDR2 couldn't bind to collagen because of that. So, this mutated DDR2 could lead to abnormalities in human skeletal growth.

6.7. Role of DDR and collagen in cancer and motivation behind our study:

By regulating interaction of tumor cells with their surrounding collagen matrix, DDRs[12, 71] function as a vital receptor in cancer. For example, activation of DDR enhances NFkB DNA binding activity in breast cancer cells (human) which leads to higher chemoresistance. NFkB is protein assembly that regulates transcription of DNA and cell survival. DDR1 builds a complex in conjunction with Notch 1 in human colon cancer cells. Activation of DDR starts Notch1 cleavage (leading to upregulation of pro-survival genes like Hes1 and Hey2). Notch1 is a human gene which encodes a transmembrane receptor. Joint activation of DDR1 and integrin β1 in pancreatic cancer cells start JNK pathway which upregulates N-cadherin. Cadherins are transmembrane proteins whose functions are dependent on calcium ions and these proteins play crucial role in cellular adhesion. In spite of a lot of research effort, signaling pathways of DDR2 in cancer cells are still undiscovered.

The variation in DDR genes in human cancer cells imply that advancement of disease can be influenced by DDR. Research studies have so far provided only little information about DDR behavior at the cell-collagen interface. That is why we are making an experimental effort by combining biological information and force based microscopy techniques to shed light on how DDRs function in physiological and pathological conditions.

DDR receptors activate after ligand binding and transmit signal into the cell. They activate many signaling pathways to enable regular cellular function. In case of cancer, tumor cells hijack DDR receptors which leads to disorder in the regular cellular communication and starts pro-invasive procedures. Many types of cancers exhibit mutations of DDR. These mutations are presumed to change functions of DDR and play a crucial role in advancement of cancer. There is a significant gap in what we know about actions of DDR in cancer.

Majority of the advancement in DDR research has been done in human lung cancer as dysregulated expression or function of DDR has been found in lung carcinomas. These receptors may serve as potential new targets for tyrosine kinases inhibitors (TKIs). Procedures targeting activity and function of tyrosine kinases include chemical molecules structured to disrupt intracellular kinase activity. Small molecule TKIs bind to active or inactive kinase intervening the transmission of phosphate to proteins with a tyrosine residue. The framework of the kinase domain makes it difficult to design TKIs. So far, imatinib, nilotinib, and dasatinib have been identified and used as DDR1 inhibitors. Dasatinib was found to prohibit mutated DDR2 in lung cancer cells which implies that patients with mutated DDR2 may benefit from dasatinib treatment.

6.8. Planned work:

We plan to perform a detailed measurement of DDR1-collagen interaction using AFM. In particular, we are planning the following studies:

a) Measure the kinetics, bond length and activation energy of DDR1-Collagen interaction at single molecular level on live cells, using both over expressed and wild type cells, as well as cancer cells.
b) Develop methods to take multiple attachments into account and obtain clean single-molecular data.
c) Compare the measured DDR1-Collagen interaction on live cells with the interaction between the extracted extracellular DDR1 and collagen plated on the substrate to determine how the interaction is affected by the cell microenvironment.
d) Determine the distribution of DDR1 on live cells using fluorescence microscopy and AFM based adhesion mapping.

Our planned work will progress in two stages: at first, we will perform measurement of DDR1-collagen interactions on live cells and then we will work with soluble DDR fragments, which can be attached to a tip or substrate. Soluble DDR1 is prepared by removing the transmembrane and intracellular (kinase) part, and attaching the extracellular part to the Fc region of an antibody. The attachment procedure we usually use in attaching proteins (see Chapter 5) is highly non-specific, and it is not clear in what orientation or what part the DDR1-Fc fusion protein will attach to the substrate. An alternative method is to attach the antigen of the Fc (in this case G protein) to the cantilever tip. Then Fc will naturally attach to the G-protein, and all DDR1s will be attached in the same and correct orientation.

6.9. EXPERIMENTAL SAMPLE PREPARATIONS AND ATTACHMENT PROTOCOLS:

6.9.1. Cell culture and passaging:

We collected three different kind of cells – BPH1 cells[97, 98] (benign prostatic hyperplasia cells), BXPC-3 cells[99] (pancreatic cancer cells) and MiaPaCa-2 cells[100-103] (human pancreatic cancer epithelial cells) from department of pathology and cultured them for our experiment.

Table 6.1: It summarizes all different types of cells with modulated expressions of DDR1, used in our experiments

Cell	Type	DDR1

$BPH1_{scr}$	Human benign prostatic hyperplasia	+
$BPH1_{shDDR1}$	Human benign prostatic hyperplasia	-
MiaPaCa-2 EV	Human pancreatric cancer cells	-
MiaPaCa-2 DDR1b	Human pancreatic cancer cells	+
MiaPaCa-2 DDR1b R105A	Human pancreatric cancer cells	+mutant

All these cells were cultured in Roswell Park Memorial Institute medium or RPMI medium[104] with HEPES[105] strengthened by 10%FBS[106], 1% penicillin/streptomycin and 1% L-glutamine. We passaged the cells in the culture flask every fifth day and changed the media (RPMI media with 10% FBS) every second day. We used the following method for passaging cells:

1) We first pipetted the culture media out of the cell culture flask.
2) Next, we rinsed the flask with 5 ml warmed up (37°C) Dulbecco's Phosphate-Buffered Saline or DPBS media and pipetted that media out.
3) We added 0.7 ml Trypsin to the flask and kept it inside incubator for 5 minutes.
4) Next, we took the flask out of the incubator and tapped the bottom of the culture flask in order wake the cells up.
5) After that, we added 2.8 ml RPMI media mixed with fetal bovine serum (FBS) in the flask.
6) We pipetted the entire media back and forth to mix everything well and took 0.5 ml out and placed that into a new fresh culture flask. We used new culture flasks for further culture.
7) We added 4.5 ml RPMI with FBS to the new flask.

8) We kept doing these passaging procedures until the cells are 80% confluent and they are ready to attach to petridish bottom. We took 0.35 ml media from the old flask and added 3ml RPMI media with FBS to each petridish. We used these 50 mm petridishes for experiment.
9) On the day of the experiment, we replaced the media in the petridishes with RPMI without FBS twice (with four hour gap between the two trials) and kept them inside the incubator for at least 30 minutes. After that, we took them out for AFM imaging and force measurements. We placed the petridish (with cells attached to the bottom of it) on the base plate and fixed it with sample holder clamps for 50 mm petridish.
10) Imaging and force measurements were performed in warmed up RPMI media without FBS in it.

6.9.2. Protocol for attaching rat-tail collagen1 to cantilever tip:

We prepared a pH 5 solution by mixing 0.68 g Monosodium phosphate ($NaH_2 PO_4$), 0.02 g disodium phosphate ($Na_2 HPO_4$) and 0.88 g sodium Chloride (NaCl) in 100 ml DI water. We took 1 ml of that solution and mixed it with 0.5ml rat tail collagen type I (purchased from Advanced Biomatrix with a concentration of 4mg/ml). We mixed the solution well and extracted 1 ml. We diluted 8.5 mg LC-SPDP (succinimidyl 6-(3(2-pyridyldithio)propionamido)hexanoate) in 1 ml Dimethyl sulfoxide (DMSO) solvent. We pipetted 0.025 ml of the LC-SPDP solution out and combined it with previously extracted 1 ml collagen solution. We kept this aside and started diluting 23 mg dithiothreitol[107] (DTT or Cleland's reagent) into 1 ml sodium acetate buffer (with pH 5.2). Both DTT and LC-SPDP were purchased from Thermo Scientific. We attached OBL-10 (purchased from Bruker Corporation AFM probes) cantilever to the bottom of an adhesive blue cap and made sure that it is properly fixed. We covered the cantilever first with 0.1 ml of the collagen and LC-SPDP mixed solution and then added 0.05 ml of DTT solution on top of it. We wrapped the entire blue cap with parafilm to prevent any kind of contamination and placed it on a shaker for 2 hours. We took it off the shaker after that time period and pipetted the solution out very carefully (with the smallest volume pipette we have). We rinsed the cantilever very carefully with ultra DI water. We covered the cantilever with 1×PBS buffer and wrapped the blue cap with parafilm again and placed it inside a refrigerator (at a temperature of 4 °C) until experiment is performed. As it is preferred to perform the experiment on the same day to prevent degradation of the sample, we always took the cantilever out after an hour (during which we worked on setting the AFM up) for experiments.

6.9.3. Protocol for attaching DDR1-Fc fusion protein to cantilever tip:

We cleaned OBL-10 (purchased from Bruker Corporation) AFM probes cantilever with hexane, ethanol and ultra-DI water to remove hydrophobic and hydrophilic contaminants. This step was followed by gently blow-drying the samples with high-purity nitrogen. The cantilever holder with the cantilever was then immersed in the mixed solution of 5% carboxylic PEG-SH (CT(PEG) with averaged molecular mass of 3400 Da) and 95% methoxyl PEG (mPEG with averaged molecular mass of 2000Da) inside a clean container. The top of the container was covered with high purity nitrogen and the container was placed on the shaker for 2 hours of incubation inside the biohood. After incubation, the cantilever was again rinsed with ultra DI water and it was transferred to a clean container, covered with room temperature phosphate buffer saline (1× PBS buffer with pH 7.2). The container was then stored in refrigerator at 4 °C overnight. The cantilever was taken out of buffer the next day and kept outside for 1 hour so that the temperature of the solution reaches room temperature and the following procedures were executed in order to functionalize the cantilever tip with protein.

a) Reaction with EDC: the cantilever was rinsed with 350 μL PBS buffer. After that it was incubated with 0.05M EDC (1-ethyl-3-(3-dimethylaminopropyl)) solution for 15 minutes. Finally it will be washed three times with PBS buffer.

b) Reaction with NHS: the cantilever was reacted with 0.05M NHS (N-hydroxysuccinimide) solution for one hour. Then, it was washed three times with PBS buffer.

c) Reaction with protein G: The cantilever was then incubated with 0.05 M 5.11ml solution of protein G[108-110] for one hour. After that, it was washed for one time with PBS buffer.

d) Reaction with ethanolamine-HCL: the surface of the cantilever was blocked with 0.1 M solution of ethanolamine-HCL for 15 minutes and the cantilever was washed four times with PBS buffer.

Finally the cantilever was again transferred to a clean container filled with 5 ml of PBS buffer and preserved in refrigerator at 4 °C until experiment. We performed control experiments with just protein-G functionalized cantilever and collagen-coated substrates. In order to attach rhDDR1-Fc Chimera (purchased from R&D systems) fusion protein to the protein-G functionalized cantilever, we incubated the same cantilever in DDR1-Fc solution (using 25 μg) for 2 hours. We performed experiments again with soluble DDR1-Fc functionalized cantilever and collagen-coated glass coverslips.

6.9.4. Protocol for attaching rat tail collagen to the glass coverslip substrate:

We first incubated the 25×25 mm square glass coverslips in Agilent cleaning solution for 2 hours and rinsed it with ultra DI water and air dried it inside biohood. We dissolved acid soluble rat tail collagen type 1 (4 mg/ml) in a solution of acetic acid using 0.1% acetic acid solution. To prepare the acetic acid solution, we took 1 ml of the glacial acetic acid (3 M) with 10 ml of ultra DI water. We took 1 ml from that solution and mixed it with 10 ml ultra DI water. We repeated the last step again to finally have 11ml 0.1% acetic acid solution. As 100 μg/ml working concentration is preferred, we mixed 0.5 ml of the rat tail collagen type I (4 mg/ml) with 4 ml of 0.1% acetic acid solution. We added 2-3 drops of diluted collagen to each of the clean coverslips and incubated them at room temperature (the coverslips were kept inside a clean glass petridish covered with a lid) for 2 hours. We pipetted out the remaining solution after 2 hours of incubation. We rinsed top surface of the coverslips with sterile 1×PBS buffer very carefully and air dried them inside a biohood to prepare them for AFM measurements.

To make sure that collagen I is properly attached to the cantilever, we performed fluorescence imaging (with 488 nm laser) with collagen (collagen is auto-fluorescent) on the tip and a clean glass coverslip as substrate. We could see a small collagen fibril fragment in the field of view (Figure 6.4).

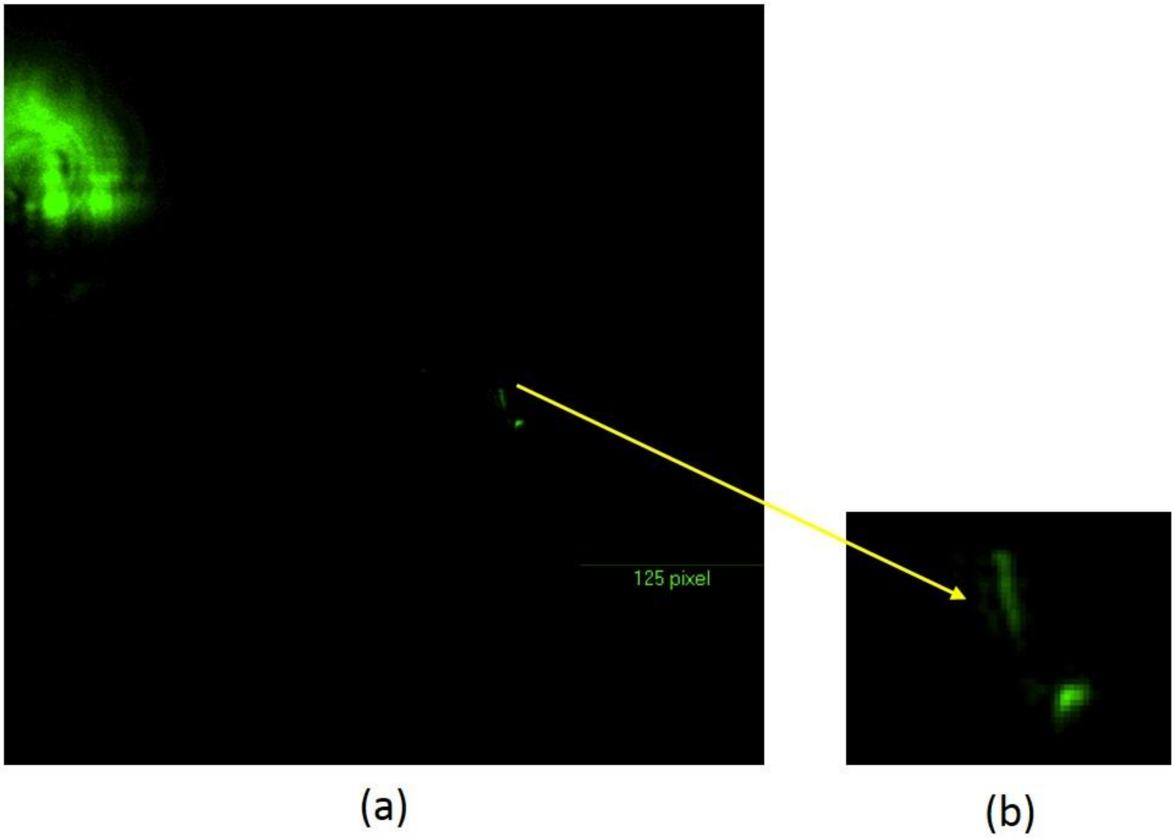

Figure 6.4: (a) Fluorescent image of collagen attached to the cantilever tip (5.3×5.3 inch) and (b) Zoomed-in image of collagen fibril fragment

6.10. Force measurements:

First we performed control experiments (imaging and force measurements) with BPH1 and BXPC-3 cell lines which express or do not express DDR (attached to the bottom of a 50mm petridish) and unfunctionalized DNP-C cantilever (purchased from Bruker and with spring constant of 0.24 N/m). We did not observe any specific binding event in our control experiments. Next, we performed AFM imaging and force measurements using BPH1 cells (BPH1scr, parental $BPH1_{shDDR1}$, MiaPaCa-2 EV, MiaPaCa-2 DDR1b, MiaPaCa-2 DDR1b R105A) with collagen I functionalized OBL-A cantilever. As we are only interested in DDR1-collagen interaction, we used fibronectin (ECM glycoprotein which binds to integrin receptors) in the flow cell in order to block the forces generated by interactions of collagen 1 and integrin. We injected 0.25 ml of fibronectin in the cell petridish after performing force measurements. We waited for 5-6 minutes and performed force measurements for BPH1 cells (BPH1$_{scr}$, parental BPH1$_{shDDR1}$).

In order confirm the results from the integrin blocking procedure, we chose MiaPaCa-2 cell lines (MiaPaCa-2 EV, MiaPaCa-2 DDR1b, MiaPaCa-2 DDR1b R105A) to perform the same experiments without and with integrin blocking antibody (AII B2 –anti beta integrin 1 blocking antibody with concentration 262 μg/ml) and fibronectin for comparison purpose. We maintained a very low scan rate of 0.3 Hz and chose 0.05 as gain and also maintained a low scanning force of less than 1nN (specifically 700 pN in most cases) to prevent the cell from getting damaged. We performed force measurements on cells of different shapes and different locations on other substrate to validate the data for all possible cell shapes.

6.11. Results and Discussion:

Fig6.5 represents microscopic view of BPH1 cells (BPH1scr, parental BPH1$_{shDDR1}$).

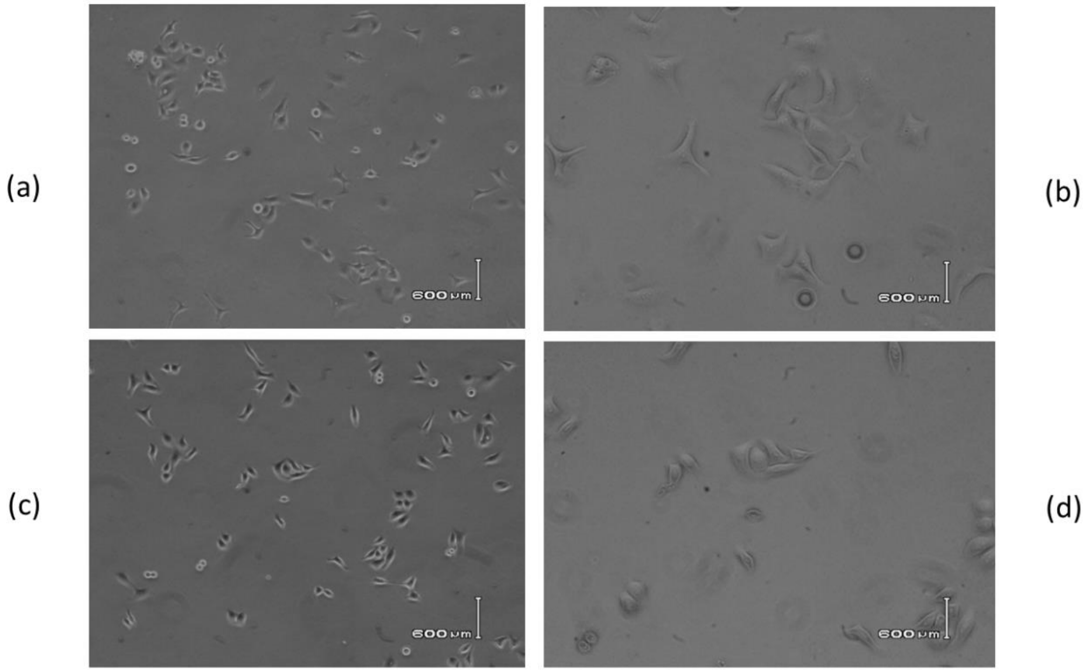

Figure 6.5: (a) Microscope images of the BPH1$_{\text{shDDR1}}$ cells at 10X magnification (b) Same cells with magnification 20X; (c) Microscope images of the BPH1$_{\text{scr}}$ at 10X magnification (d) Same cells at magnification 20X.

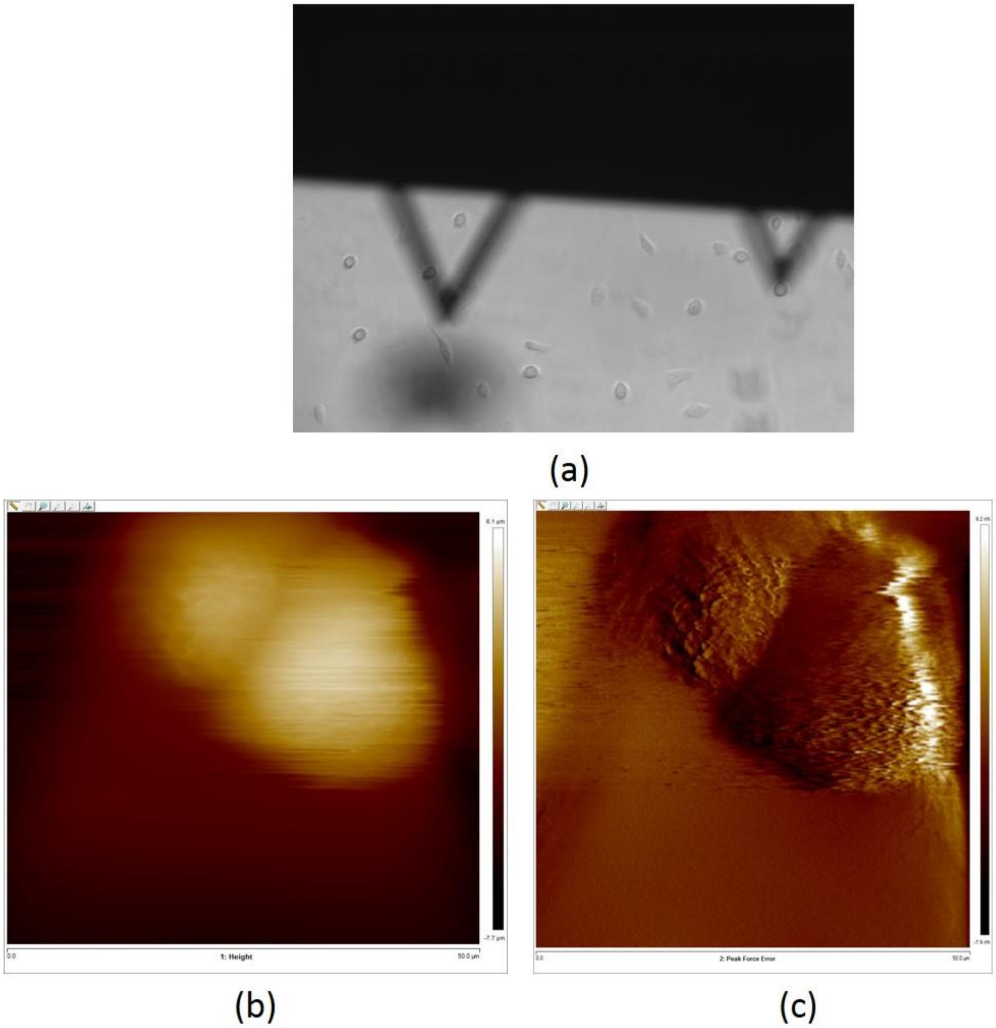

Figure 6.6: (a) BPH1$_{shDDR1}$ cell with AFM cantilever; (b) AFM height profile and (c) AFM peak force error image of a particular cell

First we performed experiments on BPH1$_{shDDR1}$ cells. AFM imaging was done when the cells were attached at the bottom of a 50mm Petri dish. In the Figure 6.6(a), we can see the AFM cantilever scanning on top of a cell and in the bottom images (b) and (c) we see the height image and the peak force error image of that cell. Fig 6.7 represents the field of view where an unfunctionalized

DNP-C cantilever is scanning on top of a BPH1$_{scr}$ cell.

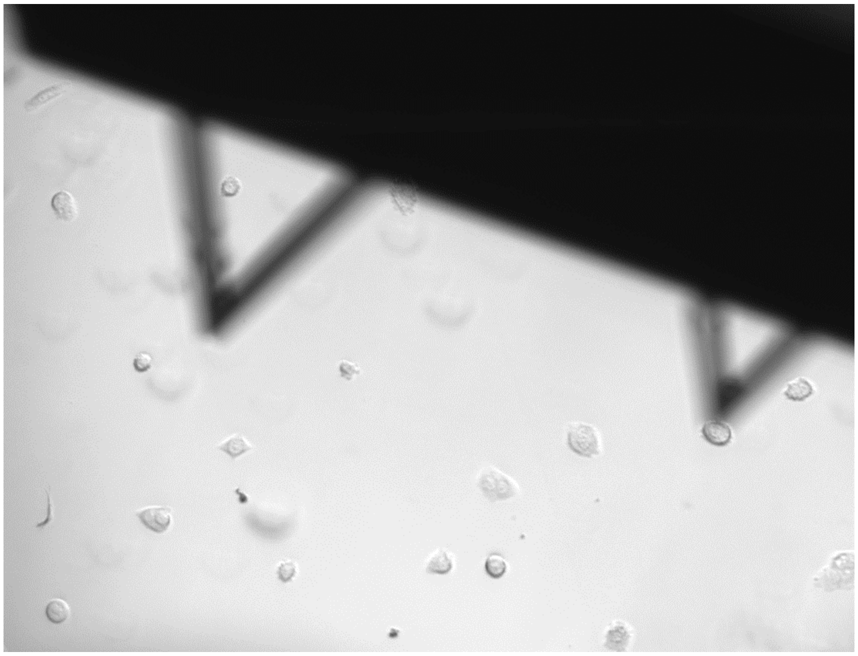

Figure 6.7: It shows the field of view where unfunctionalized DNP-C cantilever is scanning on top of a BPH1$_{scr}$ cell

Just like BPH1 cells (BPH1$_{scr}$, parental BPH1$_{shDDR1}$), we performed some control experiments (AFM imaging and force measurements) with BXPC-3 cells. Fig 6.8 represents the AFM image of a particular cell, the cantilever tip is scanning on. Fig 6.9 represents the control force curves performed on BPH1$_{scr}$. We did not notice any significant attachment in those force curves.

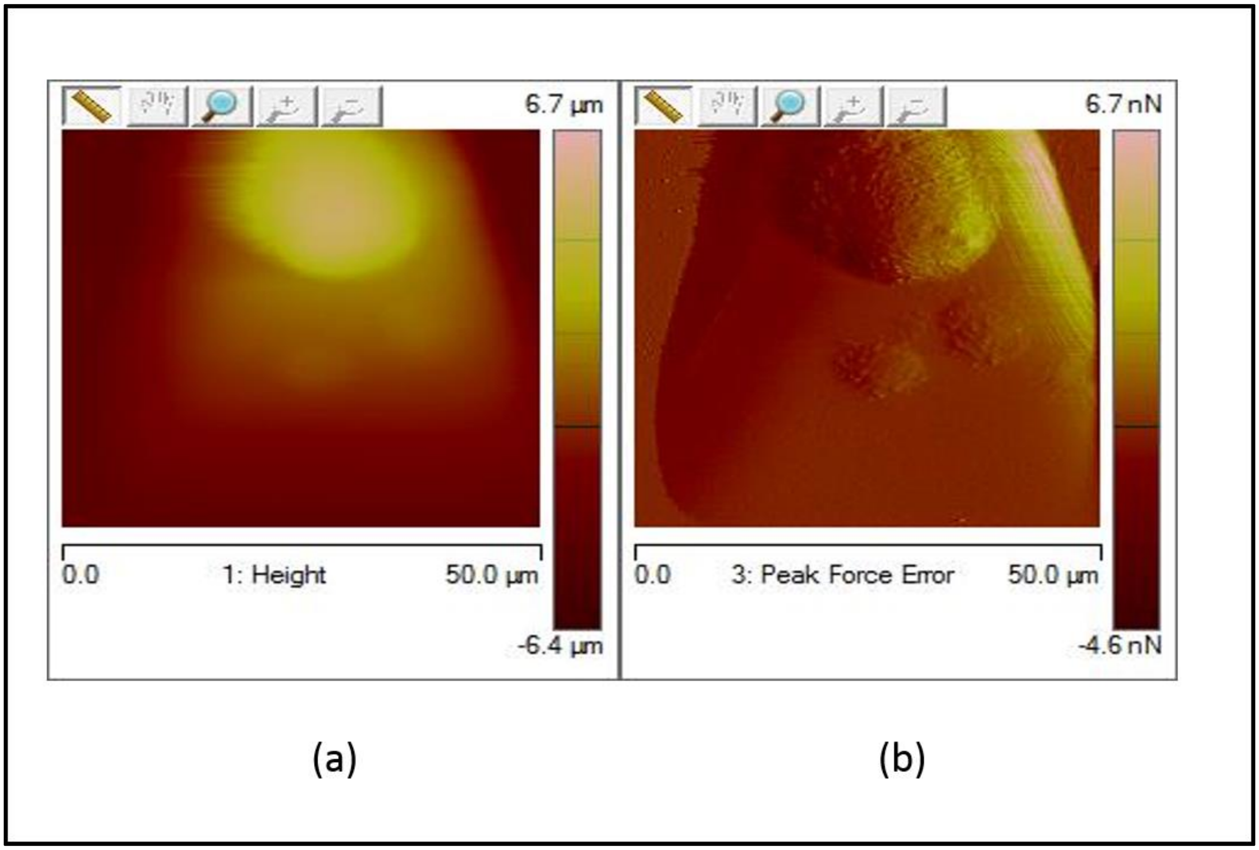

(a)

(b)

Figure 6.8: (a) represents the height image of BXPC-3 cell scanned with DNP-C cantilever and (b) represents the peak force error image of BXPC-3 cell.

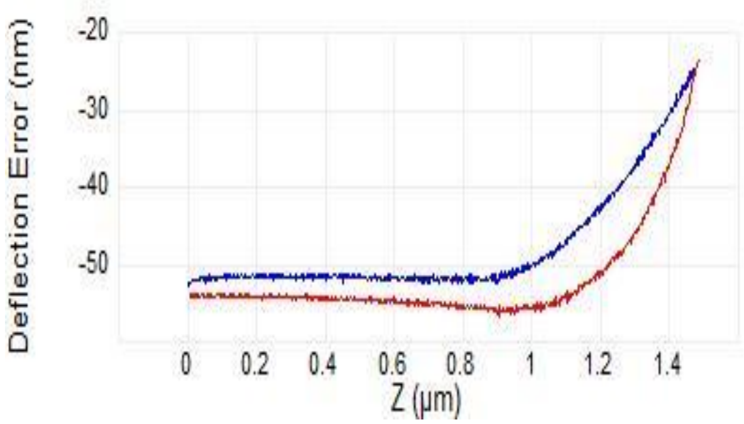

Figure 6.9: represents example of control force curves performed on the BPH1$_{scr}$ cells where the blue line represents the approach curve and red line represents the retract curve

After having good control experimental data to compare with, we functionalized the OBL-10 cantilever with rat tail collagen type I. Fig 6.10 shows collagen functionalized OBL-A cantilever scanning on top of a BPH1$_{scr}$ cell and other cells in the field of view. Fig 6.11 represents the AFM images of BPH1$_{scr}$ cell scanned with collagen functionalized OBL-A cantilever with scan sizes of 40 µm and 20 µm and with a scan rate of 0.3 Hz. Figure 6.12 demonstrates examples of force curves with single and double binding events that we noticed by scanning collagen functioned OBL-10 cantilever on top of BPH1scr cells.

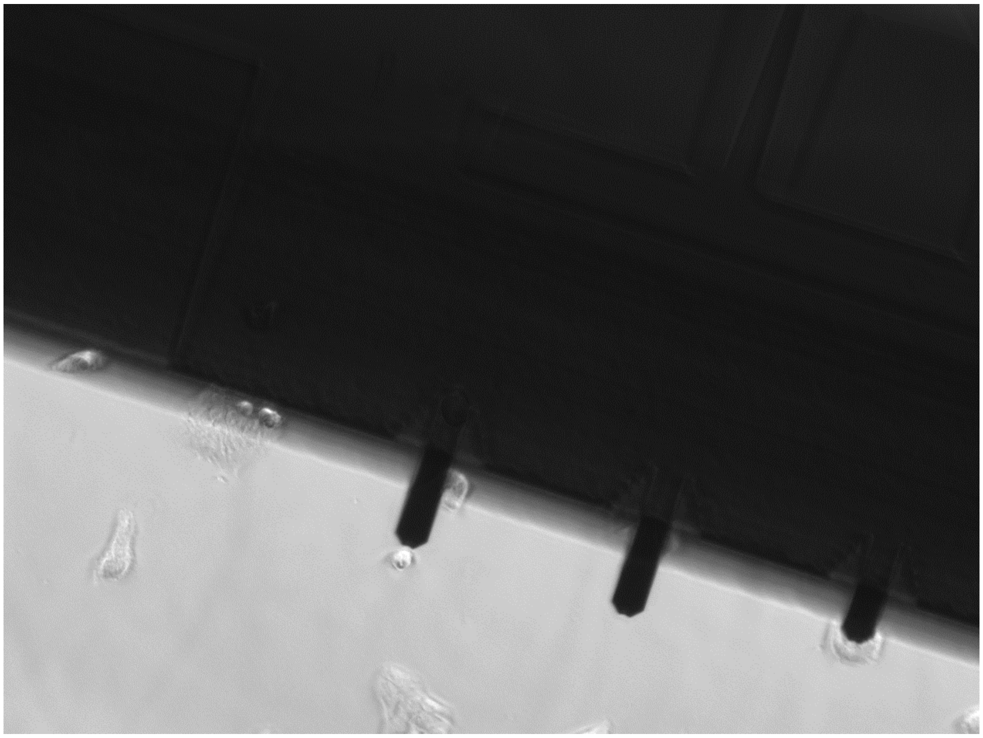

Figure 6.10: image of BPH1$_{scr}$ cell scanned with collagen functionalized cantilever

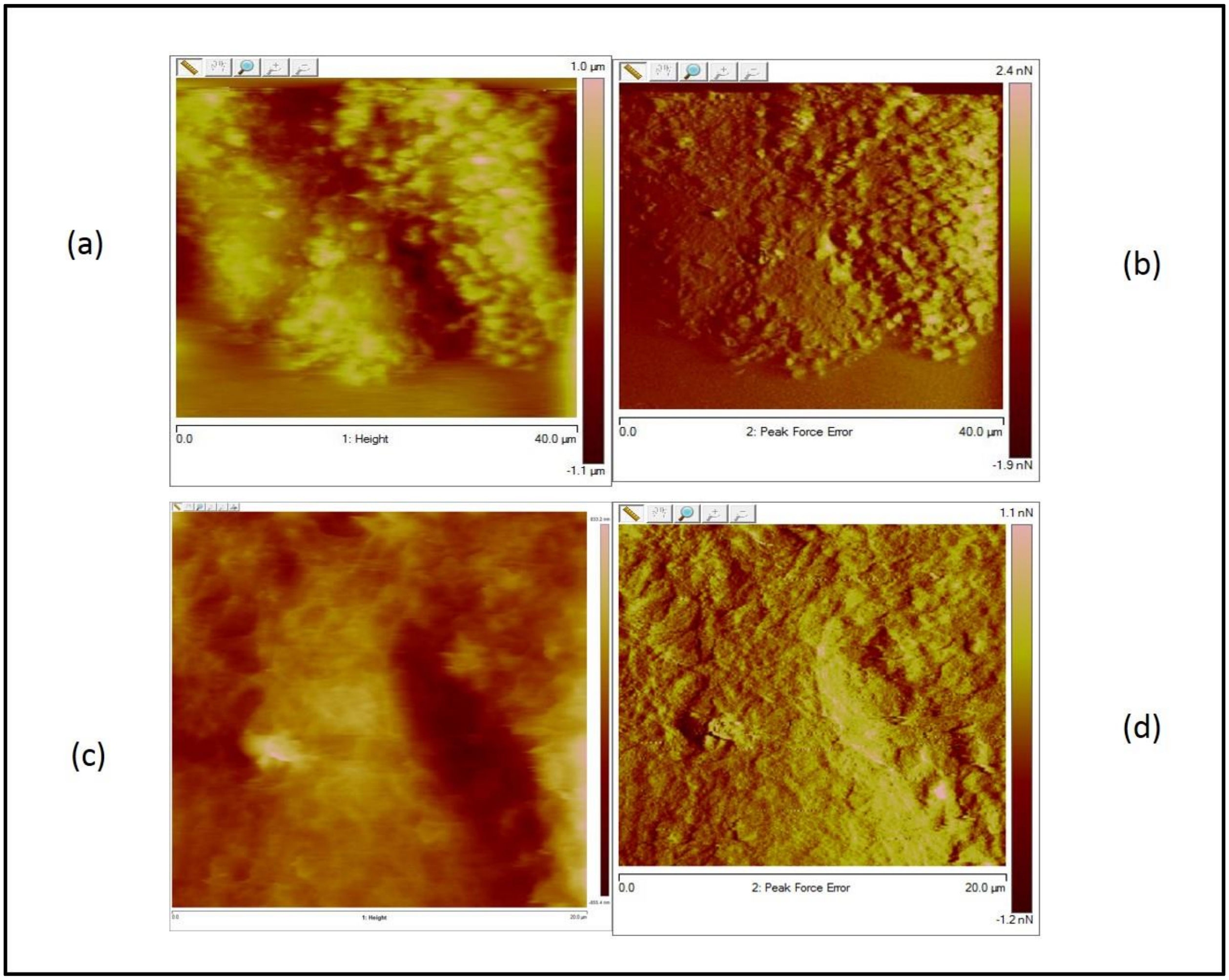

Figure 6.11 (a) and (b) Height image and peak force error image of BPH1$_{scr}$ cell scanned with collagen functionalized OBL-A cantilever with scan size of 40 µm. (c) and (d) Height image and peak force error image of BPH1$_{scr}$ cell scanned with collagen functionalized OBL-A cantilever with scan size of 20 µm.

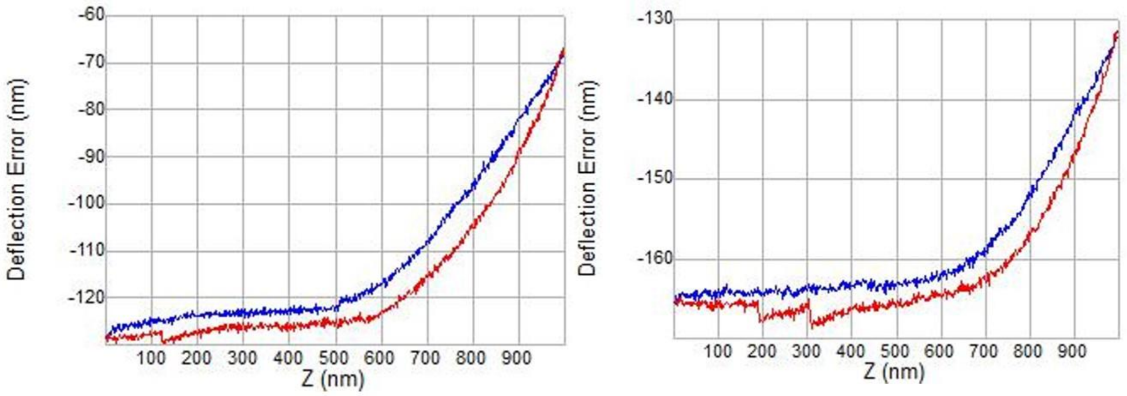

Figure 6.12: (a) Example of a single rupture event due to presence of collagen 1 on the cantilever tip and BPH1$_{scr}$ cell as substrates; (b) Double rupture event due to the binding of collagen to more than one cell surface receptor (the blue line represents the approach curve and red line represents the retract curve)

In our experiments, BPH1$_{scr}$ cells seeded on the petridishes demonstrate different cell morphologies such as round (figure 6.13 (b)) and elongated (figure 6.13 (a) and (c)). In order to determine how the most probable rupture force and binding probability are getting affected by different shapes of BPH1$_{scr}$ cells, we measured force curves on cells of four different shapes. The rupture force data sets of 1000 curves each, were compiled into rupture force histograms and fitted with a Gaussian distribution. The peak of the Gaussian represents the most probable rupture force, and the error bars were determined by dividing the standard deviation by the square root of the total number of measurements. We noticed that the most probable rupture force varies little with the cell shape and binding probability doesn’t vary too much depending on the cell shape. We proceeded by taking the average of the measurements. We also calculated the average binding probability for four different cells and applied the same methods for BPH1$_{shDDR1}$ cells.

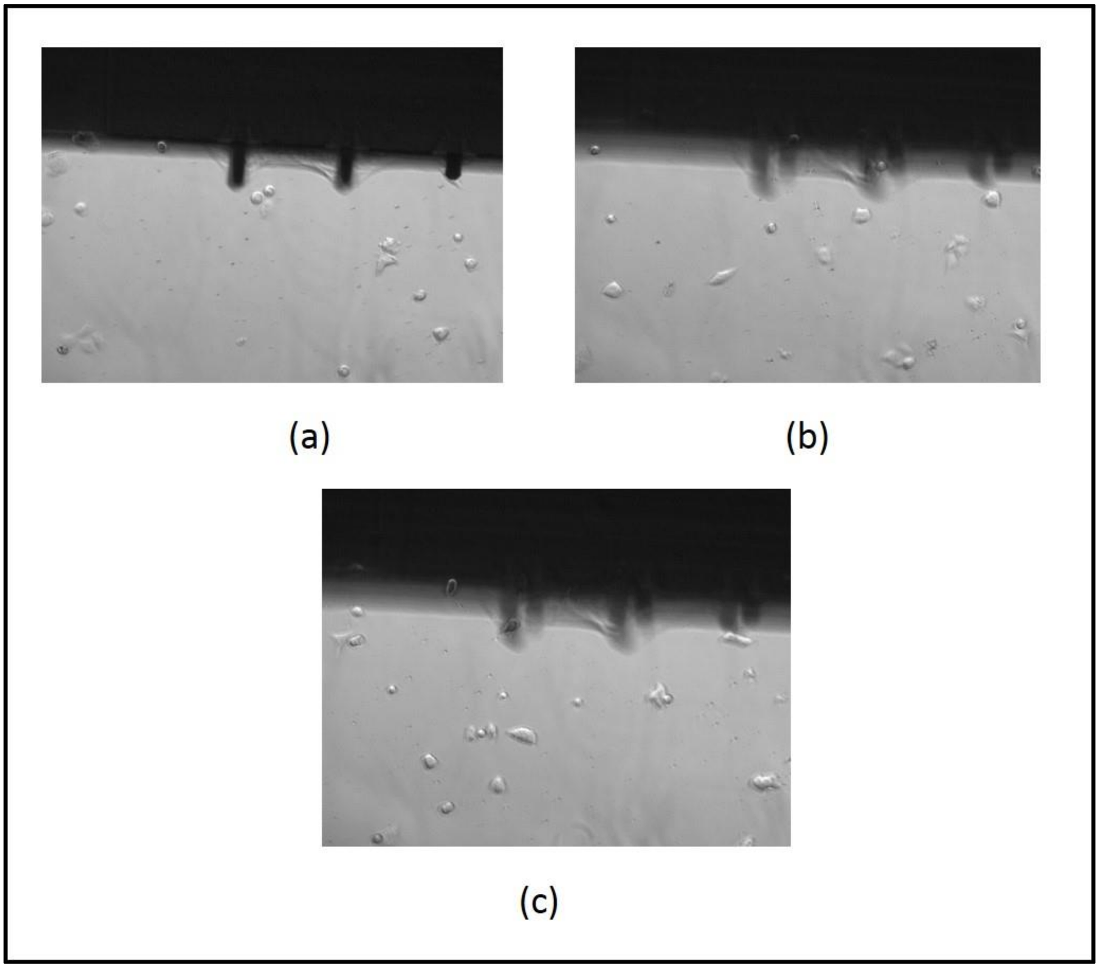

Figure 6.13: (a), (b) and (c) represent collagen functionalized OBL-A cantilever, the right most cantilever in all the images (with nominal stiffness: 0.03 N/m) scanning on top of $BPH1_{scr}$ cells of different shapes

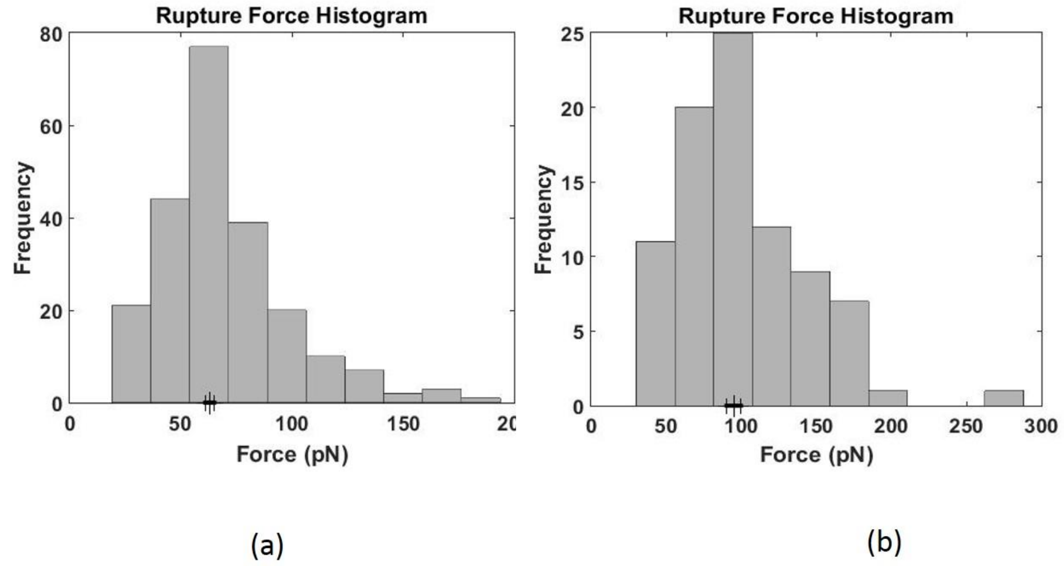

Figure 6.14: (a) represents rupture force histogram performed on the elongated BPH1$_{scr}$ cell (shown in the figure 6.13 (a)) before injecting fibronectin and (b) represents rupture force histogram performed on the elongated BPH1$_{scr}$ cell (shown in the figure 6.13 (a)) after injecting fibronectin

For force measurements, performed on the BPH1$_{scr}$ cells without fibronectin in the flow cell, average binding probability is 0.528 and averaged most probable rupture force is 80.25± 3.38 pN. For force measurements, performed on the BPH1$_{scr}$ cells with fibronectin in the flow cell, average binding probability is 0.167 and averaged most probable rupture force is 83±4.2 pN. We can conclude that injection of fibronectin[111-119] is affecting the total binding probability of collagen and BPH1 cells (which has other collagen binding receptors integrin too) by blocking the interactions between collagen and integrin.

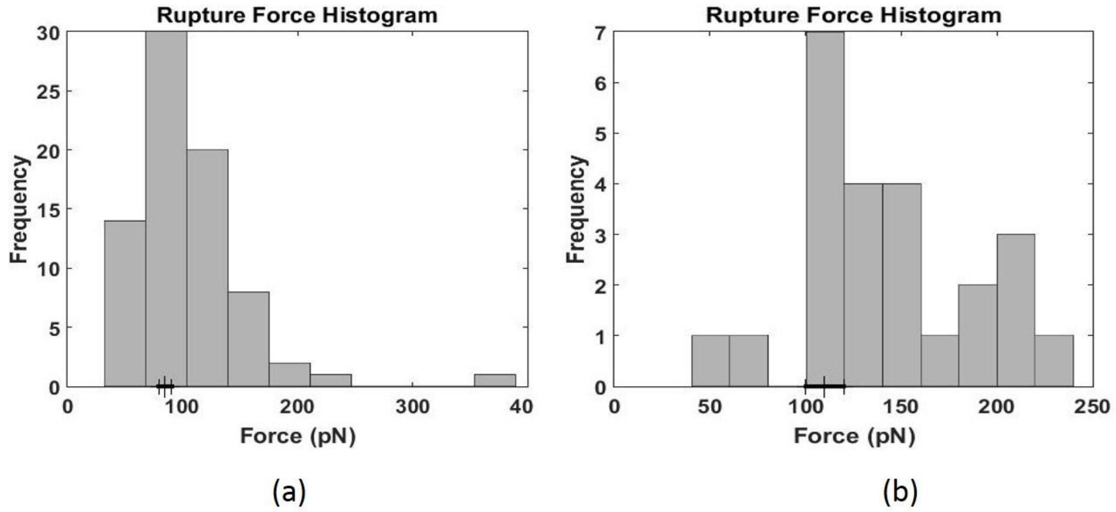

Figure 6.15: (a) represents rupture force histogram performed on the elongated BPH1$_{shDDR1}$cell (shown in the figure 6.13. (a)) before injecting fibronectin and (b) represents rupture force histogram performed on the elongated BPH1$_{shDDR1}$ cell (shown in the figure 6.13. (a)) after injecting fibronectin

For force measurements performed on BPH1 control cells (cells not expressing DDR) without added fibronectin, average binding probability was 0.268 and averaged most probable rupture force was 118±6.3 pN. For force measurements performed on the BPH1 control cells with added fibronectin, average binding probability was 0.0465 and averaged most probable rupture force was 125.7±9.8 pN.

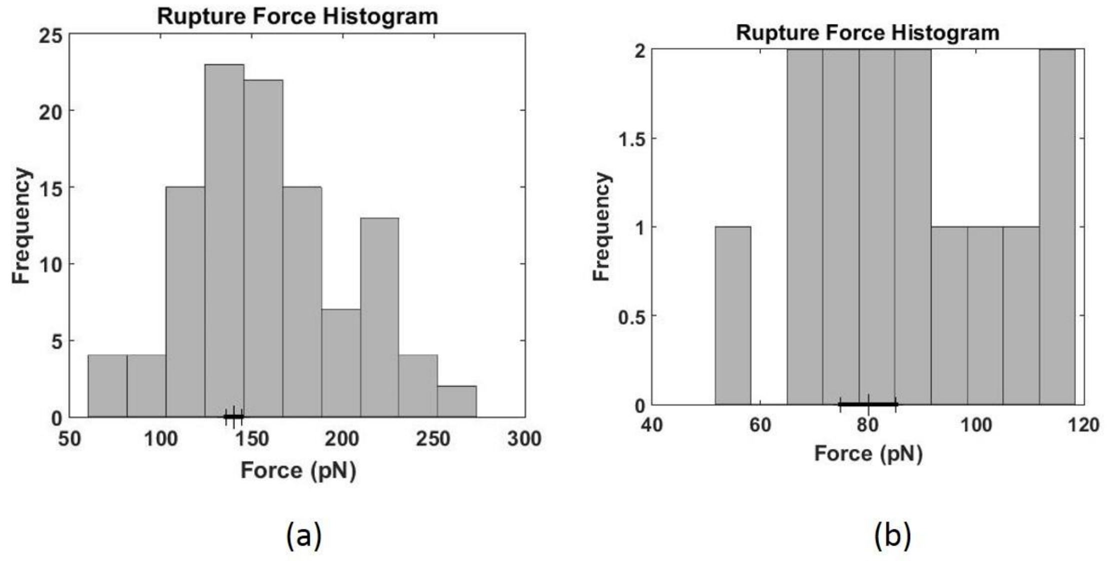

Figure 6.16: (a) and (b) Rupture force histogram for single rupture events, performed on MiaPaCa-2 EV Cells before and after injecting integrin blocking antibody (AII B2 –anti beta integrin 1 blocking antibody with concentration 262 µg/ml) respectively

For force measurements performed on the MiaPaCa-2 EV cells without adding integrin blocking antibody (AII B2 –anti beta integrin 1 blocking antibody with concentration 262 µg/ml), the binding probability was (109+12)/1000= 0.121. For force measurements performed on the MiaPaCa-2 EV cells with added antibody, the binding probability was (14+1)/1000= 15/1000 = 0.015. Most probable rupture force before injecting antibody was 140± 4.2pN. The most probable rupture force after injecting antibody was 80± 5.1 pN.

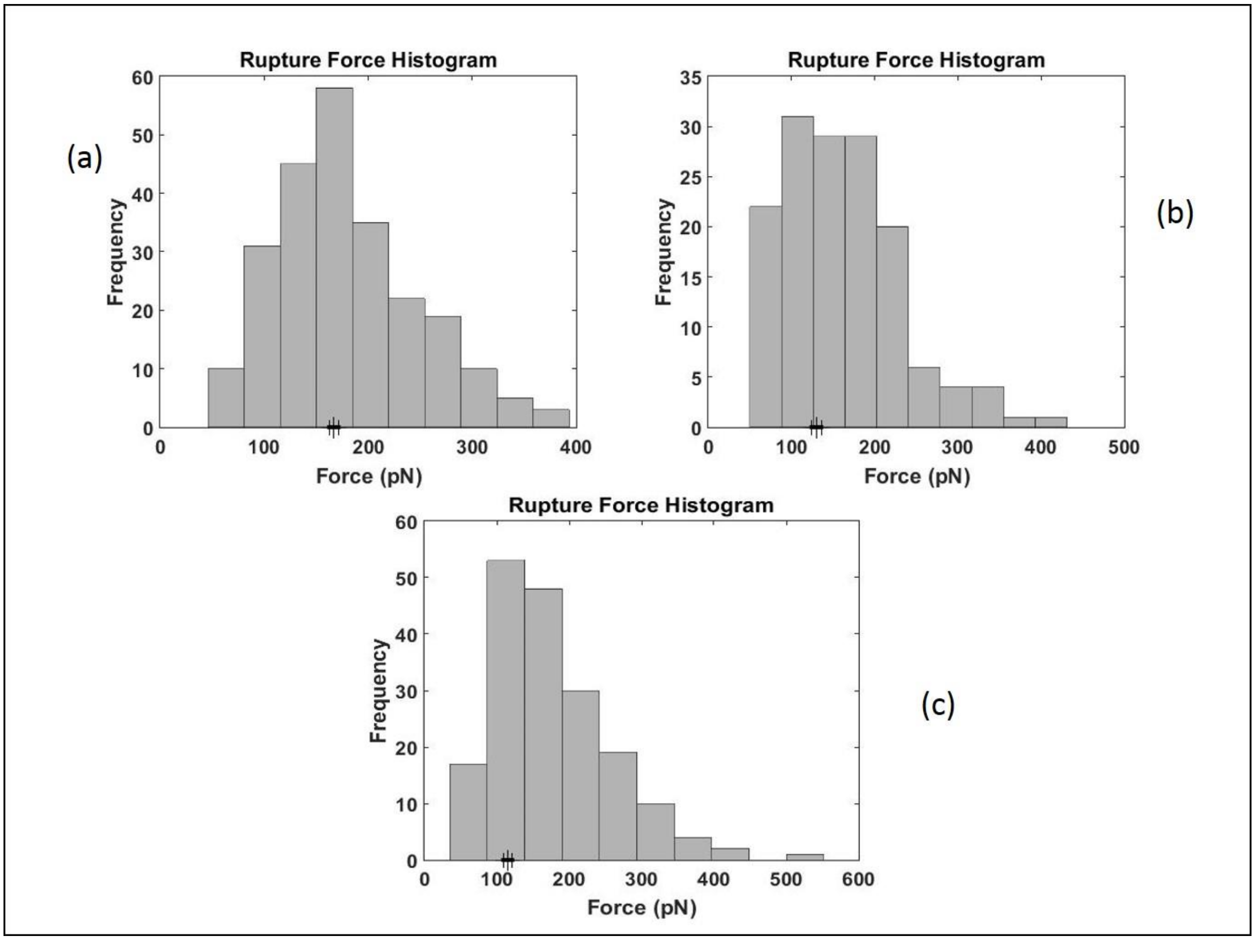

Figure 6.17: (a) represents rupture force histograms for single rupture events, performed on MiaPaCa-2 DDR1b Cells without integrin blocking antibody or fibronectin, (b) represents rupture force histograms for single rupture events, performed on MiaPaCa-2 DDR1b Cells with integrin blocking antibody, (c) represents rupture force histogram for single rupture events, performed on MiaPaCa-2 DDR1b Cells with fibronectin

MiaPaCa-2 cells are human pancreatic epithelial cells and they contain less DDR1 compared to BPH1 cells. For force measurements performed on the MiaPaCa-2 DDR1b cells without added integrin blocking antibody (AII B2 –anti beta integrin 1 blocking antibody with concentration 262 μg/ml) or fibronectin, the binding probability was (280+127)/1000= 0.407 and the most probable rupture force before injecting antibody was 167±4.43 pN. For force measurements performed on the MiaPaCa-2 DDR1b cells with added antibody (AII B2 –anti beta integrin 1 blocking antibody with concentration 262 μg/ml) in the flow cell, the binding probability was (147+57)/1000 = 0.204 and the most probable rupture force after injecting antibody was 130±5.7 pN. For force measurements performed on the MiaPaCa-2 DDR1b cells with added fibronectin, the binding probability was (184+58) /1000 = 0.242 and the most probable rupture force after injecting fibronectin was 115±6.0 pN. It can be concluded from the binding probability results that the injection of fibronectin and integrin β1 blocking antibody brings the binding probability down to half in case of MiPaCa-2 DDR1b cells (integrin receptors are either getting blocked or internalized through endocytosis).

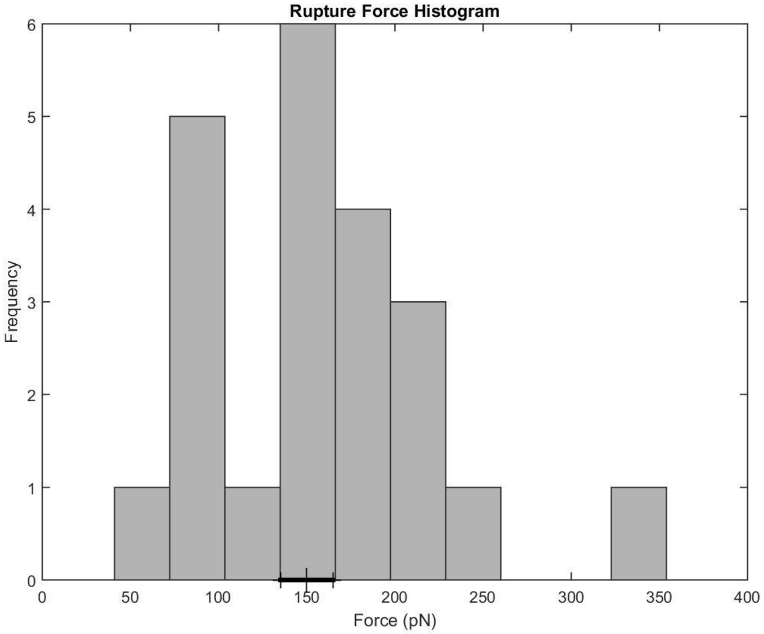

Figure 6.18: Rupture force histogram for single rupture events, performed on MiaPaCa-2 DDR1b R105A cells

For force measurements, performed on MiaPaCa-2 DDR1b R105A cells, and without added integrin blocking antibody (AII B2 –anti beta integrin 1 blocking antibody with concentration 262 μg/ml), the binding probability was 0.139 and the most probable rupture force was 150 ± 14 pN. For force measurements performed on MiaPaCa-2 DDR1b R105A cells, but with added integrin blocking antibody(AII B2 –anti beta integrin 1 blocking antibody with concentration 262 μg/ml), we found a binding probability of 0.

As additional control experiment, we denatured collagen by heating it up at a temperature of 60° Celsius for 30 minutes and then functionalized OBL-A cantilever with this collagen. As denatured collagen is not supposed to bind to DDR, we are not supposed to observe any binding events. We performed 1000 force curves and we did not notice any binding events (data not shown).

6.11.1. Measurement of interaction forces between extracted extracellular DDR and Collagen:

In order to compare the measurement of DDR1-collagen interaction on live cells and interaction between collagen and extracted extracellular DDR, we attached rat tail collagen 1 to clean glass coverslip using the protocol described previously in section 6.9.4.

We attached DDR1-Fc fusion protein to the cantilever tip by first attaching Protein-G to the cantilever using the protocol described as mentioned above. AFM images of collagen-coated substrates with different scan sizes are shown in the figure 6.19.

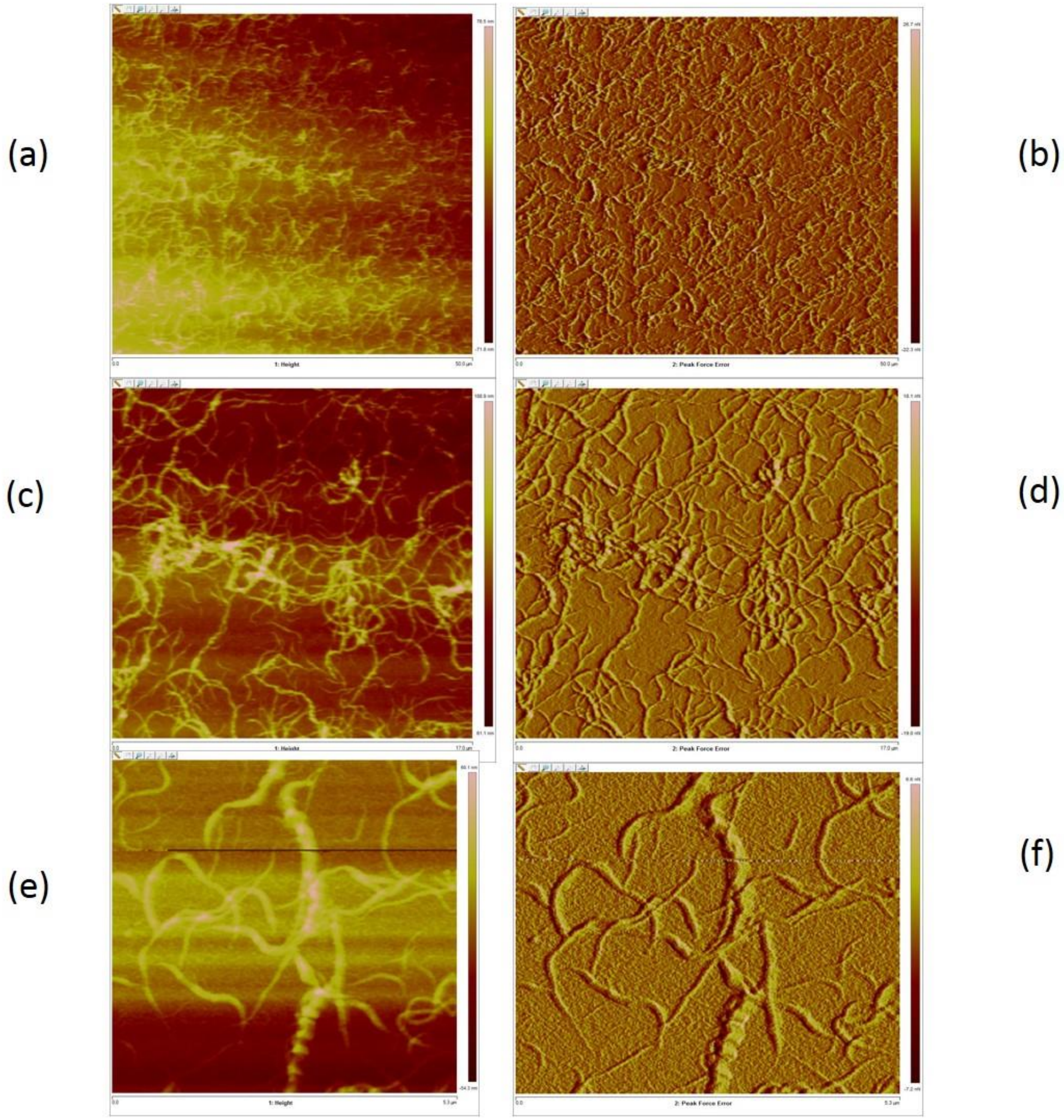

Figure 6.19: (a) and (b) AFM image of Rat tail Collagen 1 attached to glass coverslip with scan size of 50 µm. ; (c) and (d) AFM image of Rat tail Collagen 1 attached to glass coverslip with scan size of 17 µm. : (e) and (f) AFM image of Rat tail Collagen 1 attached to glass coverslip with scan size of 5.3 µm. Scan rates for imaging all of them was 0.5 Hz. (a), (c) and (e) represent the height images and (b), (d) and (f) represent the peak force error images

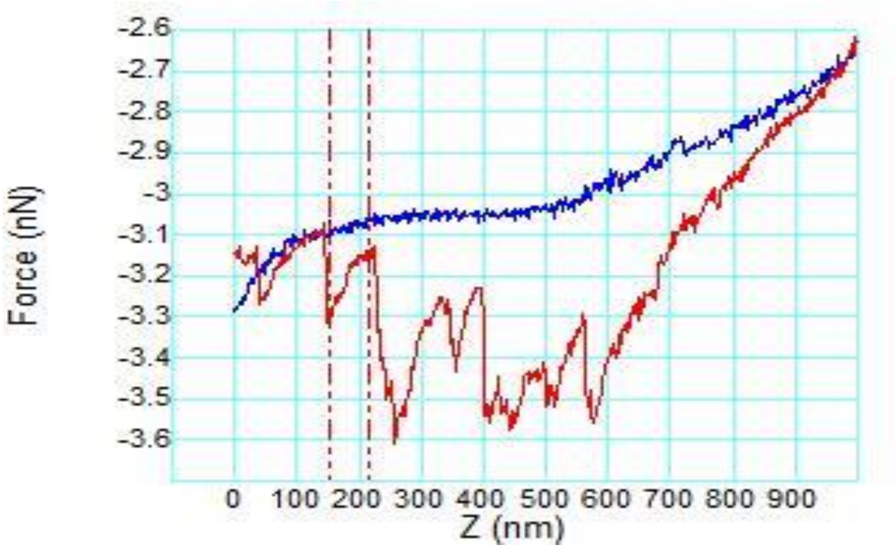

Figure 6.20: Example of force curve due to interaction of extracted extracellular DDR on the cantilever tip and Collagen on the glass coverslip where measured rupture force between the the two dotted red bars is 150 pN.

From the force measurements with collagen functionalized substrate and soluble DDR1-Fc fusion protein functionalized cantilever, we could state that our protocols of functionalization of the cantilever and substrate worked. By functionalizing the cantilever first with protein G (antigen of Fc region of the antibody), we could make sure that DDR1-Fc is attaching in proper conformation to the substrate. As a consequence of the presence of many collagen fibers on the substrate, we could notice a lot of multiple attachments in our force measurements (figure 6.20). We tried to measure the rupture force generated due to a single attachment and estimated the rupture force (141pN), which is in the same range as force measurement of DDR1-collagen interaction on live cells. We can expect less multiple attachment if we can figure out a protocol of functionalization to attach single collagen fiber or fiber fragment to the substrate.

6.11.2. Force measurements on BPH1 cells ($BPH1_{scr}$, parental $BPH1_{shDDR1}$) with DDR1 and integrin blocking antibody:

Follow up experiments were performed on BPH1 cells by using a potential DDR1 blocking antibody (human IgM-DDR1 hu 5E11 with a concentration of 2.07 mg/ml, potential therapeutic drug), provided through a proprietary source. After injecting DDR1 blocking antibody (human IgM-DDR1 hu 5E11 with a concentration of 2.07 mg/ml, potential therapeutic drug) in both DDR1 expressing and control cells ($BPH1_{scr}$ and $BPH1_{shDDR1}$ cells), the binding probability for BPH1 cells expressing DDR1 ($BPH1_{scr}$ cells) was almost halved (went down from 53% to 29%) but it did not affect the control cells (as they were already deprived of DDR1). The total binding probability in the latter case stayed almost same (in the range of 23-27%). It can be concluded that the DDR1 blocking antibody (human IgM-DDR1 hu 5E11 with a concentration of 2.07 mg/ml, potential therapeutic drug) worked and blocked most of the forces caused by DDR1-collagen interactions. After injecting integrin blocking antibody (AII B2 –anti beta integrin 1 blocking antibody with concentration 262 μg/ml) in both kind of cells mentioned above, the binding probability for BPH1 cells expressing DDR1 was almost halved (it went down from 53% to 28%) and binding probability for the control cells went down from 27% to 4%. It can be concluded that integrin blocking antibody (AII B2 –anti beta integrin 1 blocking antibody with concentration 262 μg/ml) works by blocking most of the forces caused by integrin-collagen interactions. The rupture force histograms for all the experiments mentioned above in this paragraph are shown in figure 6.21.

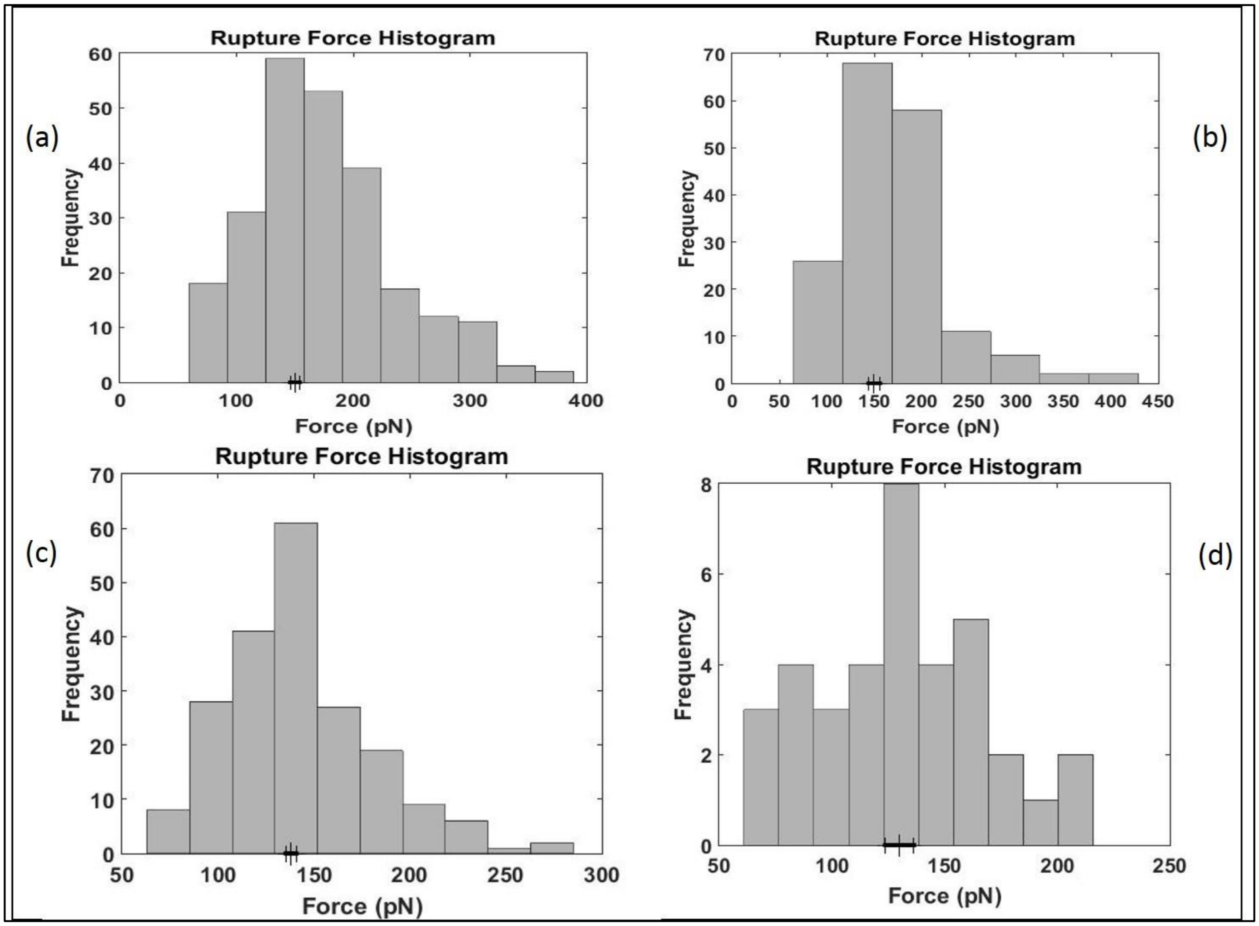

Figure 6.21: (a) Rupture force histogram on $BPH1_{scr}$ cells data with DDR1 blocking antibody with most probable rupture force as 150 pN, (b) Rupture force histogram on $BPH1_{scr}$ cells data with integrin blocking antibody with most probable rupture force as 150 pN; (c) Rupture force histogram on $BPH1_{shDDR1}$ cells data with DDR1 blocking antibody with most probable rupture force as 130 pN and (d) Rupture force histogram on $BPH1_{shDDR1}$ cells data with integrin blocking antibody with most probable rupture force as 138 pN.

Table 6.2: It summarizes binding probability measurements for different types of live cells using different experimental conditions

Experimental conditions	Binding probability for BPH1$_{scr}$ cells	Binding probability for parental BPH1$_{shDDR1}$ cells	Binding probability for MiaPaCa-2 EV cells	Binding probability for MiaPaCa-2 DDR1b cells	Binding probability for MiaPaCa-2 DDR1b R105A cells
Control experiments (Without Fibronectin/antibody)	0.528	0.268	0.121	0.407	0.139
With Fibronectin	0.167	0.0465		0.242	
With integrin blocking antibody	0.278	0.04	0.015	0.204	0
With DDR1 blocking antibody	0.285	0.229			

Table 6.3: It summarizes the most probable rupture force measurements for different types of live cells using different experimental conditions. The mode of the rupture force distribution is taken as the most probable rupture force

Experimental conditions	The most probable rupture force for BPH1$_{scr}$ cells	The most probable rupture force for parental BPH1$_{shDDR1}$ cells	The most probable rupture force for MiaPaCa-2 EV cells	The most probable rupture force for MiaPaCa-2 DDR1b cells	The most probable rupture force for MiaPaCa-2 DDR1b R105A cells
Control experiments (Without Fibronectin/antibody)	80.25± 3.4 pN	118±6.3 pN	140± 4.2pN	167±4.4 pN	150 ± 14 pN
With Fibronectin	83±4.2 pN	125.7±9.8 pN		115±6.0 pN	
With integrin blocking antibody	150pN	130 pN	80± 5.1 pN	130±5.7 pN	0
With DDR1 blocking antibody	150 pN	138 pN			

6.12. Conclusions:

All these experimental results prove the fact that DDR1-collagen interactions can be isolated on live cells by excluding other collagen-receptor interactions. Based on this, we can continue further experiments to learn more about how DDR1 behaves in normal and pathological conditions. Also we could get appropriate values of binding probabilities on different types of cancer cells (BPH1$_{scr}$, parental BPH1$_{shDDR1}$, MiaPaCa-2 EV, MiaPaCa-2 DDR1b, MiaPaCa-2 DDR1b R105A). It can be concluded that the binding probabilities and most probable rupture forces don’t vary too much depending on the different shapes of cells. More detailed studies are needed to conclude about comparison of binding probabilities inside and outside the cell. In case of MiaPaCa-2 cells, we could determine what percentage of the total interaction forces are caused by presence of DDR2 and integrin in the liquid cell.

In order to improve our experimental results, our next steps will be to first perform speed dependent measurements with DDR1 and integrin receptors on cells as substrates and collagen functionalized cantilever in order to determine the dissociation constant, bond length and activation energies. From the literature, we know the affinity values of DDR1-collagen, fibronectin-collagen and collagen-integrin interactions. Once we determine the binding affinity from our experimental results, we can compare them to the previously published affinity values and determine how they are affected by our experimental circumstances. Next, we would like to perform the dosing studies with antibody to show specificity and to notice if there is minimal amount of antibody that can be used to block different interactions. We would also like to vary the density of collagen I on the cantilever and notice how the number of multiple attachments and kinetic parameters vary by varying surface density of collagen on the cantilever tip. Further ideas about future work are described in the last chapter.

CHAPTER 7: CONCLUSION AND FUTURE WORK

7.1. Conclusions:

In our first project, we developed functionalization protocols to join linkers to the surface of the substrate and cantilever. We could validate the protocols and successfully apply them to examine the interaction forces of biotin-avidin model system. We plotted contour length histograms, probability distribution function of rupture forces and ΔR histograms for clearly visible double rupture events for 2%, 4%, 20%, 30%, 50% and 100% biotin samples. Using the molecular weight and bond structure, we determined that the contour length of the of used PEG molecules is approximately 20-25 nm, which matches the expected value based on the molecular weight of the linkers. We did not notice any contour length reading below that in our measurements. Consequently, we considered all the specific single rupture forces corresponding to those contour lengths.

We developed a new approach to examine whether the high rupture forces observed in experimental rupture force histograms are due to multiple attachments or heterogeneous bonding. This new approach involved lowering the density of silane-PEG-biotin on the sample surface, leading to lowering the number of multiple attachments. We mixed mPEG (inactive PEG molecules) and silane PEG biotin (active PEG molecules) at different percentages in order to prepare samples. This procedure reduces the number of measurements in the high force region in the rupture force histogram. Experiments were also performed at various loading rates. We found a dependence of $-v\ln(S(f))$ on loading rates, indicating bond heterogeneity. Our experimental results of binding probabilities, multiple attachment probabilities, zero-distance multiple attachment probabilities and tail percentages confirm the legitimacy of our approach of varying surface density of active sites. We were able to get good force curves as m-PEG in the solution was able to block multiple attachments. The binding probability and zero-distance multi-attachment probability were reduced due to reduction of active biotin PEG molecules on the surface. The difference between the tail percentage and zero-distance multiple attachment probability indicates that the unaccounted high force tail in the rupture force histogram cannot be completely attributed to multiple attachments. We performed Monte-Carlo simulations, which confirmed the importance of possible bond heterogeneity in these types of measurements. They indicate that multiple attachments tend to create a long high force tail in the force distribution, while bond heterogeneity produces a shoulder in the force histograms.

In our second project, we reached several conclusions about DDR1-collagen interactions in live cells and outside live cells: For force measurements performed on the parental $BPH1_{shDDR1}$ cells without added fibronectin or antibody, average binding probability was 0.528. This went down to 0.167 after injecting fibronectin. For $BPH1_{scr}$ cells, the binding is mainly caused by collagen-integrin interactions as these cells don’t express DDR2 and binding probability in this case went down from 0.268 to 0.0465 after injection fibronectin. We can conclude that injecting fibronectin is affecting the total binding probability of collagen and BPH1 cells by blocking collagen-integrin interactions. From the comparison of DDR1-collagen interactions in live cells and the interaction of collagen and extracted extracellular DDR, we concluded that the most probable rupture forces in both cases fall in the same range. As a consequence of the presence of too many collagen fibers on the substrate, we observed a large number multiple attachments in our force measurements. We tried to measure the rupture force generated due to a single attachment and the rupture force (141pN) fell under the same range as force measurement of DDR1-collagen interaction on live cells. We can expect less multiple attachment if we can find a method to attach a single collagen fiber or fiber fragment to the substrate.

After injecting a potential DDR1 blocking antibody (human IgM-DDR1 hu 5E11 with a concentration of 2.07 mg/ml, potential therapeutic drug) in both kind of cells mentioned above, the binding probability for $\mathrm{BPH1_{scr}}$ cells was almost halved but the antibody did not affect the BPH1 control cells. It can be concluded that the DDR1 blocking antibody (human IgM-DDR1 hu 5E11 with a concentration of 2.07 mg/ml, potential therapeutic drug) works and is blocking most of the forces caused by DDR1-collagen interactions. After injecting integrin blocking antibody (AII B2 –anti beta integrin 1 blocking antibody with concentration 262 μg/ml) in both kind of cells mentioned above, the binding probability for $\mathrm{BPH1_{scr}}$ cells was almost halved and binding probability for parental $\mathrm{BPH1_{shDDR1}}$ cells went down to the very low value of 0.04. It can be concluded that integrin blocking antibody (AII B2 –anti beta integrin 1 blocking antibody with concentration 262 μg/ml) works and is blocking most of the forces caused by integrin-collagen interactions.

Adding the bonding probabilities after either adding the integrin-blocking or DDR-blocking antibodies results in the binding probability observed when no blocking agent was used, confirming that we are able to control which receptors bind to collagen in our experiments.

In order to verify these experimental results, we chose three types of MiaPaCa cells (MiaPaCa-2 EV, MiaPaCa-2 DDR1b, MiaPaCa-2 DDR1b R105A) and performed similar control experiments without added antibody or fibronectin. For MiaPaCa-2 EV cells, binding probability went down almost 8 times (from 12% to 1.5%) after injection of β1 integrin blocking antibody (AII B2 –anti beta integrin 1 blocking antibody with concentration 262 μg/ml). For MiaPaCa-2 DDR1b cells, binding probability was halved after injecting either β1 integrin blocking antibody

(AII B2 –anti beta integrin 1 blocking antibody with concentration 262 μg/ml) or fibronectin. The binding probability for initial control experiment for MiaPaCa-2 DDR1b cells (41%) was low compared to BPH1 cells (53%) as MiaPaCa cells contain less DDR1 compared to BPH1 cells. For MiaPaCa-2 DDR1b R105A cells, the binding probability was around 13.9% before injecting integrin and went down to 0 after injecting integrin blocking antibody (AII B2 –anti beta integrin 1 blocking antibody with concentration 262 μg/ml). It can be concluded that for all three types of MiaPaCa cells, the most probable rupture forces generally decreased after injecting both fibronectin and antibody. Also, we can conclude that injection of both fibronectin and integrin blocking antibody (AII B2 –anti beta integrin 1 blocking antibody with concentration 262 μg/ml) blocked forces caused by the integrin-collagen interactions.

In conclusion, we were successful in developing protocols that will allow us to perform single-molecule measurements on specific receptors on live cells by using proper blocking procedures.

7.2. Directions for future work:

We tried to determine if DDR1-collagen interaction can be isolated and if they can be used for further studies to explore more information about the behavior of DDR1 on cell-collagen interface and we were successful in that attempt. In order to combine fluorescence and AFM in future experiments on live cells, DDR1 or antibodies will be labeled. In our experiments, DDR1 on cells can be tagged with GFP. Using such cells, we can first determine the location of individual receptors on the cell surface and then perform imaging and force measurements with them with AFM and MIRO software to increase specificity of the measurement and make sure that each collagen molecule is attaching to each single DDR receptor.

We can also label some agents (like Notch-1, N-cadherin) in the downstream signaling pathways regulated by DDR1s and notice their states of activation when we bring collagen functionalized cantilever near the surface. Previous researches have shown that binding affinity of DDR1-collagen interactions is regulated by fibrillar collagen and Agarwal et al[94] has also shown that DDR1 attach with overlapping monomeric units of collagen. It was also shown that the other receptors of collagen regulate and modify fibrillogenesis (development procedure of thinner fibrils in collagen fibers) of type I collagen. We would like to explore the effect DDR1-collagen binding collagen on fibrillogenesis by imaging collagen (attached to the substrate initially) with regular intervals of time after seeding BPH1 cells or similar cells on it under different conditions and repeating the same experiment after injecting antibodies.

We would like to find a better method to measure interactions between DDR-Fc and collagen by decreasing the number of multiple attachments. For example, we can either attach single fiber of collagen or a collagen peptide fragment to the cantilever by browsing the surface of collagen functionalized substrate with non-functionalized cantilever and picking up single collagen fiber on the cantilever tip or we can try to attach soluble DDR1-Fc fusion protein directly to a properly selected substrate.

We will work on developing a method which better deals with cell membrane deformation while performing single molecule force measurements on live cells. As Scheffer et al.[44] and Discher et al.[43] described in their publications, the analysis for an actual deformed cell shape is complex (not only because of the deformation shape, but also because of the influence of the cytoskeleton), but the upshot is that the force of deformation of the cell membrane is either linear (according to Scheffer) or somewhat polynomial (according to Discher). This force can be quite well fitted by a parabolic equation for the linkers that we showed in our previous publication.

Therefore, deformation modifies the force profile. Since we measure the force profile, we can fit each profile individually, extract the fitting parameters (alpha, *kt* and *kapp*), average them and then extract our kinetic parameters the same way as done in our previous paper. Our assumptions for this method is that the cell membrane is only undergoing relatively small deformations before the rupture of the bond and our measurement is not long lasting enough so that the cell has no time to react, i.e. the force is only dependent on the physical properties of the cell membrane, not on any reorganization of the cell cytoskeleton. We will develop a more detailed model for this and continue to develop a proper analysis software for this purpose.

All of our DDR1-collagen interaction force measurements were performed with a pull speed of 2 μm/s. We would like to perform speed-dependent force measurements of DDR1-collagen interactions to derive important kinetic parameters like dissociation constants, bond lengths and activation energies. We would also like to vary the density of collagen on cantilever and perform force measurements with that cantilever in order to observe if the interaction force measurements and the binding probabilities are affected by the different density of collagen and also if there is a minimal value of collagen density below which collagen doesn’t bind to DDR1 and integrins.

We would like to explore effects of linkers on forces using various kinds of PEG linkers of different lengths as usually we use linkers of longer length (20-25 nm) to distinguish specific and nonspecific interactions. We would like to see how a smaller or larger contour length of linkers affect the force measurements and kinetic parameters (off-rate, on-rate, distance to transition state, activation energy).

So far, it can be noticed from previous studies that dissociation parameters in bimolecular reactions are well investigated and explored compared to association kinetics. The initial approaches of determining association constants by Friddle et al.[120] and Hinterdorfer et al. [57] had several difficulties in experimental scenarios as they required accurate value of grafting density. Also, there was no way of distinguishing specific and nonspecific binding events. One of approaches assumed the probing of tethered ligand within a constant volume. In order to develop a proper method to determine association kinetics, Akhremitchev[7] proposed an approach in which probability of binding and dissociation are measured at the same time. In this approach, he used polymeric tether dynamics models to figure out how energy for association and binding probability are related.

The binding probability of the molecules increase if the probability of molecules encountering other molecules increases. The ligand on tip or substrate can bind to receptor on the substrate or tip during approach or retract or dwelling of the probe close to the surface. The tethers have to be extended to join the receptor and cantilever. Using low grafting density, this approach first found an expression for probability to form single bond in terms of rate of the binding of a receptor-ligand system (in terms of distance), the end-to-end separating distance of the polymeric tether, the time for oscillatory motion of the probe, dwell time, receptor displacement from end of the tether to the substrate and maximum probe distance. If the grafting density is low, the binding probability can be easy calculated by integrating the expression of probability to form one bond. In case of a fixed cantilever and receptor, the association rate is dependent on the probe position and was derived using expressions for the free energy of the tether which is fully stretched. We will explore this method to determine association kinetics and therefore determine affinities. We will perform measurements at different dwell times to validate the approach and get better estimates of the association rates.

REFERENCES

1. M. R. Sierks and B. Svensson, Biochemistry **35** (6), 1865-1871 (1996).

2. E. L. Florin, V. T. Moy and H. E. Gaub, Science **264** (5157), 415-417 (1994).

3. P. Hinterdorfer, W. Baumgartner, H. J. Gruber, K. Schilcher and H. Schindler, Proceedings of the National Academy of Sciences of the United States of America **93** (8), 3477-3481 (1996).

4. E. Evans, Biophysical chemistry **82** (2-3), 83-97 (1999).

5. E. Evans and K. Ritchie, Biophysical journal **72** (4), 1541-1555 (1997).

6. E. Y. MAYYAS, (2010).

7. S. Guo, N. Lad, C. Ray and B. B. Akhremitchev, Biophysical journal **96** (8), 3412-3422 (2009).

8. S. Guo, C. Ray, A. Kirkpatrick, N. Lad and B. B. Akhremitchev, Biophysical journal **95** (8), 3964-3976 (2008).

9. M. Raible, M. Evstigneev, F. W. Bartels, R. Eckel, M. Nguyen-Duong, R. Merkel, R. Ros, D. Anselmetti and P. Reimann, Biophysical journal **90** (11), 3851-3864 (2006).

10. H. L. Fu, R. R. Valiathan, R. Arkwright, A. Sohail, C. Mihai, M. Kumarasiri, K. V. Mahasenan, S. Mobashery, P. Huang, G. Agarwal and R. Fridman, The Journal of biological chemistry **288** (11), 7430-7437 (2013).

11. R. R. Valiathan, M. Marco, B. Leitinger, C. G. Kleer and R. Fridman, Cancer metastasis reviews **31** (1-2), 295-321 (2012).

12. Y. C. Yeh, H. H. Lin and M. J. Tang, American journal of physiology. Cell physiology **303** (12), C1207-1217 (2012).

13. A. A. Deniz, S. Mukhopadhyay and E. A. Lemke, Journal of the Royal Society, Interface / the Royal Society **5** (18), 15-45 (2008).

14. K. C. Neuman and A. Nagy, Nature methods **5** (6), 491-505 (2008).

15. R. Roy, S. Hohng and T. Ha, Nature methods **5** (6), 507-516 (2008).

16. S. A. Vickery and R. C. Dunn, Journal of microscopy **202** (Pt 2), 408-412 (2001).

17. W. J. Greenleaf, M. T. Woodside and S. M. Block, Annual review of biophysics and biomolecular structure **36**, 171-190 (2007).

18. N. A. Burnham, D. D. Dominguez, R. L. Mowery and R. J. Colton, Physical review letters **64** (16), 1931-1934 (1990).

19. H. Mueller, H. J. Butt and E. Bamberg, Biophysical journal **76** (2), 1072-1079 (1999).

20. T. Yang, X. Li, Y. Chen, D. W. Lee and G. Zuo, The Analyst **136** (24), 5261-5269 (2011).

21. S. J. Eppell, B. N. Smith, H. Kahn and R. Ballarini, Journal of the Royal Society, Interface / the Royal Society **3** (6), 117-121 (2006).

22. S. J. Eppell, S. R. Simmons, R. M. Albrecht and R. E. Marchant, Biophysical journal **68** (2), 671-680 (1995).

23. B. A. Eppell, A. M. Newell and E. J. Brown, Journal of immunology **143** (12), 4141-4145 (1989).

24. Bruker. Corporation, (2009,2010,2011).

25. Bruker. Corporation, **Application Note #128** (2012).

26. Bruker. Corporation, (2009,2010,2011).

27. Bruker. Corporation, (2009,2011).

28. M. S. Kellermayer, Methods in molecular biology **736**, 439-456 (2011).

29. J. E. Shaw, A. Slade and C. M. Yip, Journal of the American Chemical Society **125** (39), 11838-11839 (2003).

30. J. Yuan, C. Hao, M. Chen, P. Berini and S. Zou, Langmuir : the ACS journal of surfaces and colloids **29** (1), 221-227 (2013).

31. A. B. Mathur, G. A. Truskey and W. M. Reichert, Biophysical journal **78** (4), 1725-1735 (2000).

32. C. M. Franz and P. H. Puech, Cellular and Molecular Bioengineering **1** (4), 289-300 (2008).

33. Q. S. Li, G. Y. Lee, C. N. Ong and C. T. Lim, Biochemical and biophysical research communications **374** (4), 609-613 (2008).

34. E. Betzig, G. H. Patterson, R. Sougrat, O. W. Lindwasser, S. Olenych, J. S. Bonifacino, M. W. Davidson, J. Lippincott-Schwartz and H. F. Hess, Science **313** (5793), 1642-1645 (2006).

35. M. J. Rust, M. Bates and X. Zhuang, Nature methods **3** (10), 793-795 (2006).

36. C. M. Franz, A. Taubenberger, P. H. Puech and D. J. Muller, Science's STKE : signal transduction knowledge environment **2007** (406), pl5 (2007).

37. C. Lagenaur and V. Lemmon, Proceedings of the National Academy of Sciences of the United States of America **84** (21), 7753-7757 (1987).

38. K. E. Sussman, H. B. Pollard, J. W. Leitner, R. Nesher, J. Adler and E. Cerasi, Transactions of the Association of American Physicians **95**, 299-309 (1982).

39. J. Helenius, C. P. Heisenberg, H. E. Gaub and D. J. Muller, Journal of cell science **121** (11), 1785-1791 (2008).

40. M. Benoit and H. E. Gaub, Cells, tissues, organs **172** (3), 174-189 (2002).

41. A. Taubenberger, D. A. Cisneros, J. Friedrichs, P. H. Puech, D. J. Muller and C. M. Franz, Molecular biology of the cell **18** (5), 1634-1644 (2007).

42. G. I. Bell, Science **200** (4342), 618-627 (1978).

43. S. Sen, S. Subramanian and D. E. Discher, Biophysical journal **89** (5), 3203-3213 (2005).

44. L. Scheffer, A. Bitler, E. Ben-Jacob and R. Korenstein, European biophysics journal : EBJ **30** (2), 83-90 (2001).

45. E. Mayyas, M. Bernardo, L. Runyan, A. Sohail, V. Subba-Rao, M. Pantea, R. Fridman and P. M. Hoffmann, Biomacromolecules **11** (12), 3352-3358 (2010).

46. A. Fuhrmann, D. Anselmetti, R. Ros, S. Getfert and P. Reimann, Physical review. E, Statistical, nonlinear, and soft matter physics **77** (3 Pt 1), 031912 (2008).

47. C. Ray, J. R. Brown and B. B. Akhremitchev, The journal of physical chemistry. B **111** (8), 1963-1974 (2007).

48. C. Ray, S. Guo, J. Brown, N. Li and B. B. Akhremitchev, Langmuir : the ACS journal of surfaces and colloids **26** (14), 11951-11957 (2010).

49. C. S. Guo, M. A. Van Hove, R. Q. Zhang and C. Minot, Langmuir : the ACS journal of surfaces and colloids **26** (21), 16271-16277 (2010).

50. F. Hanke and H. J. Kreuzer, Physical review. E, Statistical, nonlinear, and soft matter physics **74** (3 Pt 1), 031909 (2006).

51. O. Karacsony and B. B. Akhremitchev, Langmuir : the ACS journal of surfaces and colloids **27** (18), 11287-11291 (2011).

52. N. Li, S. Guo and B. B. Akhremitchev, Chemphyschem : a European journal of chemical physics and physical chemistry **11** (10), 2096-2098 (2010).

53. N. de Souza, Nature methods **9** (9), 873-877 (2012).

54. O. K. Dudko, Proceedings of the National Academy of Sciences of the United States of America **106** (22), 8795-8796 (2009).

55. O. K. Dudko, G. Hummer and A. Szabo, Physical review letters **96** (10), 108101 (2006).

56. O. K. Dudko, G. Hummer and A. Szabo, Proceedings of the National Academy of Sciences of the United States of America **105** (41), 15755-15760 (2008).

57. P. Hinterdorfer and Y. F. Dufrene, Nature methods **3** (5), 347-355 (2006).

58. A. Noy, Current opinion in chemical biology **15** (5), 710-718 (2011).

59. A. S. Anderson, A. M. Dattelbaum, G. A. Montano, D. N. Price, J. G. Schmidt, J. S. Martinez, W. K. Grace, K. M. Grace and B. I. Swanson, Langmuir : the ACS journal of surfaces and colloids **24** (5), 2240-2247 (2008).

60. N. W. Moore and T. L. Kuhl, Biophysical journal **91** (5), 1675-1687 (2006).

61. S. Kim, M. Ouyang, J. Jeong, C. Shen and X. Zhang, The annals of applied statistics **8** (2), 1209-1231 (2014).

62. J. P. Wang, B. G. Lindsay, L. Cui, P. K. Wall, J. Marion, J. Zhang and C. W. dePamphilis, BMC bioinformatics **6**, 300 (2005).

63. C. L. Lewin B, Lingappa V, Plopper G). Sudbury, (2007).

64. B. A. Lodish H, Matsudaira P, Kaiser CA, Krieger M, Scott MP, Zipursky SL, Darnell J.

65. M. Abedin and N. King, Trends in cell biology **20** (12), 734-742 (2010).

66. C. Brownlee, Current opinion in plant biology **5** (5), 396-401 (2002).

67. G. A. Di Lullo, S. M. Sweeney, J. Korkko, L. Ala-Kokko and J. D. San Antonio, The Journal of biological chemistry **277** (6), 4223-4231 (2002).

68. G. Karsenty and R. W. Park, International reviews of immunology **12** (2-4), 177-185 (1995).

69. B. Leitinger, Annual review of cell and developmental biology **27**, 265-290 (2011).

70. S. Strasser, A. Zink, M. Janko, W. M. Heckl and S. Thalhammer, Biochemical and biophysical research communications **354** (1), 27-32 (2007).

71. M. P. Wenger, L. Bozec, M. A. Horton and P. Mesquida, Biophysical journal **93** (4), 1255-1263 (2007).

72. P. Cuatrecasas, Annual review of biochemistry **43** (0), 169-214 (1974).

73. M. H. Akabas, D. A. Stauffer, M. Xu and A. Karlin, Science **258** (5080), 307-310 (1992).

74. F. M. Dautzenberg and R. L. Hauger, Trends in pharmacological sciences **23** (2), 71-77 (2002).

75. A. G. Gilman, Annual review of biochemistry **56**, 615-649 (1987).

76. N. King, C. T. Hittinger and S. B. Carroll, Science **301** (5631), 361-363 (2003).

77. S. Riviere, L. Challet, D. Fluegge, M. Spehr and I. Rodriguez, Nature **459** (7246), 574-577 (2009).

78. A. Ullrich and J. Schlessinger, Cell **61** (2), 203-212 (1990).

79. D. R. Robinson, Y. M. Wu and S. F. Lin, Oncogene **19** (49), 5548-5557 (2000).

80. J. S. Lin, C. W. Lu, C. J. Huang, P. F. Wu, D. Robinson, H. J. Kung, C. W. Chi, C. W. Wu, W. K. Yang, J. J. Whang-Peng and W. C. Lin, Journal of biomedical science **5** (2), 101-110 (1998).

81. K. Komori, K. A. Robinson, N. E. Block, R. C. Roberts and M. G. Buse, Endocrinology **131** (3), 1288-1296 (1992).

82. N. Nair, R. J. Davis and H. L. Robinson, Molecular and cellular biology **12** (5), 2010-2016 (1992).

83. R. O. Hynes, Cell **110** (6), 673-687 (2002).

84. S. H. Kim, J. Turnbull and S. Guimond, The Journal of endocrinology **209** (2), 139-151 (2011).

85. S. J. Attwood, A. M. Simpson, S. W. Hamaia, D. Bihan, D. Roy, R. W. Farndale and M. E. Welland, International journal of molecular sciences **14** (2), 2832-2845 (2013).

86. H. C. Siebert, M. Burg-Roderfeld, T. Eckert, S. Stotzel, U. Kirch, T. Diercks, M. J. Humphries, M. Frank, R. Wechselberger, E. Tajkhorshid and S. Oesser, Protein & cell **1** (4), 393-405 (2010).

87. J. E. Olberding, M. D. Thouless, E. M. Arruda and K. Garikipati, PloS one **5** (8), e12043 (2010).

88. J. W. Smith, Current opinion in investigational drugs **4** (6), 741-745 (2003).

89. W. S. Carbonell, M. DeLay, A. Jahangiri, C. C. Park and M. K. Aghi, Cancer research **73** (10), 3145-3154 (2013).

90. H. L. Goel, M. Breen, J. Zhang, I. Das, S. Aznavoorian-Cheshire, N. M. Greenberg, A. Elgavish and L. R. Languino, Cancer research **65** (15), 6692-6700 (2005).

91. W. H. Goldmann, A. Bremer, M. Haner, U. Aebi and G. Isenberg, Journal of structural biology **112** (1), 3-10 (1994).

92. J. Gullingsrud and K. Schulten, Biophysical journal **86** (6), 3496-3509 (2004).

93. D. S. Harburger, M. Bouaouina and D. A. Calderwood, The Journal of biological chemistry **284** (17), 11485-11497 (2009).

94. G. Agarwal, C. Mihai and D. F. Iscru, Journal of molecular biology **367** (2), 443-455 (2007).

95. C. Mihai, M. Chotani, T. S. Elton and G. Agarwal, Journal of molecular biology **385** (2), 432-445 (2009).

96. L. V. Wain, G. C. Verwoert, Nature genetics **43** (10), 1005-1011 (2011).

97. H. J. Yu, A. T. Lin, S. S. Yang, K. H. Tsui, H. C. Wu, C. L. Cheng, H. L. Cheng, T. T. Wu and P. H. Chiang, BJU international **108** (11), 1843-1848 (2011).

98. Q. Wu, Y. Zhou, L. Chen, J. Shi, C. Y. Wang, L. Miao, H. Klocker, I. Park, C. Lee and J. Zhang, The Journal of endocrinology **195** (1), 89-94 (2007).

99. H. Ahsan, S. Reagan-Shaw, J. Breur and N. Ahmad, Cancer letters **249** (2), 198-208 (2007).

100. J. H. Shieh, J. K. Cini, M. C. Wu and A. A. Yunis, Archives of biochemistry and biophysics **253** (1), 205-213 (1987).

101. G. Fountzilas, H. Gratzner, L. O. Lim and A. A. Yunis, Journal of the National Cancer Institute **76** (1), 37-43 (1986).

102. G. Fountzilas, L. O. Lim and A. A. Yunis, In vitro **20** (9), 685-691 (1984).

103. A. A. Yunis, G. K. Arimura and D. J. Russin, International journal of cancer. Journal international du cancer **19** (1), 128-135 (1977).

104. G. E. Moore, R. E. Gerner and H. A. Franklin, Jama **199** (8), 519-524 (1967).

105. S. C. Baicu and M. J. Taylor, Cryobiology **45** (1), 33-48 (2002).

106. D. J. Mellor and N. G. Gregory, New Zealand veterinary journal **51** (1), 2-13 (2003).

107. W. W. Cleland, Biochemistry **3**, 480-482 (1964).

108. R. J. Towers, P. K. Fagan, S. R. Talay, B. J. Currie, K. S. Sriprakash, M. J. Walker and G. S. Chhatwal, Journal of clinical microbiology **41** (12), 5398-5406 (2003).

109. U. Sjobring, L. Bjorck and W. Kastern, The Journal of biological chemistry **266** (1), 399-405 (1991).

110. A. Olsson, M. Eliasson, B. Guss, B. Nilsson, U. Hellman, M. Lindberg and M. Uhlen, European journal of biochemistry / FEBS **168** (2), 319-324 (1987).

111. M. J. Elices, L. A. Urry and M. E. Hemler, The Journal of cell biology **112** (1), 169-181 (1991).

112. S. Huang, J. Varani and S. Chakrabarty, Journal of cellular physiology **161** (3), 470-482 (1994).

113. W. Huang, R. Chiquet-Ehrismann, J. V. Moyano, A. Garcia-Pardo and G. Orend, Cancer research **61** (23), 8586-8594 (2001).

114. X. Z. Huang, A. Chen, M. Agrez and D. Sheppard, American journal of respiratory cell and molecular biology **13** (2), 245-251 (1995).

115. A. Koide, C. W. Bailey, X. Huang and S. Koide, Journal of molecular biology **284** (4), 1141-1151 (1998).

116. R. Pacifici, C. Basilico, J. Roman, M. M. Zutter, S. A. Santoro and R. McCracken, The Journal of clinical investigation **89** (1), 61-67 (1992).

117. N. Tang, X. Wang, T. Huang, Y. Wu and Y. Chen, Experimental dermatology **23** (7), 512-513 (2014).

118. Q. L. Zou, J. R. Guo, X. F. Chen, X. L. Chen, P. Chen, M. J. Huang and Y. Z. Chen, Zhonghua yi xue za zhi **89** (48), 3425-3429 (2009).

119. Q. L. Zou, J. R. Guo, X. F. Chen, M. J. Huang, Y. Wu and Y. Z. Chen, Zhongguo shi yan xue ye xue za zhi / Zhongguo bing li sheng li xue hui = Journal of experimental hematology / Chinese Association of Pathophysiology **18** (3), 698-703 (2010).

120. R. J. Buono, T. N. Ferraro, M. J. O'Connor, M. R. Sperling, M. Abbey, E. Finanger, F. Lohoff, N. Mulholland and W. H. Berrettini, American journal of medical genetics **96** (1), 79-83 (2000).

ABSTRACT

INTERACTION FORCES AND REACTION KINETICS OF LIGAND-CELL RECEPTOR SYSTEMS USING ATOMIC FORCE MICROSCOPY

by

ANWESHA SARKAR

December 2015

Advisor: Dr. Peter M. Hoffmann

Major: Physics

Degree: Doctor of Philosophy

Atomic Force Microscopy (AFM) provides superior imaging resolution and the ability to measure forces at the nanoscale. It is an important tool for studying a wide range of bio-molecular samples from proteins, DNA to living cells. We developed AFM measurement procedures to measure protein interactions on live cells at the single molecular level. These measurements can be interpreted by using proper statistical approaches and can yield important parameters about ligand-receptor interactions on live cells. However, the standard theory for analyzing rupture force data does not fit the experimental rupture force histograms. Most of the experimental measurements of rupture force data generate a probability distribution function (pdf) with a high force tail. We show that this unexpected high force tail can be attributed to multiple attachments and heterogeneous bonding by studying a model system, biotin-avidin. We have applied our methodology to the medically relevant system of discoidin domain receptors (DDR) on live cells and their interaction with their ligand, collagen.

AUTOBIOGRAPHICAL STATEMENT

Anwesha Sarkar

Education:

- 2011-2015, Wayne State University, Dept. of Physics and Astronomy, PhD.
- 2010-2011, Institute of Physics, Bhubaneswar, India, M.Phil.
- 2008-2010, Indian Institute of Technology, Madras, India, M.Sc.
- 2005-2008, St. Xavier's College, Kolkata, India, B.Sc.

Employment:

- Fall 2015, Wayne State University, Grad. Research Assistant
- 2011-2015, Wayne State University, Grad. Teaching Assistant
- 2010-2011, Institute of Physics, Bhubaneswar, India, Research Assistant.

Recent Journal Publications:

- A. Sarkar, A. Sohail, J. Dong, R. Fridman and P. Hoffmann, Measurement of DDR1-Collagen interaction Forces with Atomic force Microscopy (manuscript prepared, presented APS March Meeting,2015)
- A. Sarkar, E. Mayyas and P. Hoffmann, Effect of Surface Density of Active sites on Rupture Force Distributions of Single Molecule Interactions (manuscript prepared, presented in APS, BPS and MMMS meetings).
- S. Jones, A. Sarkar, O. M. Merkel and P. Hoffmann, An Insight into the Biophysical Characteristics of siRNA targeted micelleplexes with Atomic Force Microscopy (manuscript prepared).